

AD-A284 583



①

PL-TR-93-2238

**Innovative Development and Application
of Models for Weakly Ionized
Ionospheric Plasmas.**

**J. Vincent Eccles
Russell Armstrong
James Hingst**

**Mission Research Corporation
One Tara Blvd., Suite 302
Nashua, New Hampshire 03062-2801**

November 1993

**DTIC
ELECTE
AUG 22 1994
S G D**

**Final Report
15 May 1990-30 November 1993**

APPROVED FOR PUBLIC RELEASE; DISTRIBUTION UNLIMITED

DTIC QUALITY INSPECTED 8



**PHILLIPS LABORATORY
Directorate of Geophysics
AIR FORCE MATERIEL COMMAND
HANSCOM AIR FORCE BASE, MA 01731-3010**

7588

94-26557

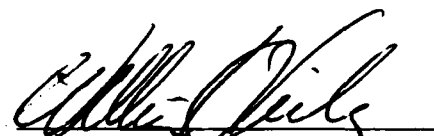


94 8 19 0 87

"This technical report has been reviewed and is approved for publication"


DONALD E. HUNTON
Contract Manager


JOHN F. PAULSON
Branch Chief


WILLIAM K. VICKERY
Division Director

This report has been reviewed by the ESD Public Affairs Office (PA) and is releasable to the National Technical Information Service (NTIS).

Qualified requestors may obtain additional copies from the Defense Technical Information Center. All others should apply to the National Technical Information Service.

If your address has changed, or if you wish to be removed from the mailing list, or the addressee is no longer employed by your organization, please notify PL/TSI, Hanscom AFB, MA 01731-3010. This will assist us in maintaining a current mailing list.

Do not return copies of this report unless contractual obligations or notices on a specific document require that it be returned.

REPORT DOCUMENTATION PAGE			Form Approved OMB No. 0704-0188	
Public reporting burden for this collection of information is estimated to average 1 hour per response, including the time for reviewing instructions, searching existing data sources, gathering and maintaining the data needed, and completing and reviewing the collection of information. Send comments regarding this burden estimate or any other aspect of this collection of information, including suggestions for reducing this burden to Washington Headquarters Services, Directorate for Information Operations and Reports, 1215 Jefferson Davis Highway, Suite 1204, Arlington, VA 22202-4302, and to the Office of Management and Budget Paperwork Reduction Project (0704-0188), Washington, DC 20503.				
1. AGENCY USE ONLY (Leave blank)		2. REPORT DATE Nov 93	3. REPORT TYPE AND DATES COVERED Final (15 May 1990-30 Nov 1993)	
4. TITLE AND SUBTITLE Innovative Development and Application of Models for Weakly Ionized Ionospheric Plasmas			5. FUNDING NUMBERS PE: 61102F PR 2310 TA G3 WU BM Contract F19628-90-C-0118	
6. AUTHOR(S) J. Vincent Eccles, James Hingst, Russell Armstrong				
7. PERFORMING ORGANIZATION NAME(S) AND ADDRESS(ES) Mission Research Corporation One Tara Boulevard, Suite 302 Nashua, NH 03062			8. PERFORMING ORGANIZATION REPORT NUMBER	
9. SPONSORING/MONITORING AGENCY NAME(S) AND ADDRESS(ES) Phillips Laboratory 29 Randolph Road Hanscom AFB, MA 01731-3010 Contract Manager: Donald Hunton/GPID			10. SPONSORING/MONITORING AGENCY REPORT NUMBER PL-TR-93-2238	
11. SUPPLEMENTARY NOTES				
12a. DISTRIBUTION/AVAILABILITY STATEMENT Approved for public release; distribution unlimited			12b. DISTRIBUTION CODE	
13. ABSTRACT (Maximum 200 words)—(Continue on reverse if necessary and identify by block number) Artificial modifications of the ionosphere through chemical releases and ionospheric heating experiments are examined with models of chemistry and transport to advance understanding of ion chemistry of the upper atmosphere. The specific releases investigated were the SF ₆ releases of the CRRES-at-Kwajalein rocket campaign and the CO ₂ releases of the Red Air I program. Both the SF ₆ and CO ₂ releases experienced freezing or clustering of the molecules. This must be accounted for in the composition and airglow observations. In addition, HF heating effects in the E and F region were examined through modeling of energy deposition and resulting chemistry. NO _x production in a HF ionospheric heater beam is estimated and compared with natural sources of NO _x . Global effects of HF operation are very small but the local effects can be large enough to permit observable modulations to this environment.				
14. SUBJECT TERMS Active Experiments Ionosphere Chemical Releases HF Radar			15. NUMBER OF PAGES 76	
			16. PRICE CODE	
17. SECURITY CLASSIFICATION OF REPORT Unclassified	18. SECURITY CLASSIFICATION OF THIS PAGE Unclassified	19. SECURITY CLASSIFICATION OF ABSTRACT Unclassified	20. LIMITATION OF ABSTRACT SAR	

FIGURES

	Page
1. Chemistry for a dense cool SF ₆ release in the F ₂ region.....	7
2. Chemistry after a SF ₆ release has expanded and heated.	7
3. (a) Electron density profile for 15 August 1990 measured between 8:23:24-8:28:40 UT, about 9 minutes before launch of the release rocket. (b) Plasma drift velocity averages determined from Altair data taken during summer 1990.....	10
4. The IMS ion data and the Altair radar electron profiles suggest that the ionosphere dropped during the CRRES-2 release experiment at an average velocity of -15 m/s. The O ⁺ ion data saturated but the F region ledge in the later electron profile and the O ⁺ data are approximately 20 km below the earlier ledge.	11
5. Simulations of the ambient chemistry of the CRRES-2 release experiment. The simulations all began with same initial conditions. The initial electron profile is identical to the Altair measurement in Figure (3). (a) The seasonal average vertical velocity is used. The F region ledge and the NO ⁺ "knee" are too high. (b) With no vertical motion the F region ledge is still too high, but the NO ⁺ "knee" appears at the correct altitude. (c) With a constant vertical velocity of -15 m/s the simulation and experiment data have the best match.	12
6. (a) The expansion of the SF ₆ cloud limbs. (b) The collisional heating of the SF ₆ release cloud. (c) The peak density of the release cloud.....	16
7. The position of release rocket, instrument rocket, ion cloud and neutral cloud as predicted by the COM model. The circle is the release point. The triangles are the measured positions of the 7774Å emission in Table 5.....	17
8. A directed release is modeled with COM program. The ion cloud position is still not able to match the 7774Å emission positions from Table 5.	18
9. East-West and North-South cross sections of the 7774Å airglow from the SF ₆ release cloud. The 7774Å intensity is only 4 Rayleighs above the background for this model run. The main characteristic of the run is the assumed initial high temperature of the SF ₆ gas. The SF ₆ temperature is set at the ambient atmospheric temperature (~1000K).	19
10. East-West and North-South cross sections of the 7774Å airglow from the SF ₆ release cloud. The 7774Å intensity is 800 Rayleighs above the background in this model run. The main characteristic of this model is the assumed initial low temperature of the SF ₆ gas. The SF ₆ temperature is set at the release temperature (~300K) and allowed to collisionally heat in the model.	19

FIGURES (CONTINUED)

	Page
11. Peak 7774Å airglow obtained from model and All sky camera. Model release of a) 1.4×10^{26} SF ₆ molecules (no freezing), (b) 1.4×10^{25} SF ₆ molecules (90% freezing), and (c) 1.4×10^{24} SF ₆ molecules (99% freezing).....	21
12. (a,b) IMS data, (c,d) release is 100% vapor, (e,f) release of 10% vapor, (g,h) release of 1% vapor. All profiles are from the downleg of observation rocket.....	22
13. (a) IMS data, (b) release is 100% vapor, (c) release of 10% vapor, (d) release of 1% vapor. All profiles are from the downleg of observation rocket.....	23
14. Integrated conductivities of the evening ionosphere.....	25
15. The shear of the horizontal plasma motion derived from the ionospheric conductivities shown in Figure 14. The corresponding vertical electric-field strength is shown on the top axis.....	25
16. (a) The field-line integrated Pederson conductivity. (b) The field-line integrated ion mass. (c) The horizontal plasma velocity. (d) The vertical plasma velocity. The time is 60 s after the SF ₆ release.....	27
17. Airglow measurements from a 4° by 4° viewing region centered on the upper release (triangles), centered on the lower release (squares), and on the undisturbed background (circles). The background measurements are smoothed.....	32
18. The production profiles of O(¹ D) for both LC chemistry set and SA chemistry set.....	35
19. The loss rates of O(¹ D) by various mechanisms using (a) LC chemistry set, and (b) SA chemistry set.....	36
20. The normalized integrated O(¹ D) airglow as measured by a zenith looking rocket instrument for (a) LC chemistry set, and (b) SA chemistry set.....	37
21. The modeled and measured 6300Å airglow from the center of the upper release. The modeled airglow is obtained from the SA chemistry set (circles) and the LC chemistry set (squares). The LC set airglow curve is divided by four to show the approximate match with the data (diamonds). The Red Air I data from the upper release is plotted with triangles.....	38
22. The modeled and measured 6300Å airglow from the center of the lower release. The modeled airglow is obtained from the SA chemistry set (circles) and the LC chemistry set (squares). The LC set airglow curve is divided by four to show the approximate match with the data (diamonds). The Red Air I data from the lower release is plotted with triangles.....	38

FIGURES (CONTINUED)

	Page
23. The measured airglow intensities for both upper (empty triangles) and lower releases (solid triangle) are compared to the predictions of the SA chemistry (dashed line) and the LC chemistry (solid line). The airglow predictions have been divided by a constant so that the upper release measured and modeled airglow intensities are the same.	39
24. (a) CO ₂ density time history for high altitude release, standard chemistry set. (b) O(¹ D) density time history for high altitude release, standard chemistry set.	41
25. (a) Time history of CO ₂ vibrational level density for high altitude release, explicit CO ₂ vibrational state chemistry set. (b) O(¹ D) density time history for high altitude release, explicit CO ₂ vibrational state chemistry set.	43
26. Estimated reaction rates for breakup of clusters due to collisional heating.	45
27. (a) CO ₂ cluster density time history for high altitude release, single particle removal model: (CO ₂) _n + M → (CO ₂) _{n-1} + CO ₂ + M. 50% of total CO ₂ released as (CO ₂) ₁₀ . (b) O(¹ D) density time history for high altitude release, single particle removal model: (CO ₂) _n + M → (CO ₂) _{n-1} + CO ₂ + M. 50% of total CO ₂ released as (CO ₂) ₁₀	46
28. (a) CO ₂ cluster density time history for high altitude release, small cluster removal model: (CO ₂) _n + M → (CO ₂) _{n-2} + (CO ₂) ₂ + M. 50% of total CO ₂ released as (CO ₂) ₁₀ . (b) O(¹ D) density time history for high altitude release, small cluster removal model: (CO ₂) _n + M → (CO ₂) _{n-2} + (CO ₂) ₂ + M. 50% of total CO ₂ released as (CO ₂) ₁₀	48
29. (a) CO ₂ density time history for high altitude release, sublimation model. (b) O(¹ D) density time history for high altitude release, sublimation model.	49
30. Electron density profiles in and out of the auroral oval. The conditions are for nighttime winter with moderate auroral activity.	57
31. Results of deposition model are for beam frequencies of 2.8 and 8 MHz. Local energy deposition for (a) inside the auroral region and (b) outside the auroral region. Energy flux of HF beams for (c) inside the auroral region and (d) outside the auroral region. Electron temperatures for (e) inside auroral region and (f) outside auroral region. Ionization profiles for (g) inside the aurora zone and (h) outside the aurora zone.	58
32. (a) Energy deposition rates and (b) electron temperature seen by a parcel of air moving through the HF heater beam at 30 m/s. These values are used to drive a detailed chemistry model, first, within an HF heater beam and, second, during a high-energy particle precipitation event.	59

FIGURES (CONTINUED)

	Page
33. The chemical changes are shown for two different cases. The energy deposition is the same in both cases but one case represents HF heating effects (solid lines) and the other represents high-energy particle precipitation effects (dotted lines). (a) The main plasma constituents and (b) the odd nitrogen molecules within the air parcel are shown for the two cases.	60

TABLES

	Page
1. SF ₆ Chemistry.....	2
2. CRRES-at-Kwajalein release conditions.....	10
3. Release rocket trajectory.....	13
4. Instrument rocket information.....	14
5. Airglow center (Michael Mendillo, personal communication).....	16
6. Release Conditions.....	31
7. Nighttime airglow chemistry.....	33
8. Radiative quenching.....	34
9. Stratospheric NO sources [<i>Jackman et al.</i> , 1980].....	53
10. Mesospheric and thermospheric NO sources [<i>Jackman et al.</i> , 1980].....	53
11. Typical HF radar specifications.....	54
12. Electronically excited species contained in the deposition model.....	56

ACKNOWLEDGMENTS

We thank Professor Michael Mendillo, Jeff Baumgardner, and Peter Sultan at the Center for Space Physics of Boston University for their availability and openness on the CRRES-at-Kwajalein and Red Air experiments. In addition, the collaborative discussions with Donald Hunton, John Paulson, A. A. Viggiano and co-workers at Phillips Laboratory were both helpful and necessary for the work presented herein. We also gratefully acknowledge the support of this work by the Phillips Laboratory Geophysics Directorate.

1. SF₆ RELEASES IN THE F REGION

Sulfurhexafluoride (SF₆) is used primarily as a gaseous insulator in high-voltage systems. The insulation ability comes from the fast removal of free electrons through electron attachment. SF₆ has been used as a release chemical in the earth's ionosphere to examine plasma instability processes. The chemistry of SF₆ in the ionosphere requires very few reactions for short time-scales due to the limited number of constituents at ionospheric altitudes. For longer time-scales the reaction list becomes complex. The region near the release becomes an electron hole and a negative-positive ion plasma. Earlier studies used simplified chemistry to model the electron hole that forms in short time [Rosenberg, 1964; Mendillo and Forbes, 1982; Bernhardt, 1984]. Mendillo and Forbes [1982] assumed the major ion would be SF₆⁻, while Bernhardt [1984] predicted SF₅⁻ would dominate due to the high ambient temperature [Fehsenfeld, 1970]. Experimental results from an SF₆ release in the E region suggested that F⁻ may be the dominant negative ion shortly after the release [Hunton et al., 1987].

The most recent ionospheric releases of SF₆ were done as part of the CRRES (Combined Release and Radiation Effects Satellite) program. The NASA/Boston University rocket campaign was entitled CRRES-at-Kwajalein. Two rockets on separate evenings released SF₆ into the ionosphere to reduce conductivity through electron attachment and to mass-load a magnetic flux tube with heavy negative ions. The modified plasma produced a perturbation to the electrodynamics of the evening equatorial ionosphere where dramatic plasma irregularities develop naturally often nightly. The natural development of the irregularities in the equatorial F region has been termed Equatorial Spread F (ESF). Similar and separate releases of barium and H₂O in the evening equatorial ionosphere were used in the Coloured Bubbles Experiment and the Brazilian Ionospheric Modification Experiment (BIME), respectively, to alter electrodynamics of the ionosphere [Haerendel et al., 1983]. Such studies of artificially-initiated ESF are expected to illuminate the natural causes of ESF.

The purpose of this paper is to examine the current understanding of the SF₆ chemistry by comparing experimental data and modeling of two SF₆ releases from rockets launched from Kwajalein island during the CRRES-at-Kwajalein campaign. The two release rockets are named CRRES-1 and CRRES-2 within this document. The initial several minutes of the release are observed by airglow produced by the chemistry occurring within the release cloud. The late time chemistry (15 minutes after the release) is observed by an Ion Mass Spectrometer (IMS) on a second instrument rocket. The combination of the two observations provides bracketing information that will help discriminate between reaction sets and physical processes included in the model.

The results of the study suggest that the collective chemistry presented by several authors [Mendillo and Forbes, 1982; Bernhardt, 1984, 1987; Hunton et al., 1987] correctly describes the short term chemical processes within the release. As time progresses, oxidation of the SF_n molecules increases the necessary reaction list. There are few laboratory studies on attachment characteristics of SO_mF_n species but the electron density is not greatly affected by the presence of the large species list. For studies of plasma effects within the deep electron hole near the release point, SF₆⁻, SF₅⁻, and F⁻ appears to be a sufficient list of negative ions. To examine late time chemistry and the broader spatial extent of the release one must include SOF₃⁻ and maybe SF₄⁻ and SOF₅⁻.

This paper presents the chemistry and airglow occurring within an SF₆ ionospheric release. In Section 2 the ambient background is modeled to provide correct context for modeling the release. Section 3 presents early time and late time observations and model results of the second SF₆ release

in the CRRES-at-Kwajalein campaign. Section 4 provides a summary and advances suggestions for future work.

2. SF₆ CHEMISTRY

Mendillo and Forbes [1982] and *Bernhardt* [1984; 1987] review ion chemistry of ionospheric SF₆ releases. Several important reactions are added by *Hunton et al.* [1987]. It is apparent from previous and present SF₆-ionospheric chemistry studies that there is still an element of unknown in the set of chemical reactions. The reactions used in this study are presented in Table 1.

TABLE 1. SF₆ Chemistry.

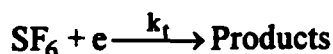
	DISSOCIATIVE ATTACHMENT	
$SF_6 + e \xrightarrow{k_1} SF_5^- + F$	$k_2 = k_1 / [1 + 1.56 \times 10^{-3} \exp(4770/T_n)]$	see <i>Bernhardt</i> [1984]
$SF_6 + e \xrightarrow{k_3} F^- + SF_5$	$k_3 \approx 0$	<i>Mullen et al.</i> [1971]
$SOF_4 + e \xrightarrow{k_4} SOF_3^- + F$	$k_4 \approx 10^{-8}$	Sauers, communication
	RADIATIVE ATTACHMENT	
$SF_6 + e \xrightarrow{k_a} SF_6^-$	$k_a = (k_1 - k_2) / 10$	see <i>Bernhardt</i> [1984]
$O + e \xrightarrow{k_5} O^-$	$k_5 = 1.3 \times 10^{-15}$	<i>Branscomb</i> [1964]
	CHARGE EXCHANGE	
$O^+ + SF_6 \xrightarrow{k_6} SF_5^+ + F + O$	$k_6 = 1.5 \times 10^{-9}$	<i>Fehsenfeld</i> [1971]
$O^+ + SF_5 \xrightarrow{k_7} SF_5^+ + O$	$k_7 = 10^{-9}$	estimated ($\sim k_6$)
$O_2^+ + SF_5 \xrightarrow{k_8} SF_5^+ + O_2$	$k_8 = 10^{-9}$	estimated ($\sim k_6$)
$SF_6^- + O \xrightarrow{k_9} O^- + SF_6$	$k_9 = 5 \times 10^{-11}$	<i>Fehsenfeld</i> [1971]
$SF_5^- + SF_6 \xrightarrow{k_{10}} SF_6^- + SF_5$	$k_{10} = 2.9 \times 10^{-14}$	<i>Seppelt</i> [1977]
$F^- + SF_6 \xrightarrow{k_{11}} SF_6^- + F$	$k_{11} = 1.2 \times 10^{-12}$	<i>Greenberg and Hargis</i> [1989]
	CHARGE INTERCHANGE	
$SF_5^- + O \xrightarrow{k_{12}} F^- + SOF_4$	$k_{12} = 1.1 \times 10^{-11}$	<i>Hunton et al.</i> [1987]
$SF_6^- + SOF_4 \xrightarrow{k_{13}} SOF_5^- + SF_5$	$k_{13} = 8.5 \times 10^{-9}$	<i>Van Brunt et al.</i> [1988]
$SF_6^- + SF_4 \xrightarrow{k_{14}} SF_5^- + SF_5$	$k_{14} = 3.7 \times 10^{-10}$	<i>Babcock and Streit</i> [1981]
	ION-ION RECOMBINATION	
$O^+ + O^- \xrightarrow{k_{15}} O^* + O$	$k_{15} = 2.7 \times 10^{-7} (T/300)^{-0.5}$	<i>Olson et al.</i> [1971]
$O^+ + SF_6^- \xrightarrow{k_{16}} O^* + SF_6$	$k_{16} = 6 \times 10^{-8} (T/300)^{-0.5}$	<i>Bortner et al.</i> [1972]
$SF_5^+ + SF_6^- \xrightarrow{k_{17}} SF_5 + SF_6$	$k_{17} = 3.9 \times 10^{-8} (T/300)^{-0.5}$	<i>Church and Smith</i> [1977]
$X^+ + Y^- \xrightarrow{k_{18}} X + Y$	$k_{18} = 6 \times 10^{-8} (T/300)^{-0.5}$	<i>Bortner et al.</i> [1972]
	E-ION RECOMBINATION	
$SF_5^+ + e \xrightarrow{k_{19}} SF_4 + F$	$k_{19} = 2 \times 10^{-7} (T/300)^{-0.5}$	<i>Biondi</i> [1973]
	ASSOCIATIONAL DETACHMENT	
$O^- + O \xrightarrow{k_{20}} O_2 + e$	$k_{20} = 2 \times 10^{-10}$	<i>Fehsenfeld et al.</i> [1969]

TABLE 1. SF₆ Chemistry. (continued)

COLLISIONAL DETACHMENT		
SF ₆ ⁻ + M $\xrightarrow{k_{21}}$ SF ₆ + e + M	k ₂₁ =1×10 ⁻¹²	Wang et al. [1989]
SF ₅ ⁻ + M $\xrightarrow{k_{22}}$ SF ₅ + e + M	k ₂₂ =1×10 ⁻¹³	Wang et al. [1989]
F ⁻ + M $\xrightarrow{k_{23}}$ F + e + M	k ₂₃ =5×10 ⁻¹⁸	Wang et al. [1989]
COLLISIONAL DISSOCIATION		
SF ₆ ⁻ + M $\xrightarrow{k_{24}}$ SF ₅ ⁻ + F + M	k ₂₄ =1×10 ⁻¹³	Wang et al. [1989]
SF ₆ ⁻ + M $\xrightarrow{k_{25}}$ F ⁻ + SF ₅ + M	k ₂₅ =1×10 ⁻¹³	Wang et al. [1989]
SF ₅ ⁻ + M $\xrightarrow{k_{26}}$ F ⁻ + SF ₄ + M	k ₂₆ =2×10 ⁻¹⁴	Wang et al. [1989]
PHOTODETACHMENT		
SF ₄ ⁻ $\xrightarrow{k_{27}}$ SF ₄ + e	k ₂₇ =1.0	Bernhardt [1987]
SF ₅ ⁻ $\xrightarrow{k_{28}}$ SF ₅ + e	k ₂₈ =0.5	Bernhardt [1987]
SF ₆ ⁻ $\xrightarrow{k_{29}}$ SF ₆ + e	k ₂₉ =2.0	Bernhardt [1987]
O ⁻ $\xrightarrow{k_{30}}$ O + e	k ₃₀ =1.15	Burch et al. [1959]
NEUTRAL REARRANGEMENT		
O + SF ₅ $\xrightarrow{k_{31}}$ SOF ₄ + F	k ₃₁ =2×10 ⁻¹¹	Van Brunt [1990]
SF ₅ + SF ₅ $\xrightarrow{k_{32}}$ SF ₄ + SF ₆	k ₃₂ =5×10 ⁻¹³	Van Brunt [1990]

2.1 Electron Attachment

Initially, the dominant reaction is SF₆-e attachment, which proceeds at a rate k₁ = 2.2×10⁻⁷ cm³s⁻¹ for low energy electrons (T_e~0.1 eV) [Fehsenfeld, 1970; Mothes et al., 1972; Spence and Schultz, 1973; Phelps and Van Brunt, 1988]



The cross section dramatically drops off with increasing electron energies [Mullen et al., 1971; Kline et al., 1979; Phelps and Van Brunt, 1988]; only the lowest energy electrons have a significant attachment cross section with SF₆. In a release in the nighttime ionosphere, SF₆ vibrational modes can significantly cool electrons to provide low energy electrons for rapid attachment and k_t can be considered constant. The products of the electron attachment reaction depend upon the vibrational state of the parent SF₆ molecule prior to attachment. The branching of SF₆ attachment chemistry can be modeled with a ground state SF₆⁻ and a vibrationally excited SF₆^{-*}. SF₆^{-*} represents all SF₆⁻ molecules with vibrational energy below the F-SF₅⁻ dissociation energy. Bernhardt [1984] uses three vibrationally excited species, SF₆^{-*}, SF₆^{-**} and SF₆^{-***}, but the two additional excited species dissociate almost instantaneously into end products.

The three main branches of the attachment process are



where $k_1 + k_2 + k_3 = k_i$. The branching of the attachment process is temperature dependent. Reaction (2.3) is negligible at ionospheric temperatures. The temperature dependent rates of reactions (2.1-2) are approximated with

$$k_2 = k_i / \left[1 + 156 \times 10^{-3} \exp(4770/T_n) \right] \quad (2.4)$$

$$k_1 = k_i - k_2 = k_i / \left[1 + 640 \exp(-4770/T_n) \right] \quad (2.5)$$

[Bernhardt, 1984; Fehsenfeld, 1970]. The metastable molecule SF_6^* can auto-detach, radiatively stabilize, or collisionally stabilize, as illustrated in the following reactions.



Auto-detachment of SF_6^* is rapid: $\tau_a = 1/\alpha_a = 10\mu s$ to $93\mu s$ depending on SF_6 vibrational energy [Odom *et al.*, 1975; Foster and Beauchamp, 1975; Lifshitz, 1983]. Collisional stabilization has a rate of $k_s = 5.4 \times 10^{-10} \text{ cm}^3 \text{ s}^{-1}$. Above 125 km altitude collisional stabilization can be neglected. Radiative stabilization is approximately ten times slower than auto-detachment [Foster and Beauchamp, 1975]. Thus, the net production of SF_6^- through the combined reactions of (2.1, 2.6-2.8) becomes



where

$$k_a = \frac{(\alpha_r + k_s[M])}{(\alpha_a + \alpha_r + k_s[M])} k_1 \approx \frac{\alpha_r}{\alpha_a} k_1 \approx \frac{k_1}{10} \quad (2.10)$$

The electron attachment reactions dominate the very early time chemistry that defines the negative-positive ion plasma within the cloud.

In the CRRES-at-Kwajalein SF_6 release, the IMS possibly observed SF_4^- at about the same density levels as SF_6^- and SF_5^- . Previous studies of SF_6 releases did not allow for SF_4^- production which can arise primarily through electron attachment to SF_4 . SF_4 attachment chemistry is similar to SF_6 chemistry with attachment branches



The attachment rate for SF_4 11 times slower than SF_6 attachment (Miller *et al.*, 1994). As with SF_6 radiative stabilization must occur. Auto-detachment rate is approximately 100 times faster than radiative stabilization which make SF_4^- production very slow in a rarified atmosphere (Sauer *et al.*, 1993).

The apparent IMS observation of SF_4^- (108 amu) densities may instead be SOF_3^- (105 amu) due to the relatively low mass resolution of the instrument. Though SF_6^- and SF_5^- will be important during the first several minutes of the release, other neutral molecules appear through the oxidation of SF_n and more exotic negative ions emerge. In particular, modeling suggests that

SOF_3^- is more dense than SF_6^- and SF_5^- 10 minutes after the release. The main reaction producing SOF_3^- is



2.2 Charge Transfer and Charge Interchange

The instrumented rocket was launched approximately 15 minutes after the release rocket launch. 15 minutes after the SF_6 release reactions slower than the attachment processes have altered the ion constituents significantly. In particular, charge exchange will have altered the positive component within the release cloud through



These are potentially important reactions for a daytime release where photo-detachment reduces the negative ion densities. The introduction of positive molecular ions will alter the electrodynamics through mass loading of the field lines as well as plasma reductions through dissociative recombination.

Two major adjustments to the negative ion populations result from the dominance of O in the upper atmosphere.



Reaction (2.3) is particularly important for the late time observations of the negative ion plasma. The dominant negative ion at late times is F^- with reaction (2.3) as the primary source of F^- .

Other negative ion species appear through fast interchange reactions as oxidation of SF_n continues:



[*Van Brunt et al.*, 1988]. This leads to a potentially complex negative-positive ion plasma.

2.3 Recombination

As the plasma is altered from an atomic oxygen ion-electron plasma to a molecular ion plasma, the recombination rates are accelerated. The O^+e recombination is so slow as to be negligible ($\approx 10^{-18} \text{ cm}^{-3} \text{ s}^{-1}$). As positive molecular ions appear the plasma recombination rate increases to about $10^{-7} \text{ cm}^{-3} \text{ s}^{-1}$ [*Biondi*, 1973]. Ion-ion recombination is not much slower at about $10^{-8} \text{ cm}^{-3} \text{ s}^{-1}$ [*Bortner et al.*, 1972].

2.4 CID and Other Reactions

As time progresses additional loss reactions can enter into the chemistry. *Hunton et al.* [1987] suggest collisionally induced detachment and dissociation as loss mechanisms for negative ions. Recent investigations [*Wang et al.*, 1989; *Olthoff et al.*, 1989] provide the cross sectional information to allow estimates for rates at atmospheric temperatures ($T \sim 1000\text{K}$). However, these reactions are slow ($< 10^{-12} \text{ cm}^3 \text{ s}^{-1}$), therefore, they probably have limited influence on the chemical perturbation except during late times after the release.

Associational attachment generally are much faster. For example,



at $2 \times 10^{-10} \text{ cm}^{-3} \text{ s}^{-1}$ [Fehsenfeld *et al.*, 1966; 1969] and



at $1.6 \times 10^{-9} \text{ cm}^{-3} \text{ s}^{-1}$ [Fehsenfeld *et al.*, 1975] may be operating with other negative ions though no rates could be found in the literature. Is it possible that the following are important?



Because the rates are possibly near gas kinetic, they could influence negative ion densities.

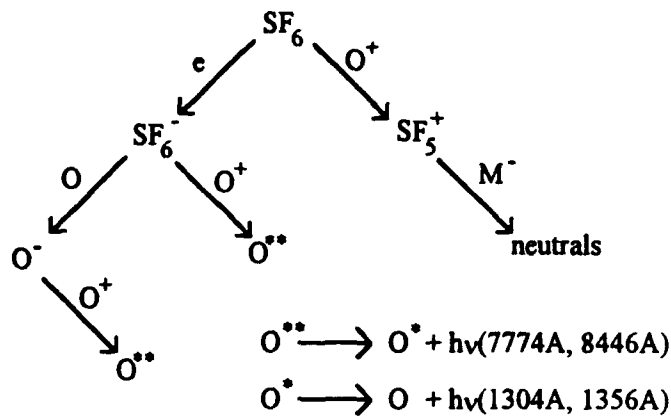
2.5 Neutral Rearrangement

Potentially important neutral reactions are missing in the review papers of ionospheric release of SF_6 . The neutral reactions may influence the late-time development of an ionospheric perturbation. Due to the dominance of O at F region altitudes, the oxidation of SF_n molecules leads to several $\text{SO}_m\text{F}_{n-1}$ neutrals [Van Brunt, 1985; Van Brunt and J.T. Herron, 1990]. In addition, the ion-ion recombination, as well as the charge interchange chemistry given above, produces many contaminant neutral species within the chemically perturbed region. Some contaminant species are electron attachers (SF_4 , SF_5 , SO_2F , SO_2F_2 , SOF_4).

2.6 Two Regions of Chemistry

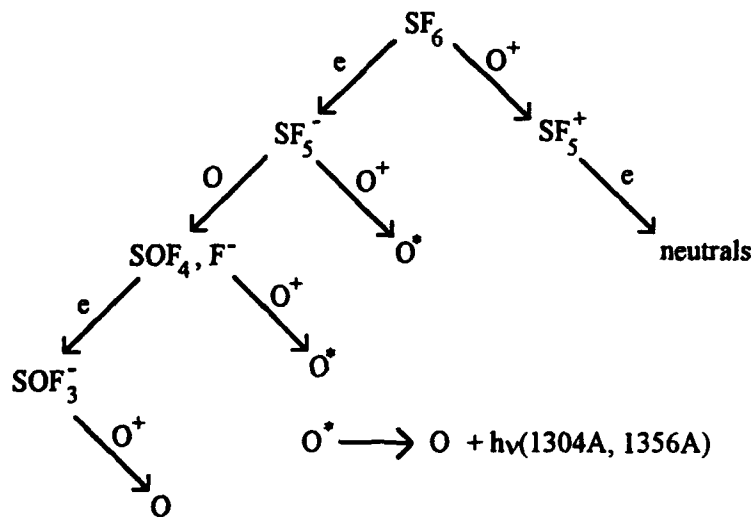
Early after the release, the SF_6 is cool ($T \sim 300\text{K}$) and dense ($n_{\text{SF}_6} > n_e$). Before the SF_6 release cloud expands to a 20 km radius, the rapid attachment chemistry has occurred and a deep electron hole has been created. The resulting ion-ion plasma cloud may increase the mass or decrease the conductivity on the magnetic flux tube to initiate instability processes at the edge of the plasma cloud. Additionally, the recombination of SF_6^- and O^+ has enough energy to create highly excited O and lead to visible airglow emissions. The important chemical processes are illustrated in Figure 1.

In the broader region after the release cloud has expanded and collisionally heated, the chemistry leads to a diffuse negative ion perturbation that does not affect the electrodynamics. The recombination of SF_5^- or F^- with O^+ does not lead to visible airglow emissions but does produce UV emission. The important chemical processes are illustrated in Figure 2.



- If SF_6 is cool and dense, then:
- I. SF_6^- , O^- , SF_5^+ , O^+
 - II. Deep electron hole.
 - III. Visible and UV airglow.

Figure 1. Chemistry for a dense cool SF_6 release in the F_2 region.



- If SF_6 is hot and less dense, then:
- I. SF_5^- , F^- , SF_5^+ , O^+
 - II. Broader region disturbance.
 - III. UV airglow.

Figure 2. Chemistry after a SF_6 release has expanded and heated.

2.7. SF₆-H₂O Competition

The release rocket and observation rocket outgas atmospheric gases that are imbedded in the skin of the rockets. The primary constituent of the outgassing is H₂O. The H₂O competes with SF₆ in the positive-ion chemistry. H₂O and O⁺ charge exchange and subsequent hydration chemistry occur:



The increase of molecular ions leads to increased recombination of the plasma.



Within the SF₆ induced perturbation the electron density is reduced and ion-ion mutual neutralization will be the avenue for H₂O⁺ and H₃O⁺ loss.



A further complication of the SF₆ release chemistry is the possibility of water clustering of the negative ions.



However, a third-body is required for hydration to proceed. Hydration will only be important for releases below 100 km and in the first moments after a release.

The introduction of H₂O will affect SF₆ chemistry through competition for O⁺ ions and through indirect reaction of H₂O chemistry products (OH, H) with SF_n fragments. Effects of H₂O in an F region release of SF₆ is small. The only observable change is the increased presence of H₂O⁺ as a minor ion species.

2.8. Airglow Emissions from an SF₆ Release

Airglow observations were made during the CRRES-at-Kwajalein campaign. An all sky camera of the Center for Space Physics of Boston University was used to observe the spatial distribution of the expected airglow enhancement during the SF₆ release. The enhancement is primarily from the ion-ion recombination



Recombination of O^+ with SF_4^- and SF_6^- can produce highly excited states of atomic oxygen. These excited states decay in multiple steps. The specific excited states of interest and their associated emission lines are:



The lower states relax to ground state via



The branching ratios for the excited states of O produced in the recombination have been approximated by using the O^+ -e recombination branching ratios [Bernhardt *et al.*, 1986].

Recombination of O with SF_5^- and F^- can only produce the lower excited states of atomic oxygen that radiate ultraviolet airglow. Recombination with SOF_3^- can only produce the low metastable states of $O(^1S)$ and $O(^1D)$. The differing energetics of the recombination reactions allows for interesting spatial structure of the airglow in the different wavelengths. In the small region where SF_6^- densities are high, 7774Å is bright, but in the broader region where SF_5^- and F^- dominate, 1356Å is important. It would be instructive to measure 7774Å and 8446Å or 1304Å and 1356Å lines together.

3. MODELING

The NASA/Boston University CRRES-at-Kwajalein campaign took place during the summer of 1990. Two sounding rockets (CRRES-1 and CRRES-2) released SF_6 on separate evenings in an attempt to induce equatorial spread F phenomena. Multiple diagnostics were used to examine the resulting perturbations to the ionosphere including Boston University's all sky optical camera and incoherent scatter radar (ALTAIR). An ion-mass spectrometer (IMS) from Phillips Laboratory Directorate of Geophysics flew on an instrumented rocket launched fifteen minutes after the second release rocket (CRRES-2). Table 2 compiles the geographic, solar, and atmospheric conditions for the equatorial launches. Both flights released approximately 35 kg of SF_6 (1.4×10^{26} molecules) at a temperature of 320K. The release canister took 3 to 7 s to empty.

The resulting SF_6 -ionospheric chemistry creates four categories of alterations to the ambient conditions:

- i. Electron depletion. This interesting perturbation alters electromagnetic wave scattering and propagation.
- ii. Negative-positive ion plasma. The replacement of electrons by heavy negative ions alters the transport properties along magnetic field-lines, increases cross field conductivity, and increases the gravitationally-induced current.
- iii. Plasma depletion through ion-ion recombination. The plasma reduction takes place on the time scale of minutes and eventually decreases conductivities.
- iv. Neutral composition perturbation. There are several metastable constituents that participate in airglow enhancements.

The study of the SF₆ release cannot be done exclusively with models of the chemical perturbation. Comparison of simulation and experiment would have only limited validity. To obtain more quantitative comparisons, the dynamics and electrodynamics of the CRRES-at-Kwajalein release were modeled in conjunction with the chemistry.

TABLE 2. CRRES-at-Kwajalein release conditions.

	CRRES-1	CRRES-2
Launch date	11 August 1990	14 August 1990
Launch time	08:10:00 UT	08:29:00 UT
Release time	08:17:20 UT	08:34:34 UT
Release Altitude	375.5 km	428 km
10.7 cm Flux	187	200
<10.7 cm Flux>	228	228
Sunspot Number (R_a)	161	229
Geo-Longitude	166.90° E	167.0898° E
Geo-Latitude	10.97° N	10.8825° N
Magnetic Dip	~ 0°	~ 0°
A_p Index	9	26

3.1 Ambient Conditions

The atmospheric conditions used as a background for the modeling studies were determined by MSIS90 [Hedin, 1991]. The pre-flight electron densities and seasonally averaged plasma velocities were obtained from Altair radar measurements (Peter Sultan, personal communication) (Figure 3).

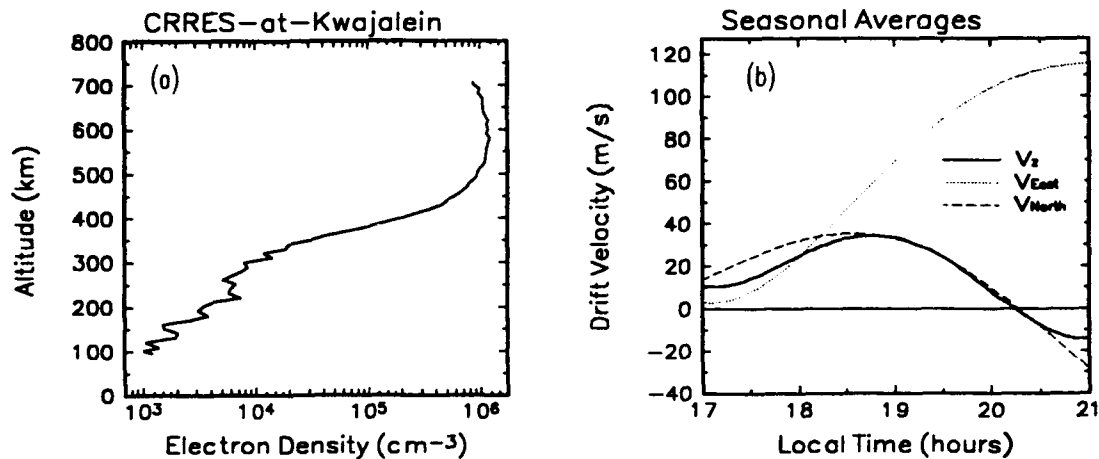


Figure 3. (a) Electron density profile for 15 August 1990 measured between 8:23:24-8:28:40 UT, about 9 minutes before launch of the release rocket. (b) Plasma drift velocity averages determined from Altair data taken during summer 1990.

The IMS measurement indicates negative ions concentrations are small compared to the total positive ion concentration. Thus, the IMS-measured O^+ , NO^+ , O_2^+ profiles should approximately represent the undisturbed conditions. Unfortunately, the O^+ IMS channel was saturated and does not provide information on the "true" profile above 300 km. The IMS data combined with electron profiles obtained from Altair Radar data do give a consistent picture of the ionosphere at the time of the instrument rocket fly-through. The electron profiles for 19.57 LT (8.43 UT) and 19.97 LT (8.83 UT) and the IMS measurements at approximately 19.97 LT (8.83 UT) suggest that the ionosphere dropped at an average rate of 15 m/s (Figure 4). The seasonal average vertical velocity is upward during the experiment time interval. Perhaps the seasonally averaged vertical velocity does not accurately represent the vertical velocity for the night of the release. This is not surprising due to the extreme variability of the vertical velocity near sunset.

We attempted to model the ambient ionosphere from the time of the Altair measurement to the time of the IMS measurement. Comparison of model results to positive ion chemistry measurements will provide additional insight into the correctness of the ionospheric vertical velocity history. Three simulations were performed to reinforce the thesis that the ionosphere was moving downward ~ 15 m/s after the SF_6 release of CRRES-2. The simulations use: the seasonal averaged vertical velocity (Figure 3), zero vertical velocity and, constant downward velocity of -15 m/s. The simulations begin with conditions provided by MSIS90 neutral atmosphere and the electron profile measured by the Altair radar at 19.57 LT. The simulations continue until the time of the observation rocket apogee (19.95 LT or 900 s after the SF_6 release). The first simulation that uses the seasonal average vertical velocity produces a very high F region ledge and a high NO^+ profile "knee" (Figure 5a). Using no vertical motion, the F region ledge and the NO^+ knee are better but still the electron and O^+ profiles are too high (Figure 5b). Using vertical velocity of -15 m/s the simulation and experiment data have a good match in total electron density (Figure 5c). The O_2^+ and NO^+ density profiles are approximately correct in shape but the lower altitude magnitudes do not compare favorably with the data. The total molecular ion density observed is approximately 3 times the modeled density. This could be due to differences in the true conditions from the model conditions (for example, T_e , $[N_2]$, $[O^+]$).

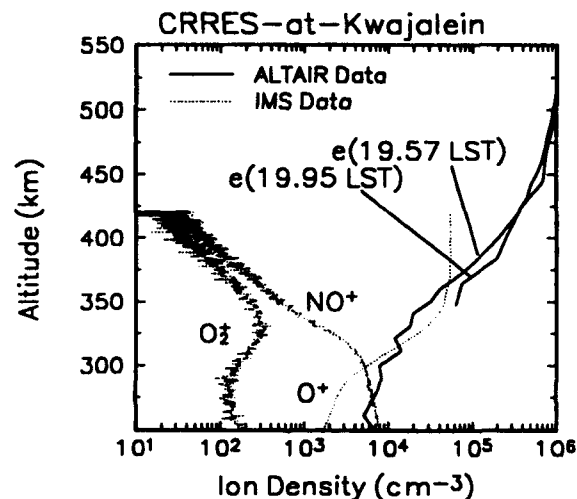


Figure 4. The IMS ion data and the Altair radar electron profiles suggest that the ionosphere dropped during the CRRES-2 release experiment at an average velocity of -15 m/s. The O^+ ion data saturated but the F region ledge in the later electron profile and the O^+ data are approximately 20 km below the earlier ledge.

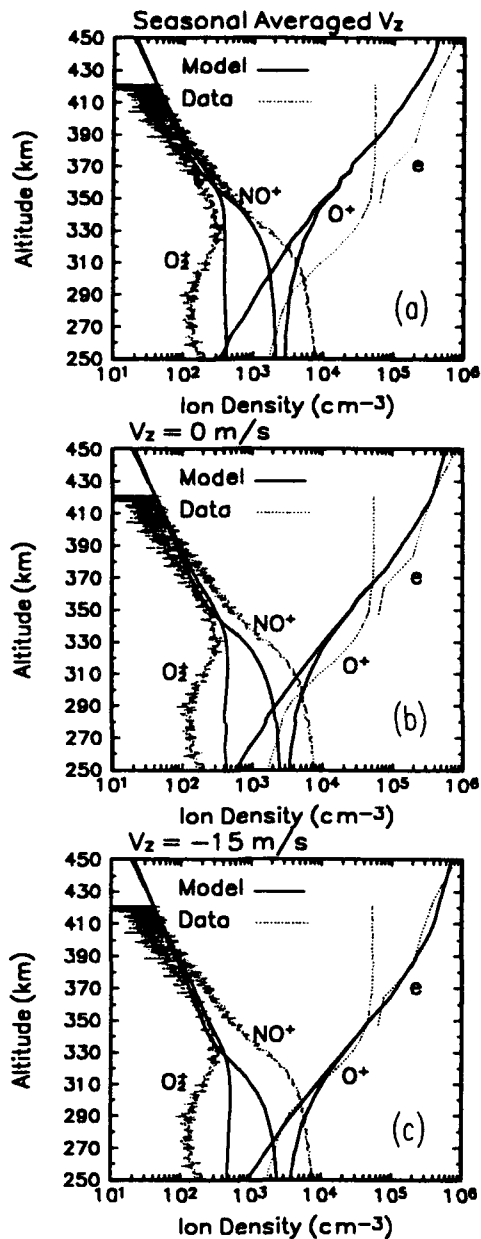


Figure 5. Simulations of the ambient chemistry of the CRRES-2 release experiment. The simulations all began with same initial conditions. The initial electron profile is identical to the Altair measurement in Figure (3). (a) The seasonal average vertical velocity is used. The F region ledge and the NO^+ "knee" are too high. (b) With no vertical motion the F region ledge is still too high, but the NO^+ "knee" appears at the correct altitude. (c) With a constant vertical velocity of -15 m/s the simulation and experiment data have the best match.

With a reasonable estimate of the electron profile and vertical velocity time history one can begin to compare the model results of the SF₆ release with observational data. The constant downward plasma velocity of -15 m/s will be used in the following studies. This velocity reproduced the observed ambient electron profile at the time of the observation rocket fly-through.

3.2 Motion of the CRRES SF₆ Release

To properly compare model results with airglow and IMS density measurements one must determine the path of the neutral and ion clouds created by the release experiment. This requires knowledge of position and velocity of both the release rocket and the instrument rocket. Table 3 lists trajectory information for the release rocket against mission elapsed time (MET). Table 4 lists the instrument rocket information.

TABLE 3. Release rocket trajectory against mission elapsed time (MET).

MET (s)	Latitude	Longitude	Altitude
0.00	9.4012	167.4651	0.037
2.40	9.3998	167.4570	2.017
30.00	9.4652	167.4441	37.019
60.00	9.6148	167.4150	112.676
90.00	9.7611	167.3841	179.848
120.00	9.9044	167.3511	238.722
150.00	10.0459	167.3169	289.423
180.00	10.1853	167.2815	332.104
210.00	10.3228	167.2455	366.883
240.00	10.4596	167.2084	393.786
270.00	10.5953	167.1705	412.914
300.00	10.7301	167.1331	424.334
330.00	10.8669	167.0963	427.334
334.00	10.8825	167.0898	427.942
360.00	11.0038	167.0596	424.191
390.00	11.1406	167.0228	412.582
420.00	11.2777	166.9861	393.237
450.00	11.4143	166.9493	366.310
480.00	11.5511	166.9125	332.639
510.00	11.6880	166.8758	289.040
540.00	11.8248	166.8390	238.399
570.00	11.9617	166.8023	179.616
600.00	12.0985	166.7655	112.502
630.00	12.2353	166.7287	37.284
660.00	12.3722	166.6920	2.767

TABLE 4. Instrument rocket information against mission elapsed time (MET).

MET (s)	Latitude	Longitude	Altitude
0.00	9.4012	167.4651	0.037
5.00	9.4029	167.4663	2.017
30.00	9.4366	167.4974	36.552
60.00	9.5163	167.5706	111.488
90.00	9.5944	167.6396	177.946
120.00	9.6709	167.7050	236.134
150.00	9.7460	167.7675	286.192
180.00	9.8201	167.8275	328.234
210.00	9.8933	167.8855	362.365
240.00	9.9656	167.9419	388.668
270.00	10.0375	167.9972	407.196
300.00	10.1089	168.0516	417.999
327.00	10.1732	168.1002	421.130
360.00	10.2515	168.1601	416.491
390.00	10.3228	168.2150	404.182
420.00	10.3944	168.2709	384.137
450.00	10.4664	168.3280	356.310
480.00	10.5391	168.3870	320.639
510.00	10.6125	168.4483	277.040
540.00	10.6871	168.5124	225.399
570.00	10.7628	168.5798	165.616
600.00	10.8400	168.6512	97.502
630.00	10.9097	168.7286	26.284
660.00	10.9063	168.7390	15.767

A simple and computationally fast release cloud model was developed to predict approximate position, density and size of a neutral release cloud (ignoring chemistry). The 427.95 km altitude is above the region where diffusive expansion through the background gas can be used to accurately describe the early expansion and fall. Therefore, a model which included momentum terms in the fall and expansion was necessary to model accurately. It is assumed that diffusion is important and a Gaussian cloud is used rather than a shell cloud. A center-of-mass (COM) model was developed which follows the motion of the center of the Gaussian release cloud as it falls through an MSIS defined atmosphere. The expansion and heating of the cloud are also computed. The basic assumption is that the cloud maintains a Gaussian shape described by

$$n(x, y, z, t) = n_o(t) \exp \left[- \left(\frac{x - x_o}{r_x} \right)^2 - \left(\frac{y - y_o}{r_y} \right)^2 - \left(\frac{z - z_o}{r_z} \right)^2 \right] \quad (3.1)$$

where x, y, z represent eastward, northward and vertical directions, n is density, and n_o is peak density. The peak density goes as

$$n_o(t) = \frac{N}{r_x r_y \frac{r_{z+} + r_{z-}}{2} \pi^{\frac{3}{2}}} \quad (3.2)$$

The cloud center position (x_o, y_o, z_o) is followed with simple center-of-mass equations of motion

$$\frac{\partial \mathbf{u}_o}{\partial t} = -v_n (\mathbf{u}_o - \mathbf{u}_n) - g \hat{z} \quad (3.3)$$

\mathbf{u}_o is the cloud center velocity, v_n is the collision frequency between the release gas and the background neutrals, and g is gravitational acceleration. The expansion of the cloud is determined for each limb of the cloud. The horizontal limbs (r_x and r_y) are assumed to expand identically. The upper and lower limbs of the cloud, r_{z+} and r_{z-} , are assumed to have independent expansion rates. The velocity of expansion is determined by the velocity of the n_0/e radius of each cloud limb. This radius grows at the rate defined by the velocity of the gas at that radius, which can be determined by the momentum equation

$$\frac{\partial u_{rx}(r_x)}{\partial t} = -v_n [u_{rx}(r_x) - u_{rx}(z_o)] - \frac{kT_o}{r_x m_o} \quad (3.4)$$

$$\frac{\partial u_{rz+}(r_{z+})}{\partial t} = -g - v_n [u_{rz+}(r_{z+}) - u_{rz+}(z_o + r_{z+})] - \frac{kT_o}{r_{z+} m_o} \quad (3.5)$$

$$\frac{\partial u_{rz-}(r_{z-})}{\partial t} = -g - v_n [u_{rz-}(r_{z-}) - u_{rz-}(z_o + r_{z-})] - \frac{kT_o}{r_{z-} m_o} \quad (3.6)$$

where u_{rx} is velocity of the horizontal limb expansion, u_{rz+} is the velocity of the upper limb expansion, u_{rz-} is the velocity of the lower limb expansion, and m_o is the release gas mass, and T_o is the release gas temperature. The pressure term in each equation reduces as the Gaussian limb radii in the denominator increase. The collisional heating of the cloud can also be approximated through

$$\frac{C_v}{C_p} \frac{\partial T_o}{\partial t} = \frac{v_n m_n}{m_o + m_n} \left[3k(T_o - T_n) - \frac{m_n}{2} (\mathbf{u}_o - \mathbf{u}_n)^2 \right] \quad (3.7)$$

Only the center of the cloud is used to define the temperature of the whole release cloud. The solutions assume that the background gases are unchanged by the release. This is true for the large scale problem. Only at early times ($t < 10$ s) will the release affect the background densities and temperatures. The CRRES-2 SF_6 release is modeled using the above COM model with the MSIS90 neutral atmosphere model. The northward and eastward rocket velocities at release were 503 m/s and -136 m/s, respectively.

Figure 6 gives the expansion history and temperature of the modeled release cloud. The temperature increase is slow due to the internal energy capacitance of SF_6 . The slow increase allows SF_6^- to be produced as the dominant ion for a significant period. The cloud moves initially with the rocket trajectory and expands adiabatically for one mean free path (~ 50 km). After two minutes, diffusion controls the motion. Within five minutes, the release cloud has the same horizontal motion and temperature as the background atmosphere. The region of chemical influence of the cloud has a radius greater than 100 km. The differential neutral drag force on the top and bottom limbs of the cloud causes the cloud to flatten.

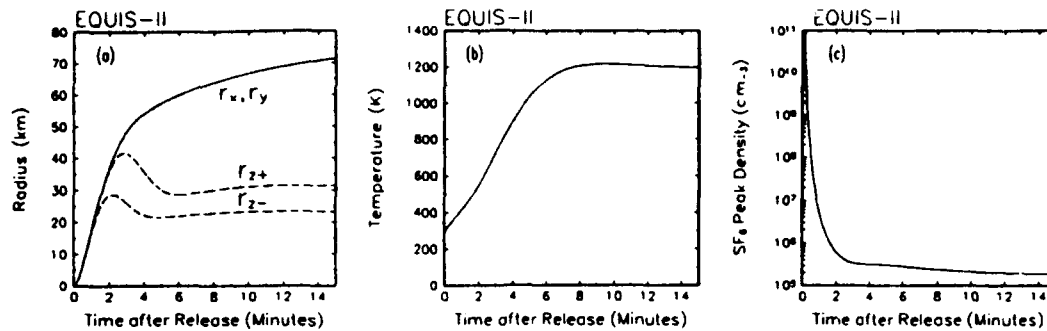


Figure 6. (a) The expansion of the SF₆ cloud limbs. (b) The collisional heating of the SF₆ release cloud. (c) The peak density of the release cloud.

The dense region of the ion cloud should closely follow the 7774Å emission region measured by the Boston University all-sky camera. The horizontal position of the emission region center versus time after release of Table 5 was obtained from the all sky camera images (Michael Mendillo, personal communication). The altitude column of Table 5 is the predicted altitude of the ion cloud center given an downward plasma drift of 15 m/s. The North-South motion of the 7774Å emission should approximate the neutral gas motion since this is parallel to the magnetic field. The East-West motion of the plasma perturbation should couple very rapidly to the background plasma motion. It is assumed that the ion cloud is formed within a chemical time constant of the attachment process (10s). The background plasma East-West motion should be approximately 80% of the neutral wind. Additionally, the vertical motion of the ion cloud is assumed to be coupled to the background plasma motion. Altair measurements suggest that there was no vertical motion of the ionosphere for up to an hour after the release. The background plasma was moving approximately 130 m/s East and 135 m/s South. These numbers were obtained from the observed motion of the 7774Å emission region.

TABLE 5. Airglow center (Michael Mendillo, personal communication).

TAR (s)	Latitude	Longitude	Altitude (km)
42	11.18	167.21	426.1
68	11.30	167.24	425.7
94	11.34	167.28	425.4
120	11.38	167.28	424.4
146	11.34	167.31	424.6
172	11.26	167.35	424.2
198	11.22	167.38	423.8
224	11.22	167.38	423.4
250	11.22	167.45	423.0
276	11.14	167.45	422.6
302	11.18	167.49	422.2

The relative positions of the rockets and perturbation clouds are shown in Figure 7. The predicted ion cloud positions produced by the COM model have an offset of about 17 km east and 17 km north from the 7774Å measurement positions. The Boston University all sky camera position contains uncertainty of approximately 10 km (M. Mendillo, personal communication), which does not account for the entire offset. If the camera position is correct, the velocity required for the gas to reach the first 7774Å measurement position is about 600 m/s, which is larger than the release rocket velocity. The only way this apparent problem may be overcome is if the gas release was directed, i.e., if the release takes place from a single nozzle into space. The gas would accelerate out of the release tank to obtain a directed velocity of 180 m/s (thermal velocity at 300K) with respect to the release rocket velocity. If the directed velocity out of the release tank is northward then the COM prediction could better approximate what was observed.

Another COM model run was done using a directed release of 130 m/s North and 130 m/s East with respect to the release rocket. Figure 8 shows the failure of this particular directed release to account for the 7774Å measured positions. However, the later time positions obtained from the model are closer to the measured positions.

Using the instrument rocket path and the model predictions of the ion cloud path, we note that the rocket-to-ion cloud separation varies only slightly between these cases. The path of the ion cloud differs primarily in the initial minutes after the release. Thus, only slight variations are seen in the ion profiles predicted by several possible ion cloud paths. This provides confidence in the comparisons of data and model results.

The expansion after the release may allow for freezing of the SF₆ gas. The thermal energy of the gas is transferred to directed acceleration from the release rocket. This produces clustering or freezing of the SF₆ molecules and reduces the 7774Å emission signature from the experiment.

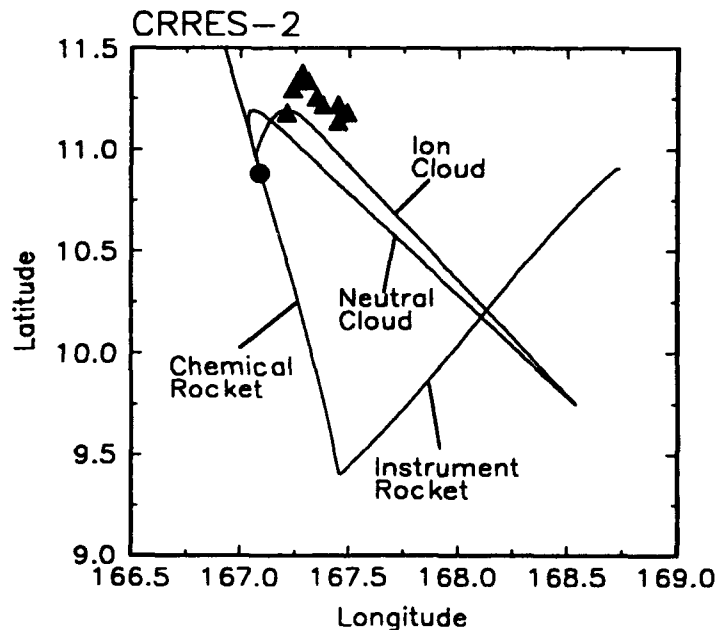


Figure 7. The position of release rocket, instrument rocket, ion cloud and neutral cloud as predicted by the COM model. The circle is the release point. The triangles are the measured positions of the 7774Å emission in Table 5.

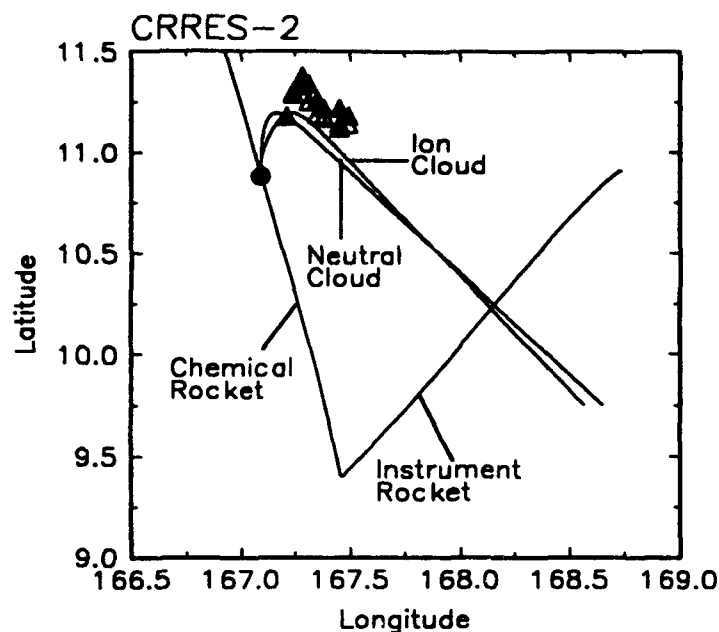


Figure 8. A directed release is modeled with COM program. The ion cloud position is still not able to match the 7774\AA emission positions from Table 5.

3.3 Chemical Perturbation in CRRES-2

Due to the quick coupling of the cloud to the neutral background and the lack of any significant perturbed plasma motion, a simplified three-dimensional model of chemistry and dynamics can be used to simulate the chemical perturbation of the SF_6 release. Using axially symmetric cylindrical geometry in the frame of the ambient neutral wind, the three-dimensional aspects of the neutral motion can be reduced to two-dimensions. Because the plasma is bound to the magnetic field lines, its only motion is parallel to the magnetic field. This cannot be properly modeled in the cylindrical geometry. However, the plasma perturbation can be modeled approximately by solving plasma motion in the plane containing the magnetic field and altitude directions with rectangular coordinates. The combined cylindrical-rectangular, two-dimensional model effectively reproduces a three-dimensional transport result. This simplified transport allows one to use large chemistry sets with less computational demand.

The set of reactions used in the two-dimensional study is larger than in previous studies of ionospheric releases of SF_6 . The reactions of Table 1 are included with several ambient ion reactions to develop airglow predictions and density profiles. Thermodynamic calculations indicated that 40% of the SF_6 may be frozen upon release. The calculation involved large uncertainties. For this reason, three cases were run using 100%, 10%, and 1% free-vapor of SF_6 in release.

The model results were compared to airglow measurements in East-West cross sections, and North-South cross sections of the 7774\AA airglow. The modeled 7774\AA airglow for North-South and East-West cross sections are plotted for the times of several airglow data points – 16, 68, 120, and 250 seconds after the release. Two model runs of the release are presented in Figure 9 and 10. Figure 9 shows the very low emission rates of the SF_6 release chemistry if the SF_6 is initialized with the ambient upper atmosphere temperature of about 1000K. This was suggested by *Bernhardt et al.* [1984]. Hot SF_6 leads almost entirely to SF_5^- ions. The excited oxygen atoms

produced from SF_5^- and O^+ recombination produce ultraviolet emissions. The atmosphere is optically thick to these UV emissions and could not be observed from the ground. Figure 10 shows the very high emission rates of the SF_6 release chemistry. The SF_6 is initialized at the release temperature of 300K and allowed to heat through collisions with the background gases. This allows SF_6^- to be produced for a significant time period (see Figure 6b). The 7774\AA intensities in a cold release of SF_6 are approximately 7 and 1.3 times larger than observed at 16 s and 250 s, respectively.

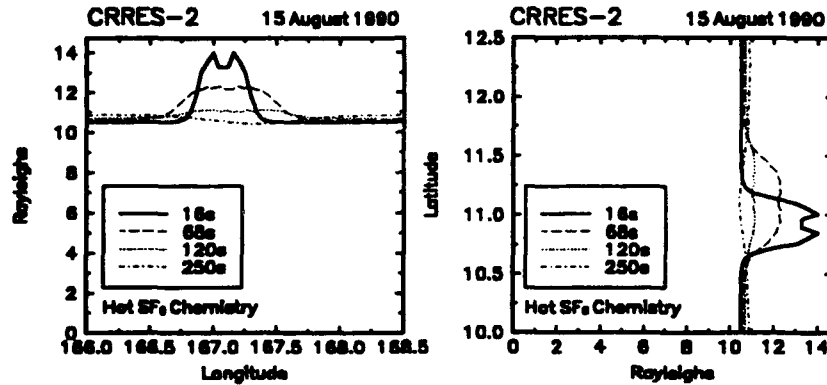


Figure 9. East-West and North-South cross sections of the 7774\AA airglow from the SF_6 release cloud. The 7774\AA intensity is only 4 Rayleighs above the background for this model run. The main characteristic of the run is the assumed initial high temperature of the SF_6 gas. The SF_6 temperature is set at the ambient atmospheric temperature ($\sim 1000\text{K}$).

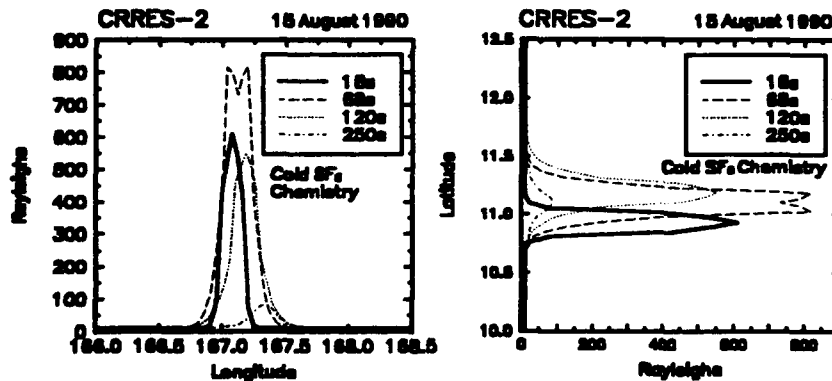


Figure 10. East-West and North-South cross sections of the 7774\AA airglow from the SF_6 release cloud. The 7774\AA intensity is 800 Rayleighs above the background in this model run. The main characteristic of this model is the assumed initial low temperature of the SF_6 gas. The SF_6 temperature is set at the release temperature ($\sim 300\text{K}$) and allowed to collisionally heat in the model.

It may be sufficient to describe present observations if some thermodynamic considerations are taken into account. An apparent problem with interpretation of Red Air I release of CO₂ may be rapid clustering of the CO₂ molecules [Eccles and Hingst, 1993]. This binds the CO₂ and delays the 6300Å airglow emissions that were the main observational diagnostic of the event. Similarly, observations of the SF₆ release experiment of CRRES-at-Kwajalein suggest that the SF₆ freezes or clusters almost totally for the initial half minute of the release, then eventually evaporates to effectively release approximately 10% of the intended total with a delay of almost a minute. Below we will present the evidence supporting this conclusion.

The airglow measurements made by Michael Mendillo's group at Boston University provide an early-time benchmark to assess the chemistry in the model. The all sky camera integrates over a 20 second period. The measurement of the 7774Å airglow cloud show no airglow production until the profile integrated over 32 to 52 seconds (label 42 seconds). This suggests either (1) initial complete freezing (clustering) of the SF₆ release or (2) complete snowplow of local plasma density within the release cloud for 30 seconds. The first proposed explanation is not necessarily unexpected. A thermodynamic model of the SF₆ releases [Bernhardt, 1988] predicts 40% freezes during the expansion. However, the calculation did not include partition of energy into translational acceleration of the gas. Much of the thermal energy of the SF₆ gas goes into directed expansion out of the nozzle, thus, more than 40% may be frozen or clustered. Soon after acceleration of the release gas, self-collisions will allow clustering or freezing the SF₆ molecules. Subsequent collisions with the hot ambient background will release SF₆ molecules, which then can participate in attachment chemistry. The second proposed explanation -- snowplow effects -- can also reduce the initial 60 seconds of airglow production. The SF₆ cloud is dense in the first half minute (Figure 6). The density must be above 10¹⁰ cm⁻³ to have mean-free-path less than 1 km. This situation is maintained for up to 20 s causing significant reduction of O⁺ within the release.

Even if snowplow effects can explain the early time reduction of airglow, the airglow measurements after 200 s indicate only 10 percent of the SF₆ is available for chemistry (Figure 11). The all sky camera unfortunately saturated at 125 Rayleighs intensity but the early and later time peak 7774Å emissions can be compared to model runs with release of (a) 100%, (b) 10%, and (c) 1% of vapor SF₆. The 10% vapor (90% freezing) run follows the measured peak intensity after the camera is no longer saturated.

The late-time chemical system was observed by a second rocket fly-through at approximately 900 s after the release. The rocket trajectory and modeled ion cloud trajectory (Figure 8) were used to provide time history profiles of modeled IMS observations. The resulting picture suggests similar conclusions to the airglow observations at earlier times.

The resulting measured and modeled IMS profiles are compared in Figure (12). Examination of the three model profiles (Figure 12) suggest that 10% vapor (90% freezing) provides the best result for F⁻, SF₅⁻, SF₅⁺ densities. This is in agreement with the airglow data conclusions. Additionally, F⁻ as the dominant ion requires the chemical mechanism proposed by Hunton *et al.* [1987].

In all simulations, there were no significant amounts of SF₄⁻ produced. This differs from the actual experiment where SF₄⁻ was observed to have similar densities as SF₆⁻ and SF₅⁻. Electron attachment of SF₄ is the only avenue of production included in the simulations. Very high temperatures are required to produce SF₄⁻ from dissociative attachment of SF₆ and SF₅. The apparent discrepancy between simulation and experiment suggests that (1) there is another avenue of production for SF₄⁻, (2) the electron attachment rate has been underestimated, or (3) the IMS is measuring something other than SF₄⁻. The first and second explanations appear less likely than then third. The Mass Spectrometer used in the CRRES-at-Kwajalein experiment has a resolution of about 3 amu. The mass of SOF₃⁻ (105 amu) is only 3 amu lower than SF₄⁻ (108 amu). SF₄⁻

and SOF_3^- densities would be combined in the measurement (D. E. Hunton, personal communication). The measurement might instead predict the presence of SOF_3^- . The simulation results agree qualitatively with this experimental interpretation (Figure 13).

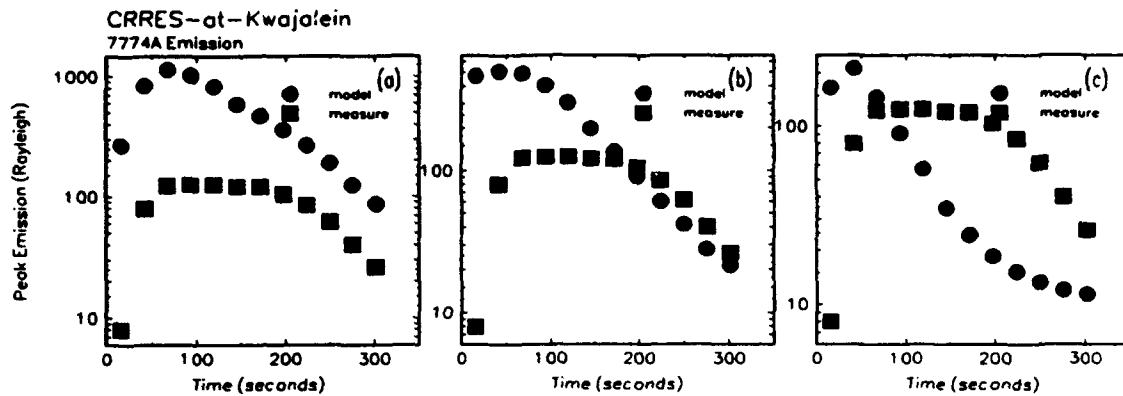


Figure 11. Peak 7774Å airglow obtained from model and All sky camera. Model release of a) 1.4×10^{26} SF_6 molecules (no freezing), b) 1.4×10^{25} SF_6 molecules (90% freezing), and c) 1.4×10^{24} SF_6 molecules (99% freezing).

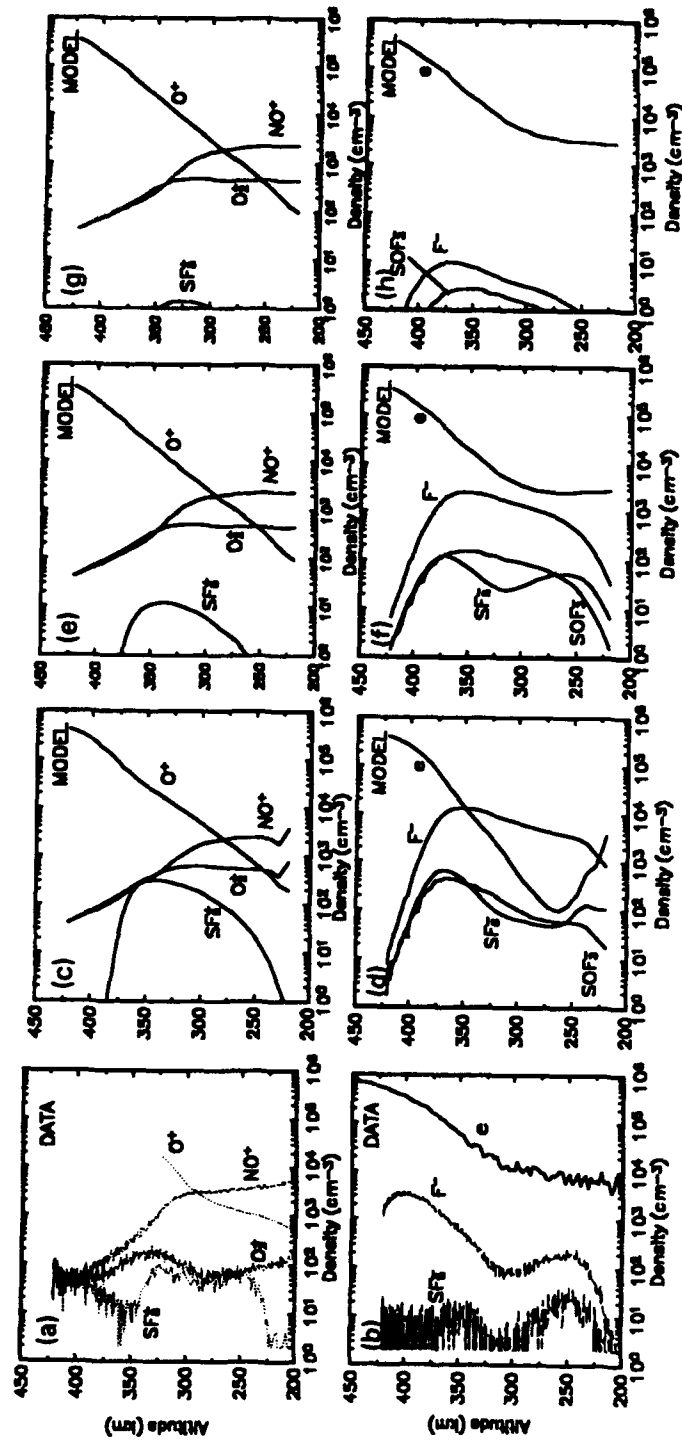


Figure 12. (a,b) IMS data, (c,d) release is 100% vapor, (e,f) release of 10% vapor, (g,h) release of 1% vapor. All profiles are from the downleg of observation rocket.

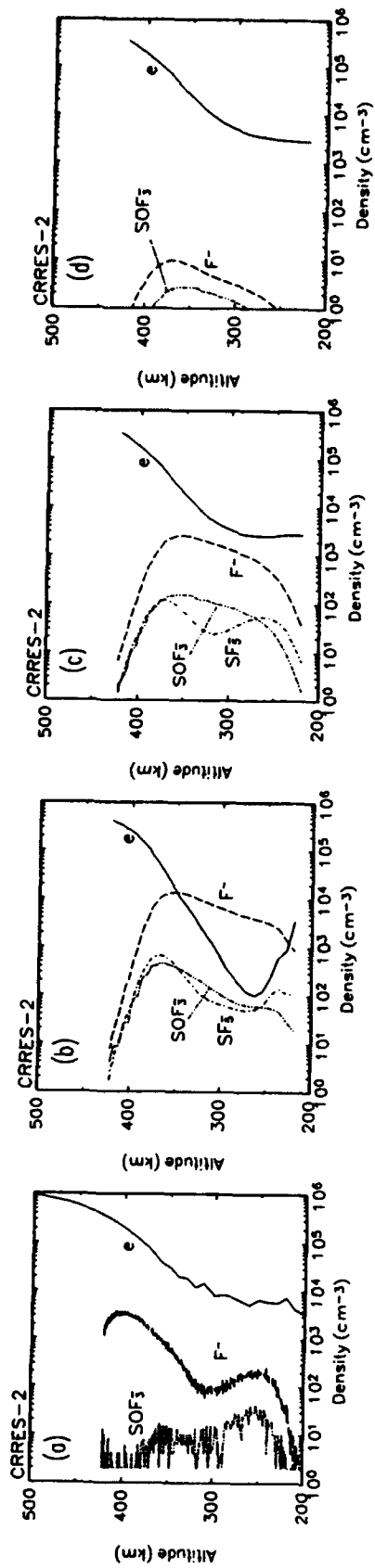


Figure 13. (a) IMS data, (b) release is 100% vapor, (c) release of 10% vapor, (d) release of 1% vapor. All profiles are from the downleg of observation rocket.

3.4 Electrodynamic Perturbation from an SF₆ Release

The motion of plasma perturbations in the equatorial ionosphere requires knowledge of the background plasma motion. The neutral wind blows plasma freely along the horizontal magnetic fields at the equator. The motion perpendicular to B is defined by the electric field. The bulk plasma moves as $E \times B$. The global electric field system at the equator is generally defined by the interaction of the magnetic field, neutral atmosphere, and ionosphere. The large-scale electric field provides the zeroth-order motion of the ionosphere. The primary ionospheric current system is the Solar Quiet (Sq) system. The Sq system is modeled with reasonable success using solar-driven, tidal-mode wind models and an E region conductivity model [Richmond *et al.*, 1976].

General trends of the equatorial electric fields are reviewed in Fejer [1981]. During the day the ionospheric plasma near the equator rises at 10 ms^{-1} due to the eastward electric field created by the Sq current divergences. The F region profile appears to remain stationary due to the continual production of plasma in the F₁ region. However, after sunset the production ceases and the F region profile rises. The evening F₁ region chemically decays causing the bottomside F region ledge to steepen. The evening decay of E and F₁ region plasma reduces conductivity and causes an increase in polarization electric fields after sunset [Rishbeth, 1971]. At sunset the enhancement of the downward-directed electric field drives the plasma eastward at about the same velocity as the thermospheric winds (100 to 200 ms^{-1}). The F region horizontal drift is fairly constant from night to night and easily predicted from a knowledge of conductivities and the neutral wind magnitude. Unfortunately, a self-consistent electric field model is computer intensive and does not give the desired detail needed for the evening region of the ionosphere. A simplified predictive model of the equatorial electric fields can be obtained from input of average ambient conditions (neutral densities, neutral winds, plasma densities, F and E region conductivities) [Haerendel *et al.*, 1991]. The calculation of large-scale electric fields ($> 5 \text{ km}$) can be treated as a two-dimensional problem where the important ionospheric quantities are integrated along flux-tubes. The vertical electric field is approximately given by

$$E_L = - \left(\frac{\int \sigma_P u_n \gamma dl}{\Sigma_P} \right) + \frac{\Sigma_H E_\phi}{\Sigma_P} \quad (3.8)$$

where E_L is the vertical electric field, E_ϕ is the west-to-east electric field, σ_P is local Pedersen conductivity, u_n is the zonal neutral wind, Σ_H is fieldline integrated Hall conductivity, and Σ_P is fieldline integrated Pedersen conductivity [Haerendel *et al.*, 1991; Anderson and Mendillo, 1983]. Integrations are performed along the magnetic field line (dl) with γ as a geometry factor of the flux tube. Figure 14 shows the integrated conductivities of the evening ionosphere. Figure 15 shows the resulting E_L given a neutral wind of 150 ms^{-1} , $E_\phi = 1 \text{ mVm}^{-1}$ and $B = 0.25 \times 10^{-4} \text{ T}$. The resulting horizontal motion has a shear at the F region ledge. Above the shear the velocity is eastward and below it is westward.

Throughout the day the F region plasma moves upward at about 15 ms^{-1} . Near sunset the plasma vertical velocity (horizontal electric field) grows in magnitude to 30 - 70 ms^{-1} for about 1 to 2 hours. After the enhancement, the ionosphere drops rapidly (20 ms^{-1}) and continues to have a downward velocity through the remainder of the night. The evening enhancement of the rise velocity has been the focus of scientific study due to its correlation with the occurrence of ESF. Unfortunately, the vertical rise velocity is extremely variable from night to night and difficult to predict.

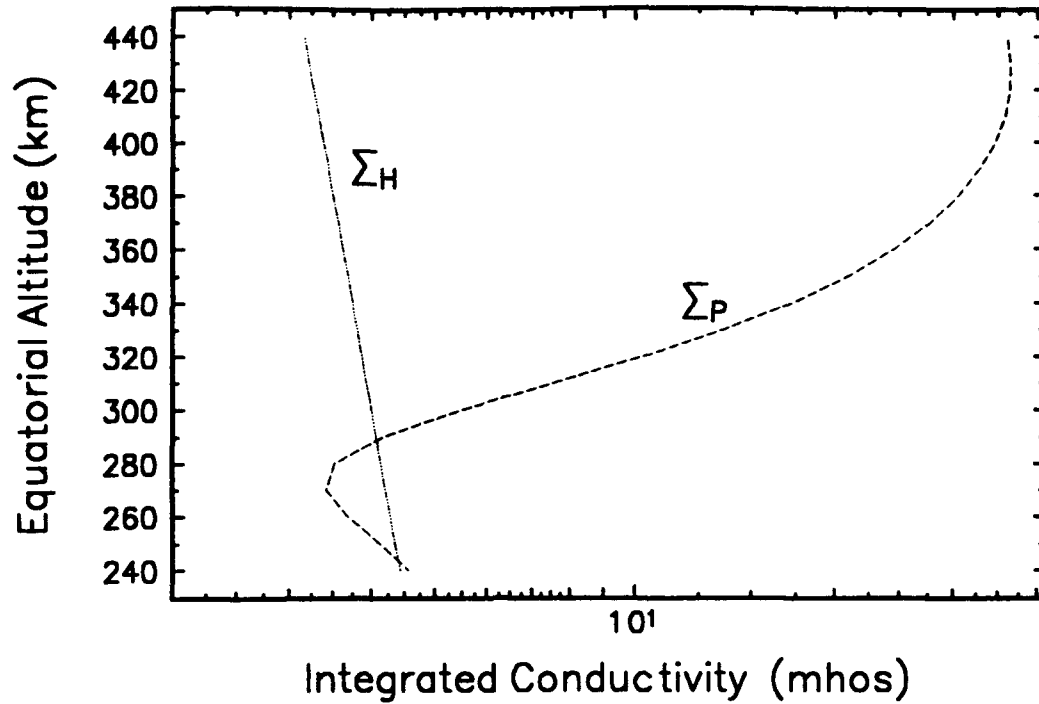


Figure 14. Integrated conductivities of the evening ionosphere.

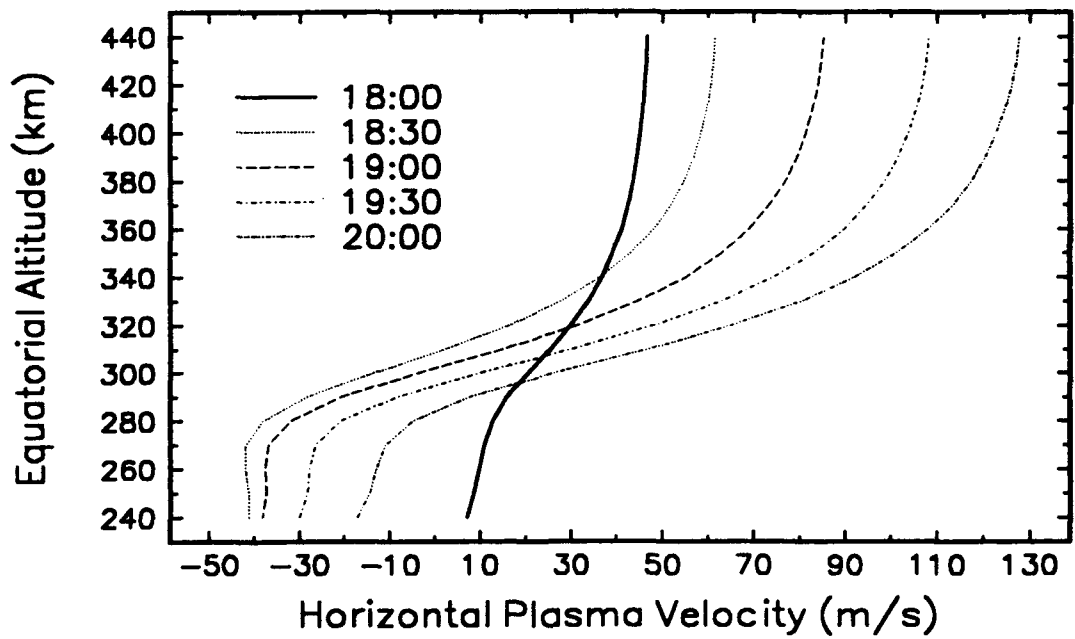


Figure 15. The shear of the horizontal plasma motion derived from the ionospheric conductivities shown in Figure 14. The corresponding vertical electric-field strength is shown on the top axis.

The time history of the horizontal electric field can be modeled given integrated ionospheric quantities and $E_x(t)$ (rise velocity) [Haerendel *et al.*, 1991]. The horizontal electric field moves the F region upward. The rise alters the conductivity-weighted neutral wind in Equation (3.8). The shear feature in the horizontal velocity rises (and falls) with the F region. The above electric field model completes the necessary picture of the ambient conditions of neutral atmosphere, ionosphere, and associated electric fields. One can now introduce the chemical perturbations to the background electrodynamic and study electrodynamic in the region near the cloud.

A two-dimensional, electrodynamic model was developed to solve for the motion of the perturbed plasma region. The electrodynamic model is reduced to a potential equation with source terms. The source terms are determined by gravitationally-generated and neutral-wind-generated currents perpendicular to the magnetic field. The method used is similar to that described in Haerendel *et al.* [1991] and Cakir *et al.* [1991]. The background ionosphere is modeled with field-line integrated quantities excluding the 30 km slice containing the main perturbation of the SF₆ release.

The chemistry and motion of the cloud are followed using local quantities. The reaction set used is simplified in order to reduce the number of species in the two-dimensional calculation. The reduced reaction set only models the deep electron hole well. The extended chemical perturbation will not be modeled well with the limited chemistry. This chemical approximation is appropriate for determining the electrodynamic effect of the SF₆ release. The background ionosphere is connected to the slab containing the cloud via equipotential magnetic field-lines.

The resulting perturbation of the integrated Pederson conductivity shown in Figure 16a, is very small due to the low collision frequencies at the high altitude of the release. The largest electrodynamic perturbation is due to the mass loading of the field-lines. This generates greater gravitational current in the region of dense SF₆⁻ (Figure 16b). The mass of the SF₆⁻ plasma is still only a fraction of the integrated mass of the flux tube. However, it is sufficient to cause an electrodynamic perturbation. The horizontal plasma velocity perturbation is largest in the vertical direction (horizontal electric field perturbation) (Figures 16c), because the gravitationally-generated current is horizontal. The vertical velocity perturbation is significant up to 60 s after the release and should be greater in the early seconds of the release (Figure 16d). However, due to the rapid decay of the molecular negative-positive ion plasma within the cloud region, the velocity perturbation also will decay rapidly. This is not true of an atomic ion perturbation.

The electrodynamic within the SF₆⁻ cloud causes the plasma cloud to drop in altitude. A net drop in the plasma flux tube containing the ion cloud causes adjacent regions to rise. Any plume development comes from these adjacent regions of the SF₆⁻ cloud. As the negative-positive plasma recombines, the net plasma loss causes the perturbed region to slow. It could eventually rise when the mass in the perturbed region is less than the surrounding region.

The quick decay of the velocity field perturbation suggests that the SF₆ release will not stimulate large-scale plume structures associated with ESF. However, the steep sides of the plasma perturbation in the local release volume provide a free-energy source from which small-scale irregularities can grow. The short wavelength perturbations can develop without coupling to the extended ionosphere.

The horizontal velocity perturbation always remains small and the perturbation region moves at nearly 99% of the ambient horizontal velocity. The expected position of the plasma perturbation can be determined by simply following the ambient motions of the ionosphere from the initial release position.

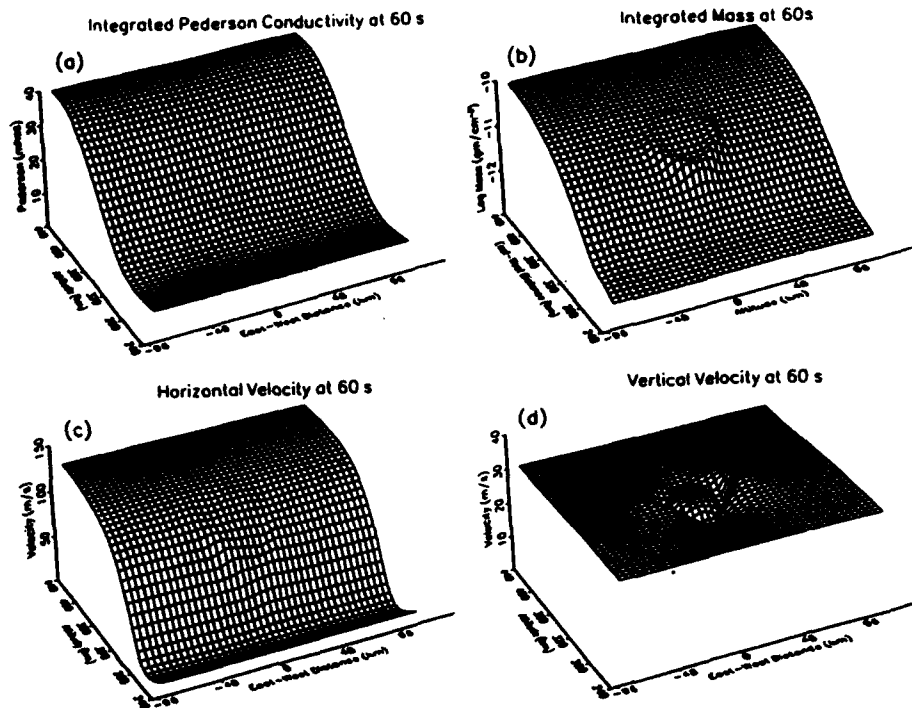


Figure 16. (a) The field-line integrated Pederson conductivity. (b) The field-line integrated ion mass. (c) The horizontal plasma velocity. (d) The vertical plasma velocity. The time is 60 s after the SF_6 release.

4. DISCUSSION OF SF_6 RELEASES

A thorough examination of the possible chemistry associated with an SF_6 release in the ionosphere has been performed. In making comparisons of simulations and field experiments it was necessary to simulate dynamics, electrodynamics and experimental measurement procedures in the numerical calculations. Favorable comparisons between the experiment and simulation of the SF_6 release give greater confidence in interpreting the simulation and experimental data. Any differences between the simulation results and experimental observation of the SF_6 release could reside in the oversight of significant reactions, ignorance of temperature dependencies of known reactions, and/or difficulties in combining complex chemistry with geometrically realistic transport models. The findings obtained pertaining to the release of SF_6 in the ionosphere as reported above are summarized below.

- i. The plasma perturbation motion suggests that the large-scale electric fields generated by the perturbed field-line electrodynamic quantities are small in magnitude and short in duration. The perturbed plasma region moves approximately with the background plasma. This suggests that the artificial seeding of equatorial spread F is unlikely to cause large-scale plasma plumes. Small-scale irregularities (< 1 km) can still form on the sharp gradients in the local quantities of plasma density, conductivity, etc.
- ii. The extent of the electrodynamically perturbed region is approximately 25 km in radius. This is the region of the deep electron hole. The extent of the chemically perturbed region was determined to be very large ($r > 200$ km). The broad extent

- is due to the high altitude of the release point, which allows the broad expansion of the SF₆ cloud.
- iii. Due to the large heat capacitance of SF₆, the SF₆ release gas heated slowly. This allows for significant levels of 7774 Å airglow production, though the model predicted more airglow than was observed. The all sky camera does not measure any 7774 Å emission from the release position until 42 seconds after the release time. This delayed emission may indicate that the SF₆ freezes or clusters completely during the initial expansion. The slow rise of the 7774 airglow suggests an evaporation process taking place over a 1 or 2 minute period. The later time (~4-6 minutes) airglow measurements and the ion species profiles measured by the IMS (~15 minutes) best agree with about 10% - 20% of the total SF₆ evaporating over the initial minutes after the release.
 - iv. Previously suggested SF₆ chemistry [Mendillo and Forbes, 1982; Bernhardt, 1984; Hunton et al., 1987] appears to be sufficient for the initial chemistry of an SF₆ release (near the release point). SF₆⁻ production is large in this central region. The saturation of the all-sky camera measurement of 7774 Å airglow is evidence for the production of SF₆⁻ near the release point.
 - v. F⁻ is the dominant negative ion when the observation rocket flies through the perturbed region. The unexpected dominance of F⁻ is explained well by the charge interchange mechanism given in Hunton et al. [1987].
 - vi. Chemistry simulations indicated that in the late time (>5 min), oxidation of SF_n is potentially important. Several neutral species produced later in the SF₆-ionospheric chemistry are electron attachers. SOF₃⁻ is probably an important late-time negative ion.
 - vii. SF₄⁻ densities in experimental observations are much higher than simulation predictions. However, the mass spectrometer resolution does not have the necessary resolution to separate the masses of SOF₃⁻ and SF₄⁻. Therefore, the density of SOF₃⁻ predicted in the simulation may account for the SF₄- channel IMS measurement.

The findings of the simulation and experiment comparisons can be used to suggest directions for the continued study. The recommendations below focus on the attempt to resolve the apparent differences between simulation and experimental CRRES SF₆ release.

While the large-scale electric fields are not perturbed greatly by an equatorial release of SF₆, small scale irregularities can be formed and observed. Simulations of the development of the small scale irregularities would provide insight into the timing of probable observations of the irregularity onset in a positive-negative ion plasma. The dynamic and electrodynamic implications of the negative-positive ion plasma in the F region are still unexplored. The late-time modeling of the depleted plasma tube can be examined in simulation to determine the time constant for refilling of the electron hole and plasma hole. Questions about the extent of the depletion along a magnetic field line could have possible ramifications on how big the long term electrodynamic perturbation is. If the perturbation has a long life, then a release of SF₆ on the F region ledge prior to the pre-reversal enhancement may have a more destabilizing effect than a later release. The present models can suggest optimal altitudes and times for a release to seed ESF phenomenon.

Several potentially important attachment cross sections have not been published (SF₅, SOF₄, and other molecules). Additionally, many basic chemical processes are only estimated. Products and rates of ion-ion recombination are, in general, only estimated in this study. Associative deattachment reactions are in general unknown and left out of the present modeling.

Observation of the spatial distribution of 1304Å and 1356Å emissions along with 8446Å and 7774Å emissions would provide strong indicators of the regions where SF₆⁻ or SF₅⁻ production is taking place. The 1304Å and 1356Å emissions must be observed from a space-based platform such as the RAIDS satellite since the atmosphere is optically thick for these emissions.

5. CO₂ RELEASES IN THE F REGION

Optical signatures of chemically induced ionospheric holes from rocket exhaust or release experiments have been measured and modeled for three decades [Booker, 1961; Mendillo and Forbes, 1978; Zinn and Sutherland, 1980; Mendillo and Baumgardner, 1982]. Releasing CO₂ in the F region allows for observations of CO₂ chemistry in a time-dependent regime which is difficult to study in the laboratory. The Red Air I (Release Experiments to Derive Airglow Inducing Reactions) Program released 9 kg of CO₂ at 253 km and again at 379 km altitude in the mid-latitude nighttime ionosphere from a single rocket. The strategic release altitudes help to isolate key chemical processes to determine reaction rates of CO₂/ionospheric chemistry.

The presence of CO₂ in the ionospheres of Venus and Mars as well as the exhaust effluents of some rocket engines make the study of CO₂ reactions an important endeavor. CO₂ is an important perturbing chemical in the high ionosphere (z > 200km) of the earth. It is not naturally present in any significant density but the ambient plasma is perturbed strongly by the release of CO₂. This is because the reaction rate of O⁺ with CO₂ is 2 and 3 orders of magnitude greater than O⁺ with O₂ and N₂, respectively. A CO₂ release in the F region ionosphere rapidly changes the plasma from an atomic to a molecular ion plasma, thus increasing the rate of ion-electron recombination.

The primary reactions of CO₂ in the F region are:



The total rate of the combined reactions (5.1-5.2) is approximately $9.4 \times 10^{-10} \text{ cm}^3 \text{ s}^{-1}$ and does not depend greatly on temperature. However, the branching of the CO₂-O⁺ reaction does vary strongly with reaction energy [Fehsenfeld *et al.*, 1966; Paulson *et al.*, 1966; Dunkin *et al.*, 1968; Mosesman and Huntress, 1970; Johnsen *et al.*, 1970; Lindinger *et al.*, 1974; Jaffe and Klein, 1974; Viggiano *et al.*, 1990a and 1990b]. Implications of the branching energy dependence for ionospheric release of CO₂ have been discussed in Caledonia *et al.* [1987] and Hunton *et al.* [1990]. At low energies, <1 eV, the charge interchange branch is dominant. In rocket release experiments, this CO₂-O⁺ interchange produces O₂⁺ and, eventually, 6300Å airglow. At higher energies the charge exchange branch dominates. The same branching trends are observed with both vibrational energy and translational energy (A.A. Viggiano, private communication). Additionally, the population distribution of the vibrational states of the produced O₂⁺ varies with temperature [Viggiano *et al.*, 1990a]. This results in a change in the vibrational population of O₂⁺ and altered branching ratios of dissociative recombination [Guberman, 1988].

Due to the rarefied conditions of an upper atmospheric release of CO₂, NLTE (non-local thermal equilibrium) conditions hold. Under such conditions the vibrational state populations of molecular neutrals and ions can depart from Boltzmann distributions. Chemical rate coefficients obtained under LTE conditions may be a misrepresentation within models of chemical release. Explicit vibrational dependencies in rate coefficients and products are potentially important in modeling such NLTE environments.

The molecular ion plasma produced in a CO₂ release has observable effects. A large release might lead to a long-lived plasma depletion through increased recombination rates and to a 6300Å airglow enhancement through the radiative decay of O(¹D) produced in the recombination of O₂⁺:



and possibly in the recombination of CO₂⁺



The 6300Å emission perturbation and the electron density depletion provide signatures of the CO₂-ionospheric chemistry and time-dependent airglow chemistry.

CO₂-ionospheric chemistry has been used to model 6300Å airglow production in CO₂ releases from exhaust plumes [Mendillo and Baumgardner, 1982]. There were indications that the observed 6300Å intensity was less than the value predicted by the chemistry model.

The Red Air I Campaign attempted to place CO₂ releases above and below the F peak. For these two release points, the electron densities would be similar but the neutral background would give different characteristics in diffusion and chemical constituent concentrations. Measurements of the time-dependent airglow perturbations at two separate altitudes in the F region have the potential to provide definitive information on unresolved questions of nighttime airglow chemistry and CO₂ chemistry. If published CO₂-O⁺ reaction rates are accurate, then CO₂ releases at several altitudes can be used to find quenching rates of O(¹D) by ground state O. At altitudes below 250 km N₂ quenching of O(¹D) dominates. Above 290 km radiative quenching dominates. Near 270 km altitude O quenching of O(¹D) may be important. This quenching reaction, first suggested by Yee and Dalgarno [1985], could alter predicted airglow profiles for daytime, nighttime and auroral ionospheres. Some investigators suggest that quenching by O is not needed to explain experimental observations [Link and Cogger, 1988] (also see, Bates [1989]).

This investigation examines the chemistry and thermodynamics of a cold CO₂ release in the F region of the ionosphere. The direct comparison of model results and Boston University all sky camera observations made during Red Air I experiment. The discrepancy between model results and observations of the Red Air I releases indicates that either (1) CO₂-O⁺ reaction rates in the literature are much too fast, or (2) complex thermodynamic processes are occurring that degrade the intended simplicity of the experiment. Several questions are examined in numerical simulations of the Red Air I release to explain the observed airglow signatures. First, what processes can produce the less-than-expected airglow emission from the CO₂ release region? Second, what processes can lead to a bimodal decay curve observed in the high altitude release?

Because the primary observable in the Red Air I experiment is 6300Å emission from radiative decay of O(¹D), it was necessary to examine nightglow chemistry models. The reaction set necessary for ambient O(¹D) production and loss is reviewed elsewhere [Torr and Torr, 1982; Link and Cogger, 1988; Solomon et al., 1988; and Solomon and Abreu, 1989]. The background 6300Å airglow during Red Air I was measured and is modeled as an additional baseline input into the study of CO₂ ion-chemistry. Simulations use two separate airglow chemistry sets -- airglow chemistry suggested by Link and Cogger [1988] and the chemistry suggested by Solomon and Abreu [1989]. In the near steady-state conditions of the ambient nighttime airglow, ground measurements of the integrated airglow intensities cannot distinguish between the two chemistry sets [Link and Cogger, 1988]. However, the time-dependent, altitude-specific effects of the CO₂ releases forces one to consider the differences between the assumed rates.

Section 2 is a description of the Red Air I experiment. Section 3 of the paper discusses ambient airglow chemistry and implications of the Red Air I optical observations reported by Michael Mendillo [personal communication]. Section 4 examines the results from

multidimensional release modeling. Section 5 presents the simulations of the Red Air I CO₂ releases using several more complex chemical models. Conclusions of the paper are in Section 6.

6. RED AIR I EXPERIMENT DESCRIPTION

The Red Air I Campaign attempted to place CO₂ release above and below the F peak. For these two release points, the electron densities would be similar but the neutral background would give different characteristics in diffusion and chemical constituent concentrations. A single rocket carried both release canisters. One was released at 253 km altitude (2:29 UT) and the other at 379 km altitude (2:32 UT). Table 6 provides the geosolar conditions for the night of the Red Air I release experiment.

Table 6. Release Conditions.

Launch	3 April 1989
10.7cm Flux	184
<10.7cm Flux>	196
Sunspot Number (Ra)	218
Geo-Longitude	284.6° E
Geo-Latitude	37.8° N
Ap Index	21
Kp Index	27
Release Altitudes	379 km and 253 km
Local Solar Time	21:30

The Millstone Hill radar measured the electron density profile, electron temperature, and ion temperature during the time of the airglow measurements. The MSIS90 neutral atmosphere model [Hedin, 1991] predicts an exospheric temperature of 1200K for the geophysical parameters of the Red Air I releases. The neutral exospheric temperature of the MSIS model atmosphere was set equal to the measured ion temperature of the Red Air I experiment (1030K) [Mendillo, personal communication, 1991].

All sky camera observations of the 6300Å airglow enhancement showed an enhancement of 75 Rayleighs over the background for the upper release of CO₂. The enhancement was immediate (< 1 minute) and decreased approximately as a simple decay curve, though the decay curve had a bimodal characteristic suggesting the presence of other processes beyond simple CO₂-ionospheric chemistry (Figure 17).

The observation of the low-altitude release showed a peak enhancement of 25 Rayleighs over the background. The enhancement time history of the lower release had a more pronounced hump characteristic. The double rise of airglow at the low-altitude release positions also suggests that processes other than simple CO₂ chemistry may be involved in the perturbation evolution. Note that the second pronounced rise in the low-altitude release measurement corresponds to the release time of the high-altitude release.

It is important to examine release characteristics, species transport, and chemistry in order to fully interpret the Red Air I experiment. Rather than being a definitive experiment to quantify questions on ambient airglow and CO₂ ion chemistry, the experiment is instead an investigation into unexpected thermodynamic and chemical processes.

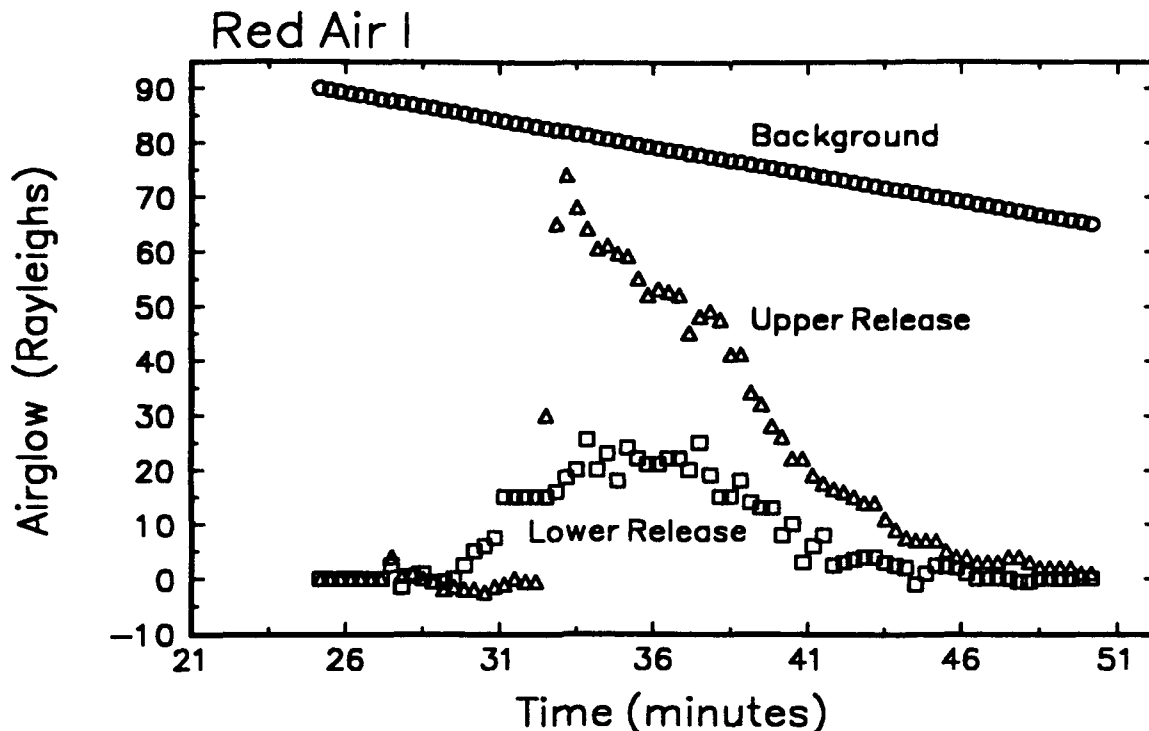


Figure 17. Airglow measurements from a 4 by 4 degree region centered on the upper release (triangles), centered on the lower release (squares), and on the undisturbed background (circles). The background measurements are smoothed.

7. NIGHTTIME BACKGROUND AIRGLOW

While metastable species are only trace constituents in the atmosphere, they have significant roles in the chemistry and thermal budget of the atmosphere. Long radiative lifetimes permit conversion of electronic energy to kinetic or vibrational energy through quenching processes. In addition, the long-lived metastable species allow for energy transport away from the region of the metastable species formation. The metastable species $O(^1D)$ provides one of the strongest features in airglow and auroral spectra. Due to the relative simplicity of the chemistry of the nighttime mid-latitude ionosphere, nightglow measurements from this region can help resolve rate coefficient discrepancies of the $O(^1D)$ sources and sinks. The ambient reactions used to model airglow production are given in Tables 7 and 8.

While *Hays et al.* [1978] used Atmosphere Explorer (AE) satellite nightglow measurements to determine quenching rates and yields of $O(^1D)$, *Cogger et al.* [1980] used the chemistry of *Hays et al.* [1979] to predict nighttime 6300Å airglow and compared the prediction to ground-based measurements. They concluded that the chemistry predicted airglow intensity at twice the observed intensities from $O(^1D)$ decay. Through the inclusion of several new rate determinations, *Link and Cogger* [1988] reexamined the ground-based work of *Cogger et al.* [1980] and resolved the discrepancies. However, some issues of $O(^1D)$ nightglow chemistry remain (for a full discussion see *Link and Cogger* [1988]).

The primary issue highlighted in *Link and Cogger* [1988] (henceforth LC) is the quenching of $O(^1D)$ by ground state atomic oxygen. The nightglow chemistry put forward by *Solomon and Abreu* [1989] (henceforth SA) includes a non-zero rate for this quenching reaction. The differences between the LC and SA chemistry sets center on the use of $6.81 \times 10^{-3} \text{ s}^{-1}$ and $9.41 \times 10^{-}$

$^3\text{s}^{-1}$, respectively, for the Einstein coefficient of the $\text{O}(^1\text{D})\text{-O}(^3\text{P})$ transition. To agree with observed airglow values SA included the quenching of $\text{O}(^1\text{D})$ by atomic oxygen



with a suggested rate of $8 \times 10^{-12} \text{ cm}^3\text{s}^{-1}$. LC stated that the quenching of $\text{O}(^1\text{D})$ by radiative decay (3.9) is not needed if a smaller Einstein coefficient for $\text{O}(^1\text{D})$ radiative decay is used.

A steady-state model of the ionosphere was used to investigate the background integrated airglow associated with the Red Air I release experiments. The model assumes the ionospheric constituents are in chemical equilibrium. The ion constituents can be determined from a measured electron density profile, given neutral density profiles, and a set of rate coefficients for the reactions listed in Tables 7 and 8.

Table 7. Nighttime airglow chemistry.

DISSOCIATIVE RECOMBINATION	
$\text{N}_2^+ + \text{e} \xrightarrow{k_1} \text{N} + \text{N}$	$k_1 = 1.9 \times 10^{-7} (T_e/300)^{-0.4}$
$\text{NO}^+ + \text{e} \xrightarrow{k_2} \text{N} + \text{O}$	$k_2 = 4.0 \times 10^{-7} (T_e/300)^{-0.9}$
$\text{O}_2^+ + \text{e} \xrightarrow{k_3} \text{O} + \text{O}$	$k_3 = 2.0 \times 10^{-7} (T_e/300)^{-0.7}$
CHARGE EXCHANGE	
$\text{N}^+ + \text{O} \xrightarrow{k_4} \text{O}^+ + \text{N}$	$k_4 = 2.0 \times 10^{-12}$
$\text{N}^+ + \text{NO} \xrightarrow{k_5} \text{NO}^+ + \text{N}$	$k_5 = 6.0 \times 10^{-10} (T_n/300)^{0.27}$
$\text{N}^+ + \text{O}_2 \xrightarrow{k_6} \text{O}_2^+ + \text{N}$	$k_6 = 3.0 \times 10^{-10}$
$\text{O}^+ + \text{N}(^2\text{D}) \xrightarrow{k_7} \text{N}^+ + \text{O}$	$k_7 = 1.3 \times 10^{-10}$
$\text{O}^+ + \text{NO} \xrightarrow{k_8} \text{NO}^+ + \text{O}$	$k_8 = 8.0 \times 10^{-13} (T_n/300)^{-0.2}$
$\text{O}^+ + \text{O}_2 \xrightarrow{k_9} \text{O}_2^+ + \text{O}$	$k_9 = 2.0 \times 10^{-11} (T_n/300)^{-0.7}$
$\text{N}_2^+ + \text{O} \xrightarrow{k_{10}} \text{O}^+ + \text{N}_2$	$k_{10} = 1.0 \times 10^{-11} (T_n/300)^{-0.23}$
$\text{N}_2^+ + \text{NO} \xrightarrow{k_{11}} \text{NO}^+ + \text{N}_2$	$k_{11} = 3.3 \times 10^{-10}$
$\text{N}_2^+ + \text{O}_2 \xrightarrow{k_{12}} \text{O}_2^+ + \text{N}_2$	$k_{12} = 5.0 \times 10^{-11} (T_n/300)^{-0.8}$
$\text{O}_2^+ + \text{N}(^2\text{D}) \xrightarrow{k_{13}} \text{N}^+ + \text{O}_2$	$k_{13} = 2.5 \times 10^{-10}$
CHARGE INTERCHANGE	
$\text{N}^+ + \text{O}_2 \xrightarrow{k_{15}} \text{O}^+ + \text{NO}$	$k_{15} = 4.0 \times 10^{-11}$
$\text{N}^+ + \text{O}_2 \xrightarrow{k_{16}} \text{NO}^+ + \text{O}$	$k_{16} = 4.4 \times 10^{-12} \exp[-3220/T_n]$
$\text{O}^+ + \text{N}_2 \xrightarrow{k_{17}} \text{NO}^+ + \text{N}$	$k_{17} = 1.2 \times 10^{-12} (T_n/300)^{-1.0}$
$\text{N}_2^+ + \text{O} \xrightarrow{k_{18}} \text{NO}^+ + \text{N}$	$k_{18} = 1.4 \times 10^{-10} (T_n/300)^{-0.44}$
$\text{O}_2^+ + \text{N} \xrightarrow{k_{19}} \text{NO}^+ + \text{O}$	$k_{19} = 1.8 \times 10^{-10}$

Table 7. (continued) Nighttime airglow chemistry.

$N + NO \xrightarrow{k_{20}} N_2 + O$	$k_{20} = 3.6 \times 10^{-11}$
$N + O_2 \xrightarrow{k_{21}} NO + O$	$k_{21} = 4.4 \times 10^{-12} \exp[-3220 / T_n]$
$N(^2D) + NO \xrightarrow{k_{22}} N_2 + O$	$k_{22} = 6.0 \times 10^{-11}$
$N(^2D) + O_2 \xrightarrow{k_{23}} NO + O$	$k_{23} = 8.8 \times 10^{-12} (T_n / 300)^{0.5}$
$N(^2D) + O \xrightarrow{k_{24}} N + O$	$k_{24} = 1.9 \times 10^{-12}$
$N(^2D) + N_2 \xrightarrow{k_{25}} N + N_2$	$k_{25} = 9.4 \times 10^{-14} \exp[510 / T_n]$
$N(^2D) + O_2 \xrightarrow{k_{26}} N + O_2$	$k_{26} = 5.3 \times 10^{-12}$
$N(^2D) + e \xrightarrow{k_{27}} N + e$	$k_{27} = 3.9 \times 10^{-10} (T_e / 300)^{0.81}$
$N(^2P) + O \xrightarrow{k_{28}} N + O$	$k_{28} = 1.5 \times 10^{-11}$
$N(^2P) + e \xrightarrow{k_{29}} N + e$	$k_{29} = 2.8 \times 10^{-9} (T_e / 300)^{0.5}$
$O(^1D) + O \xrightarrow{k_{30}} O + O$	$k_{30} = 0.0 - 8.0 \times 10^{-12}$
$O(^1D) + N_2 \xrightarrow{k_{31}} O + N_2$	$k_{31} = 2.0 \times 10^{-11} \exp[1118 / T_n]$
$O(^1D) + O_2 \xrightarrow{k_{32}} O + O_2$	$k_{32} = 2.9 \times 10^{-11} \exp[675 / T_n]$
$O(^1D) + e \xrightarrow{k_{33}} O + e$	$k_{33} = 2.9 \times 10^{-10} (T_e / 300)^{0.91}$

Table 8. Radiative quenching.

$N(^2D) \xrightarrow{a_1} N + h\nu(5200\text{\AA})$	$a_1 = 1.07 \times 10^{-5} / s$
$N(^2P) \xrightarrow{a_2} N + h\nu(3455\text{\AA})$	$a_2 = 5.4 \times 10^{-3} / s$
$N(^2P) \xrightarrow{a_3} N(^2D) + h\nu(10400\text{\AA})$	$a_3 = 7.9 \times 10^{-2} / s$
$O(^1D) \xrightarrow{a_4} O + h\nu(6300\text{\AA}, 6364\text{\AA})$	$a_4 = 6.8 - 9.4 \times 10^{-3} / s$
$O(^1S) \xrightarrow{a_5} O + h\nu(2972\text{\AA})$	$a_5 = 4.5 \times 10^{-2} / s$
$O(^1S) \xrightarrow{a_6} O(^1D) + h\nu(5577\text{\AA})$	$a_6 = 1.06 / s$

The background neutral atmosphere is determined by MSIS90 [Hedin, 1991], which provides the altitude profiles of N, O, N₂, NO, O₂. Table 6 lists the geo-solar conditions of the Red Air I experiment. The electron density was obtained from Millstone Hill radar measurements (M. Mendillo, private communication). The main ion species NO⁺, O⁺, O₂⁺ are determined through steady state assumptions that lead to relationships similar to that in Link and Cogger [1988]. Finally, minor species and metastable species N(²D), O(¹D) and O(¹S), and N⁺ are determined from the neutral and ion species mentioned above, again using steady state assumptions.

The observed background 6300Å airglow for the Red Air I experiment was determined from unperturbed portions of the all sky camera images. The measured background airglow was near 90 Rayleighs for a zenith look. This is equivalent to 108 Rayleighs with an atmospheric extinction correction of 1.2 [Baumgardner, personal communication, 1991].

The model determination of integrated 6300Å airglow intensities were generally much higher than the measured intensities. The airglow chemistry of SA and LC predicted airglow intensities that were approximately two times the observed intensities. There are several parameters of the model that can, if altered, reduce the modeled airglow, e.g., error in chemical rates, exospheric temperature, error in input into MSIS90, error in the measured electron density profile, etc. The lower atmospheric temperature of 1030K was used for determining the atmosphere density profiles and reaction rates. This alone reduced the predicted airglow by 50%. To match the measured airglow value, the rate of the reaction



was assumed to be lower than the rate given by *Albritton et al.* [1977]. The experimental conditions of *Albritton et al.* [1977] de-coupled the kinetic motion energy of the reactants from the O_2^+ vibrational energy. *Chen et al.* [1978] measured the rate of reaction (7.10) with true thermal distributions for the reactants and O_2^+ internal energy. This resulted in lower reaction rates than *Albritton et al.* [1977]. Unfortunately, the *Chen et al.* [1978] measurements were from 300K to 900K. The observed airglow can be reproduced in the model with no alterations of other rate coefficients given in the SA chemistry set when the formula suggested by *Chen et al.* [1978] for reaction (7.10) is used with a temperature of 1030K.

For the electron density profile and plasma temperature measured for the Red Air I experiment, the steady-state chemistry model predicts 6300Å airglow values of 110 Rayleighs and 140 Rayleighs for SA and LC, respectively, compared to the measured 6300Å airglow value of 108 Rayleighs. SA provided excellent agreement with the experimental measurement. The production rates of $\text{O}(^1D)$ are the same for both chemistry sets (Figure 18). LC assumed no quenching of $\text{O}(^1D)$ by O and the slower radiative decay for $\text{O}(^1D)$.

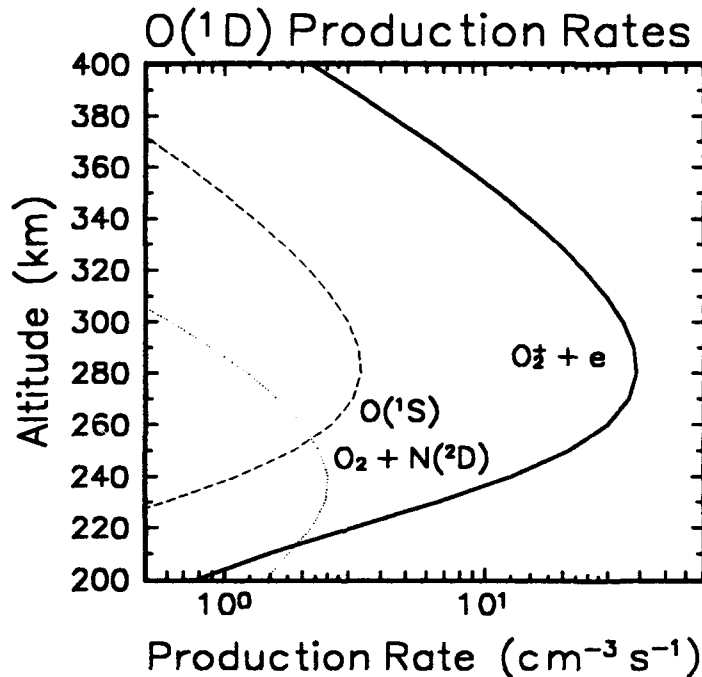


Figure 18. The production profiles of $\text{O}(^1D)$ for both LC chemistry set and SA chemistry set.

Figure 19a shows the loss rates of $O(^1D)$ for LC chemistry. A $O(^1D)$ quenching rate of $4 \times 10^{-12} \text{ cm}^{-3} \text{ s}^{-1}$ was needed to bring LC chemistry into agreement with the Red Air I background airglow measurement. The loss rates of $O(^1D)$ by various mechanisms are plotted in Figure 19b for SA chemistry. It is seen that $O(^1D)$ quenching by O has only a narrow altitude range of domination as the main loss mechanism, but it has a broad altitude range of relative importance. The first low altitude release occurs, fortuitously, precisely at the altitude of the peak O quenching of $O(^1D)$. However, degrading effects reduce the reliability of the lower release of Red Air I for quenching rate determinations. These degrading effects are examined below.

Figure 20 compares the normalized integrated airglow as measured by a zenith looking rocket instrument for SA and LC. There is a measurable difference if the observing rocket reaches an altitude of 300 km. The present ambiguity of the ground based measurements of ambient 6300Å airglow leaves no indication as to the preferred Einstein coefficient of $O(^1D)$ decay and the $O(^1D)$ quenching rate by O. However, the time-dependent emission perturbation induced by the Red Air I CO_2 releases help resolve the quenching and radiative issues of $O(^1D)$ chemistry.

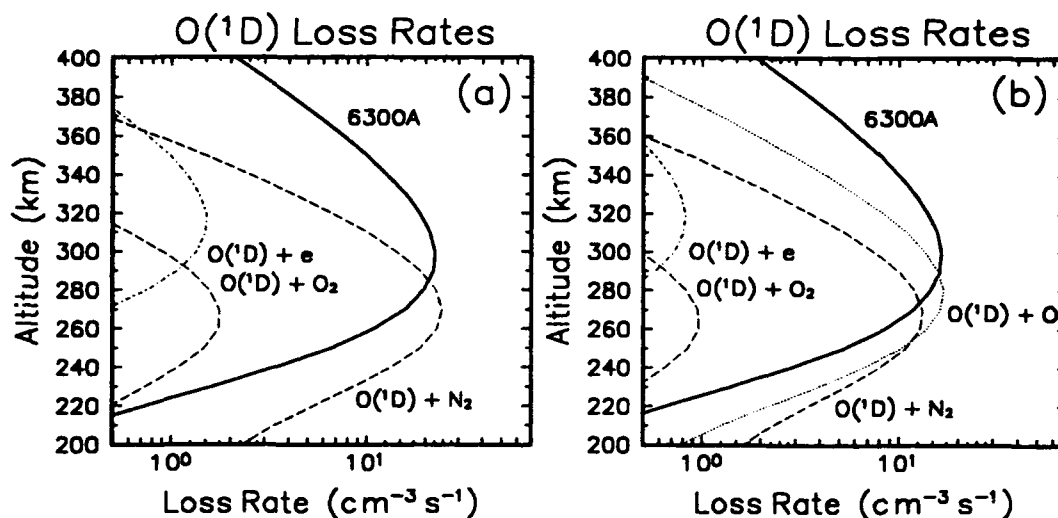


Figure 19. The loss rates of $O(^1D)$ by various mechanisms using (a) LC chemistry set and (b) SA chemistry set.

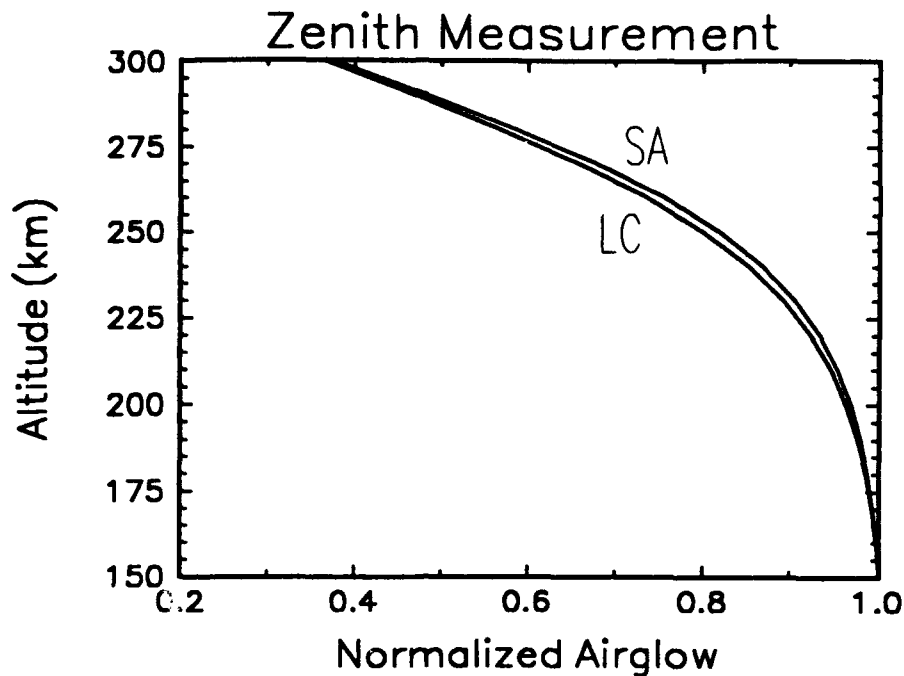


Figure 20. The normalized integrated $O(^1D)$ airglow as measured by a zenith looking rocket instrument for the LC chemistry set and the SA chemistry set.

8. TWO-DIMENSIONAL SIMULATIONS OF RED AIR I

The CO_2 releases at 253km and 379km gave 6300Å airglow enhancements that differ with each other in magnitude, rise time, and decay shape. The differences are not simply explained by the chemistry results in the above section. Modeling the Red Air I experiment requires simulation of the chemical and dynamic effects of the release and the observation methods of the airglow measurement. As will be seen, the geometry of the line-of-sight integration of the airglow played a role in the magnitude and time history of the 6300Å measurement.

The Red Air I releases of CO_2 into the mid-latitude nighttime ionosphere are modeled with a two-dimensional finite-difference model. Cylindrical geometry, with the axis of symmetry being altitude, was used to reduce the three-dimensional transport problem to a two-dimensional numerical computation. It is assumed that the magnetic field is vertical and the horizontal rocket motion is negligible. The diffusion limit is used for species transport. The ambient species for the initialization of the background within the two-dimensional model are provided by the steady-state model discussed in Section 7. CO_2 is introduced at the release altitude within the model and the chemistry and diffusion of the ambient and carbon oxide species (CO_2 , CO_2^+ , CO) are followed in time.

An average Rayleigh value is obtained from simulation data to compare with Red Air I data. The simulated airglow peak is approximately four times too large for both the SA and LC reaction set (Figure 21). This suggests that a chemical or thermodynamic process is missing or incorrectly represented in the model. In addition, the shape of the enhanced airglow curve of the simulation is a simple decay structure and not the double hump of the Red Air I data.

Figure 22 displays the simulated lower release airglow. The magnitude and the shape are not modeled well in the lower release. The two releases of the Red Air I experiment were performed

from a single rocket. This allows for the possibility of mixing the airglow signatures of the two releases spatially. This mixing is shown below to be important only for the lower release. It is interesting to note that the SA chemistry produced the brightest airglow in the upper release and the weakest response in the lower release. This is due to the peak quenching of $O(^1D)$ by O at the 253 km altitude release.

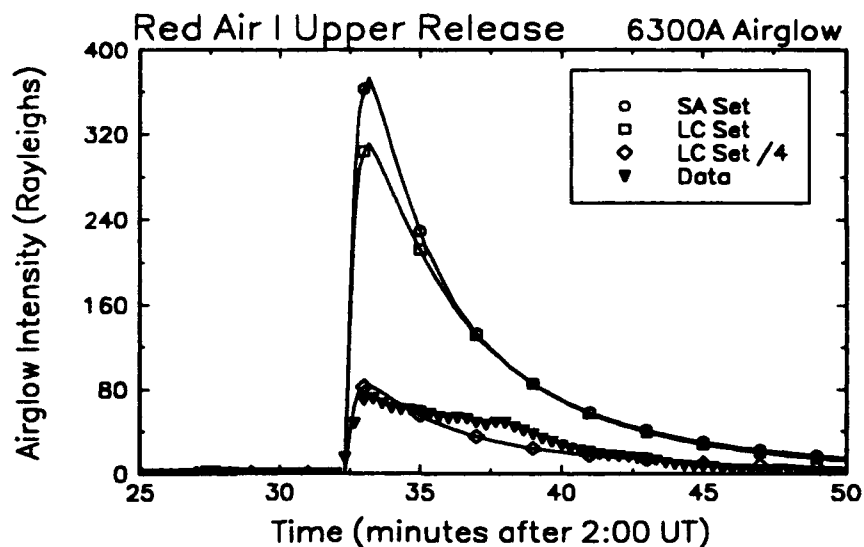


Figure 21. The modeled and measured 6300Å airglow from the center of the upper release. The modeled airglow is obtained from the SA chemistry set (circles) and the LC chemistry set (squares). The LC set airglow curve is divided by four to show the approximate match with the data (diamonds). The Red Air I data from the upper release is plotted with triangles.

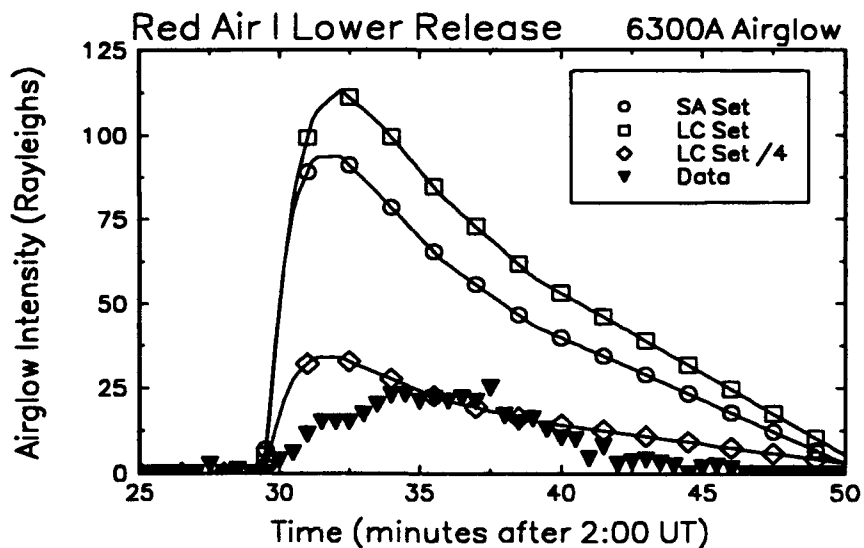


Figure 22. The modeled and measured 6300Å airglow from the center of the lower release. The modeled airglow is obtained from the SA chemistry set (circles) and the LC chemistry set (squares). The LC set airglow curve is divided by four to show the approximate match with the data (diamonds). The Red Air I data from the lower release is plotted with triangles.

To determine if the airglow perturbations of the separate releases were "mixed", the airglow histories of the two simulations are linearly added using the observational geometry of the all sky camera. The releases were separated enough to make the linear adding of the airglow effects reasonable. The CO₂ of the lower release may have expanded up to the higher altitude of the second release and vice versa. Figure 23 shows the added effects of the two releases at the airglow measurement point of the high and low altitude releases. The expansion of the lower release cloud is stopped abruptly at the lower altitude. The lower release does not affect the upper release region. The shape of the time decay of the airglow enhancement measured at the upper release point cannot be explained by the mixing of the simulations of the two releases. A separate chemical process must be at work in the upper release. This is examined in the next section.

The higher altitude release has a definite influence on the measurement of the lower release experiment. The upper release expands and falls into the region of the lower release point. The Red Air I airglow measurement has a plateau near the front of the time-airglow curve. This could be the mixing region of the upper and lower cloud effects. This is unfortunate since this is the region where O quenching of O(¹D) is important. The lower altitude intensity predictions with LC and SA chemistry are both too high by a factor that is larger than the upper release predictions. The ratio of the peak intensity of the upper to the lower releases is approximately 3.8. The LC set produces a ratio of 2.0. The SA set with O on O(¹D) quenching produces a ratio of 2.5, which is closer to the measured value. The absolute intensities are affected by freezing of CO₂ upon release. Perhaps the upper and lower releases have different release characteristics that allow different percentages of CO₂ to participate in the airglow chemistry. This would invalidate any conclusion based on the ratio of upper to lower airglow intensities, but the ratios indicate that O quenching may be present. Two remaining questions are addressed in the following section: (1) why does the model over-predict the airglow, and (2) what produces the hump in the upper release airglow signature?

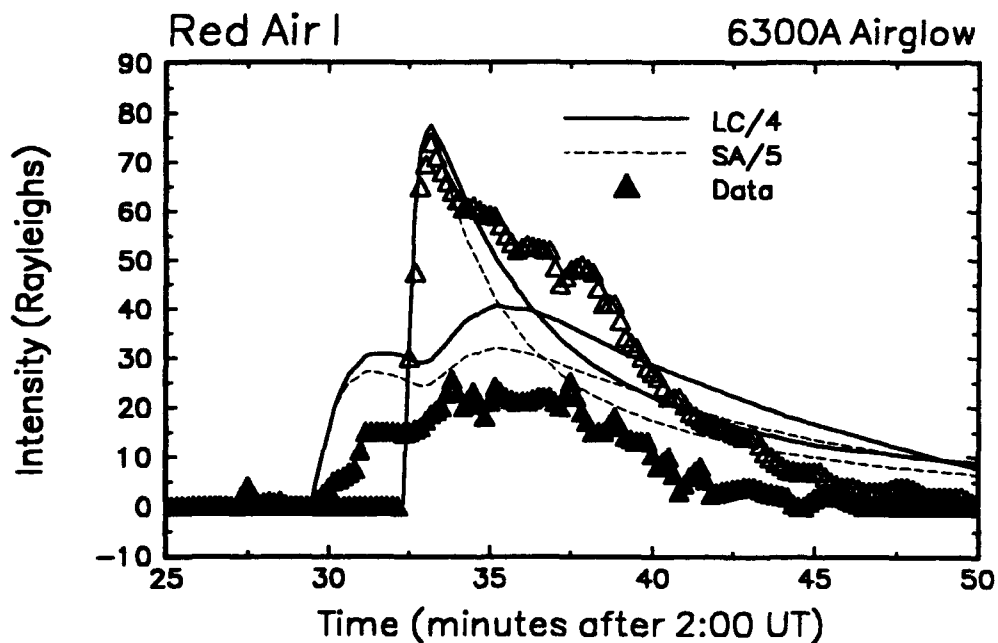


Figure 23. The measured airglow intensities for both upper (empty triangles) and lower releases (solid triangle) are compared to the predictions of the SA chemistry (dashed line) and the LC chemistry (solid line). The airglow predictions have been divided by a constant so that the upper release measured and modeled airglow intensities are the same.

9. CO₂ CHEMICAL INVESTIGATIONS

Computations were performed using a single-cell Lagrangian chemical-kinetics code to investigate the possible differences in the chemistry sets of standard CO₂ reactions, explicit vibrational CO₂-O₂⁺ reactions, clustering CO₂ reactions, and the freezing and subsequent sublimation of CO₂ reactions. The removal of CO₂ by diffusion is also included in the model.

The focus of this investigation was to determine chemical processes that may produce the hump observed in the high altitude release 6300Å emission profile. It should be noted that without spatial and dynamic modeling, it is difficult to obtain absolute comparisons with airglow measurements.

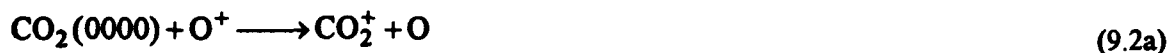
The initialization of model parameters was based upon the actual release conditions. Each release consisted of 9 kg (1.24×10^{26} molecules) of CO₂. Based on data from the all sky camera, the release at high altitude is assumed to have quickly expanded to a cloud having a radius of 25 km. At this size, assuming homogeneity, the cloud CO₂ density was estimated to be 10⁶ molecules per cubic centimeter. The rate that CO₂ left the system via diffusion in the model was estimated to be 10⁻¹ cm³ s⁻¹.

9.1 Standard CO₂ Chemistry

In the first attempt to model the release, the standard CO₂ reaction set outlined in Section 5 was used. Figures 24 *a* and *b* represent the time histories of CO₂ and O(¹D) density. From the density of O(¹D) a rough estimate of the peak enhancement over the background can be made. Assuming a 50 km region of relatively dense CO₂, the peak enhancement from this model was estimated to be 148 Rayleighs. This is twice the observed peak. From the O(¹D) profile shape it is clear that this simple model does not produce the hump in the observed emissions. It was determined that the standard chemistry dissipates CO₂ too rapidly to create the hump. This suggests that there are other, previously unsuspected processes that affect the CO₂ chemistry.

9.2 Explicit Vibrational CO₂ Chemistry

The inclusion of explicit vibrational chemistry was an attempt to model the effect of heating CO₂ vibrational levels on its decay. Introduction of explicit vibrational states of CO₂ (A. A. Viggiano, private communication) and O₂⁺ [Guberman, 1988; Queffelec et al., 1989] into the chemistry is examined to allow for non-local thermal equilibrium effects on the simulated 6300Å airglow. Reactions (1.1) and (1.2) become



The rates of reactions (5.1a,b) and (5.2a,b) are given as a function of vibrational states of CO₂ using unpublished data of A.A. Viggiano (private communication). There has been no attempt to extrapolate the data up to the high ionospheric temperatures, thus, data for T_{CO₂} = 500K is used. Rates for vibrational quenching and excitation of CO₂ are taken from Archer [1990].

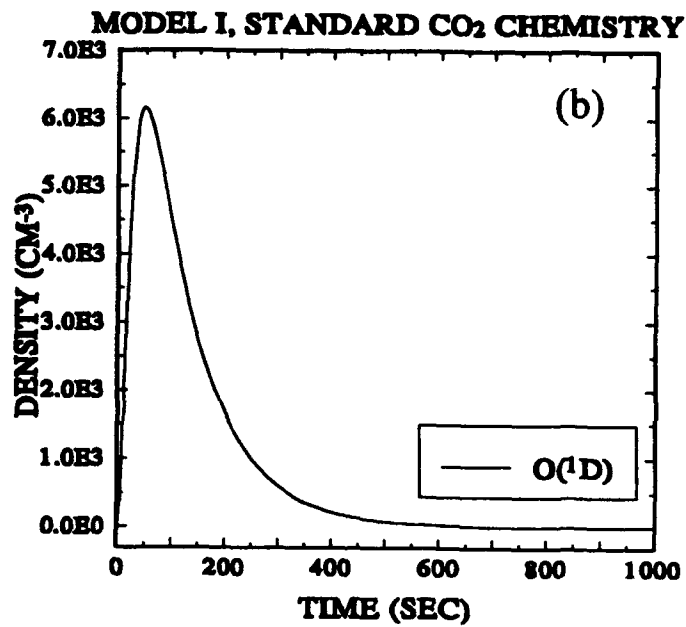
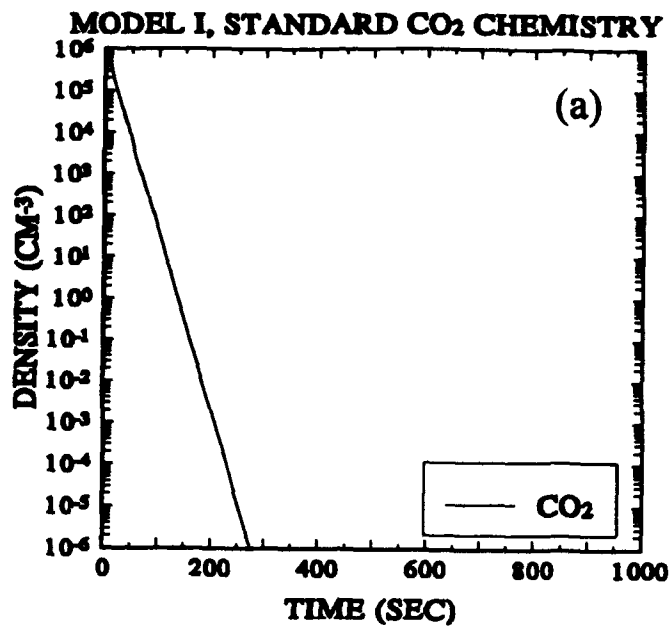


Figure 24. (a) CO₂ density time history for high altitude release, standard chemistry set. (b) O(¹D) density time history for high altitude release, standard chemistry set.

Branching of the $\text{CO}_2\text{-O}^+$ reaction path varies with vibrational level. Ground state CO_2 producing O_2^+ (9.1a) has a branching ratio of 0.96, leaving reaction path (9.2a) relatively unimportant to the system. $\text{CO}_2(0110)$ producing O_2^+ (9.1b), however, controls only 87% of the reactions, making the production of CO_2^+ (9.2b) important though still small. In addition to these changes, all low energy reactions ($E < 0.1\text{eV}$) involving CO_2 were updated to include these explicit levels. The reactions were taken from *Archer (1990)*.

The production rates of vibrational states of O_2^+ are taken from *Viggiano et al. [1990a]*. These rates are based on data taken in the temperature range of 88K to 300K. This is a limitation on the NLTE investigation but the results will indicate trends. Quenching rates of $\text{O}_2^+(m)$ are estimated. Further laboratory studies are necessary to provide proper rates for the chemical models.

Figures 25 a and b represent the time histories of important species during the model simulation. It is clearly seen that $\text{O}(^1D)$ production is not changed in any significant way from the standard CO_2 model results. The decay shape and time constant are virtually identical to that previous result. The plot of CO_2 density shows its decay is also unaffected. The peak enhancement over the background is estimated to be slightly more than a factor of two too great and the characteristic hump has not been created. This implies that the non-equilibrium effects of vibrational excitation of CO_2 are not responsible for the secondary peak of $\text{O}(^1D)$ production that produces the observed emissions hump.

Computations using the two different chemistry sets of CO_2 (with and without vibrational states) give the same results. There is presently no advantage to using explicit vibrational levels of CO_2 and O_2^+ in the chemistry. This does not say that vibrational level chemistry is not important in the modeling of the NLTE conditions in CO_2 releases. A possible explanation is that the rates for reactions containing CO_2 and O_2^+ were obtained from low temperature measurements ($T < 545\text{K}$ and 300K , respectively). Laboratory experiments with higher temperature environments could give reaction rates that would alter results of subsequent simulations.

The results indicate that too much 6300\AA airglow is predicted by the best simulation effort. Possible reasons for the low $\text{O}(^1D)$ production in the Red Air I release are: 1) CO_2 freezing or clustering at release, 2) error in the MSIS86 neutral atmosphere, 3) error in the measured electron density, 4) slower charge interchange rate of CO_2 with O^+ .

9.3 CO_2 Cluster Chemistry

The chemistry kinetics code was used to investigate the impact of CO_2 clustering (or freezing) and subsequent evaporation (or sublimation) on the induced 6300\AA airglow produced by a release of CO_2 in the ionosphere. Two experimental observations in the Red Air I airglow measurements suggest that clustering or freezing plays a role in the CO_2 release chemistry. First, the observed 6300\AA emissions are several times less than predicted emissions. The reduction of modeled 6300\AA airglow magnitude can be achieved if CO_2 freezes or clusters. Simple ideal gas calculations predict that 7% of the CO_2 would freeze in an ionospheric release and be lost to the experiment [*Bernhardt, 1987*]. Because of a large dipole moment, the CO_2 molecule is far from ideal. Van der Waals forces should be taken into account in the freezing calculation including Joule-Thompson cooling and kinetic energy loss to directed translational acceleration. Thermodynamics calculations suggest that more than 50% of the total CO_2 release may cluster or freeze. The proposed production of clusters was corroborated unanimously by several clustering experts. Indeed, large clusters ($n > 100$) were likely (*Olaf Echt, University of New Hampshire, personal communication*). This would reduce the amount of free CO_2 .

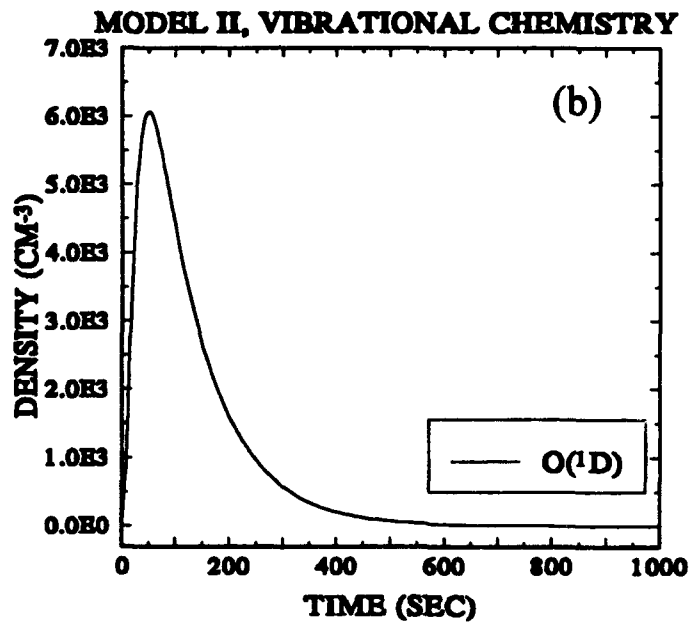
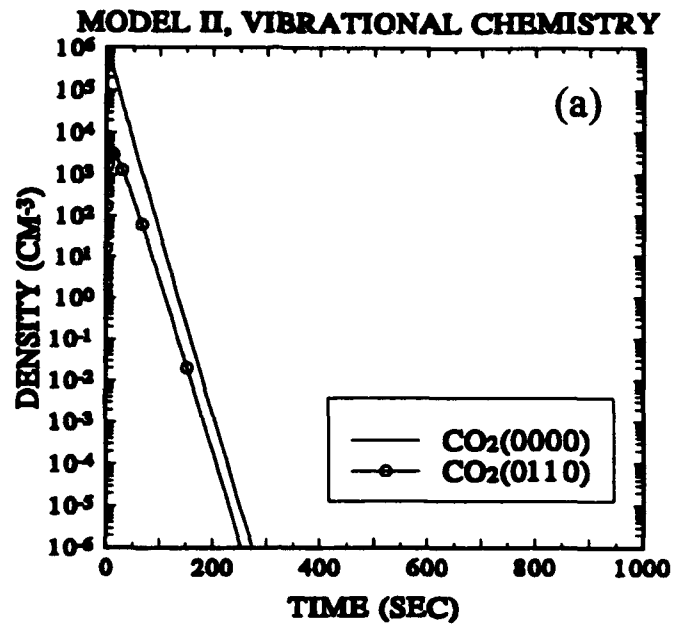


Figure 25. (a) Time history of CO₂ vibrational level density for high altitude release, explicit CO₂ vibrational state chemistry set. (b) O(¹D) density time history for high altitude release, explicit CO₂ vibrational state chemistry set.

The second reason for considering freezing and clustering is the presence of a hump in the decay of the 6300Å airglow signature. The hump might imply the slow release of free CO₂ from the frozen or clustered CO₂.

It is unclear how the clusters actually decay in collision, requiring that two cases be investigated. The first case assumes that after sufficient energy has been imparted to the cluster via collisions, a single CO₂ molecule breaks off from the larger group. The second case models the ejection of a smaller cluster from a larger heated group.

For both of the models it is assumed that cluster breakup occurs only due to collisions with relatively populous atomic oxygen and diatomic nitrogen. An estimate of the reaction rates for these processes is made by taking into account the colliding particle cross-sections and the energy of the colliding particles. The basic equation to determine the reaction rate is then

$$v_{12} = \sigma_0 \left(\frac{8kT_1}{\pi M_1} + \frac{8kT_2}{\pi M_2} \right)^{\frac{1}{2}} \quad (9.3)$$

where σ_0 is the collision cross section, k is Boltzmann's constant, T is temperature, and M is the particle mass. The subscript "1" refers to values for the CO₂ clusters and "2" represents values for either O or N₂. For this calculation, the temperature of the cold CO₂ is assumed to be 250K and the hotter ambient species are 1030K. The masses of the individual particles are 7.304×10^{-26} kg for CO₂, 4.648×10^{-26} kg for N₂, and 2.656×10^{-27} kg for O. The collision cross section is assumed to be circular and is determined by

$$\sigma_0 = \pi (r_1 + r_2)^2 \quad (9.4)$$

where r is the particle radius. The radius of CO₂ is 2.25Å, the radius of N₂ is 1.9Å, and the radius of O is 1.3Å. The effective radius of the CO₂ clusters, r_1 , varies with cluster size, n , in the following manner

$$r_1 = n^{\frac{1}{3}} r_{\text{CO}_2} \quad (9.5)$$

where r_{CO_2} is the effective radius of a single carbon dioxide molecule.

It is assumed that a particle colliding with a CO₂ cluster transfers energy only to a single CO₂ molecule in that cluster, and this energy is then transferred to the rest of the cluster via weak cluster bonds. When enough energy is absorbed into the cluster then a particle will "boil" off. This energy transfer collision frequency is

$$v_{ene} = \left(\frac{M_2}{M_1 + M_2} \right)^2 v_{1,2} \quad (9.6)$$

where the mass is no longer the cluster mass but the mass of one CO₂ molecule. The mass weighting in equation (9.6) for energy transfer collisions is 0.15 for N₂ collisions and 0.07 for O collisions.

It is also assumed that the binding energies of the clusters are small and a single collision will remove molecules from the cluster. The rates for reactions developed with this model are found in Figure 26 below as a function of cluster size up to 10.

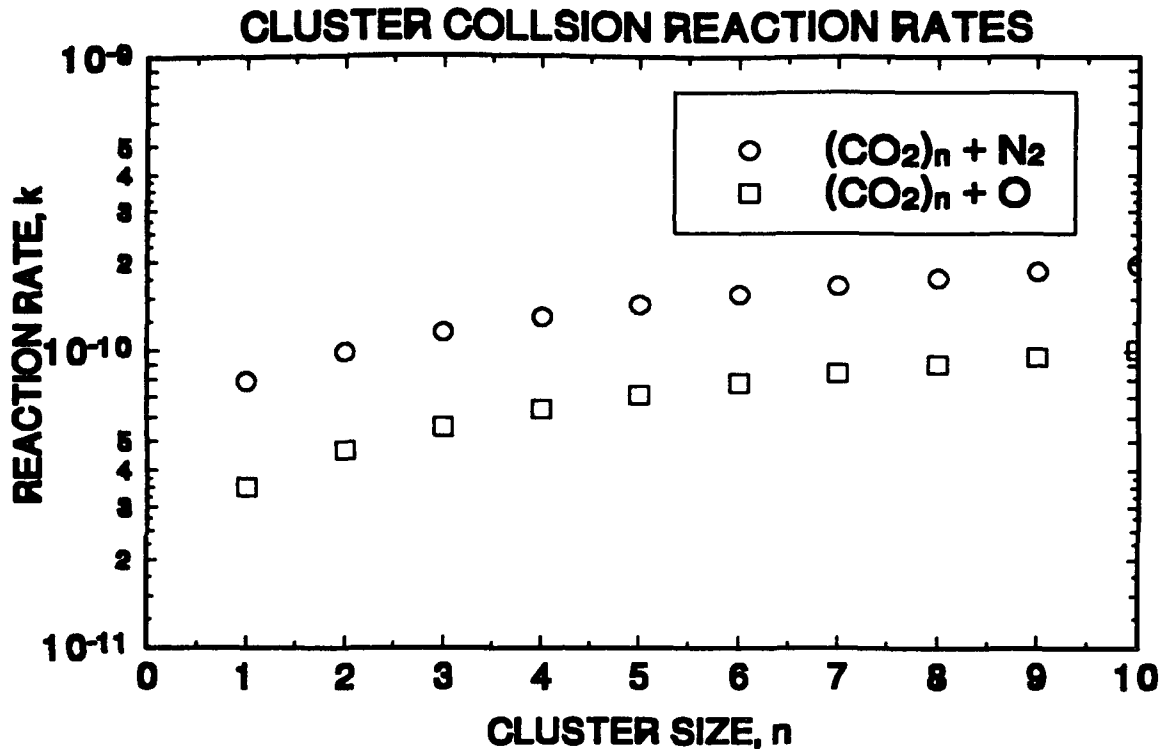
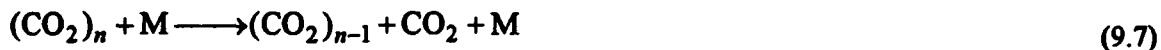


Figure 26. Estimated reaction rates for breakup of clusters due to collisional heating.

9.3.1. Single Particle Removal

The chemistry for this model is identical to the standard CO₂ reaction set with the addition of reactions describing the breakup of the CO₂ clusters by ejection of a single CO₂ molecule. These reactions are of the form



where M is either O or N₂. The rates for these reactions are determined as described above.

Figures 27 *a* and *b* display the time histories of O(¹D) and CO₂ density for this model. Fifty percent of the total CO₂ cloud density is assumed to be clustered upon release as (CO₂)₁₀ clusters. Larger cluster sizes (n=30,60,90) were also used but n=10 produced results that better reflected the 6300Å decay curve. Figure 27*a* shows that the simple breakup cascade of CO₂ clusters down to single molecules does, in fact, delay the formation and relaxation of O(¹D). From that resulting O(¹D) history a peak enhancement of 92 Rayleighs is estimated with no hump predicted. The predicted intensity is now very close to the observed 75 Rayleighs. It is clear that this model does not delay the introduction of CO₂ into the system nearly long enough to create a secondary O(¹D) density peak which would lead to the observed density curve. However, the reduced peak emissions from relaxing O(¹D) indicates that a significant percentage of the released CO₂ may be clustered, verifying a critical assumption made. If the second assumption of small cluster sizes is valid, the shape of the oxygen curve suggests that boiling off one CO₂ molecule at a time from a heated cluster is not the correct decay mechanism for the process. The supply of a significant amount of CO₂ to the system must come after the initial release and it must come fast enough to make a secondary peak in the carbon dioxide decay profile.

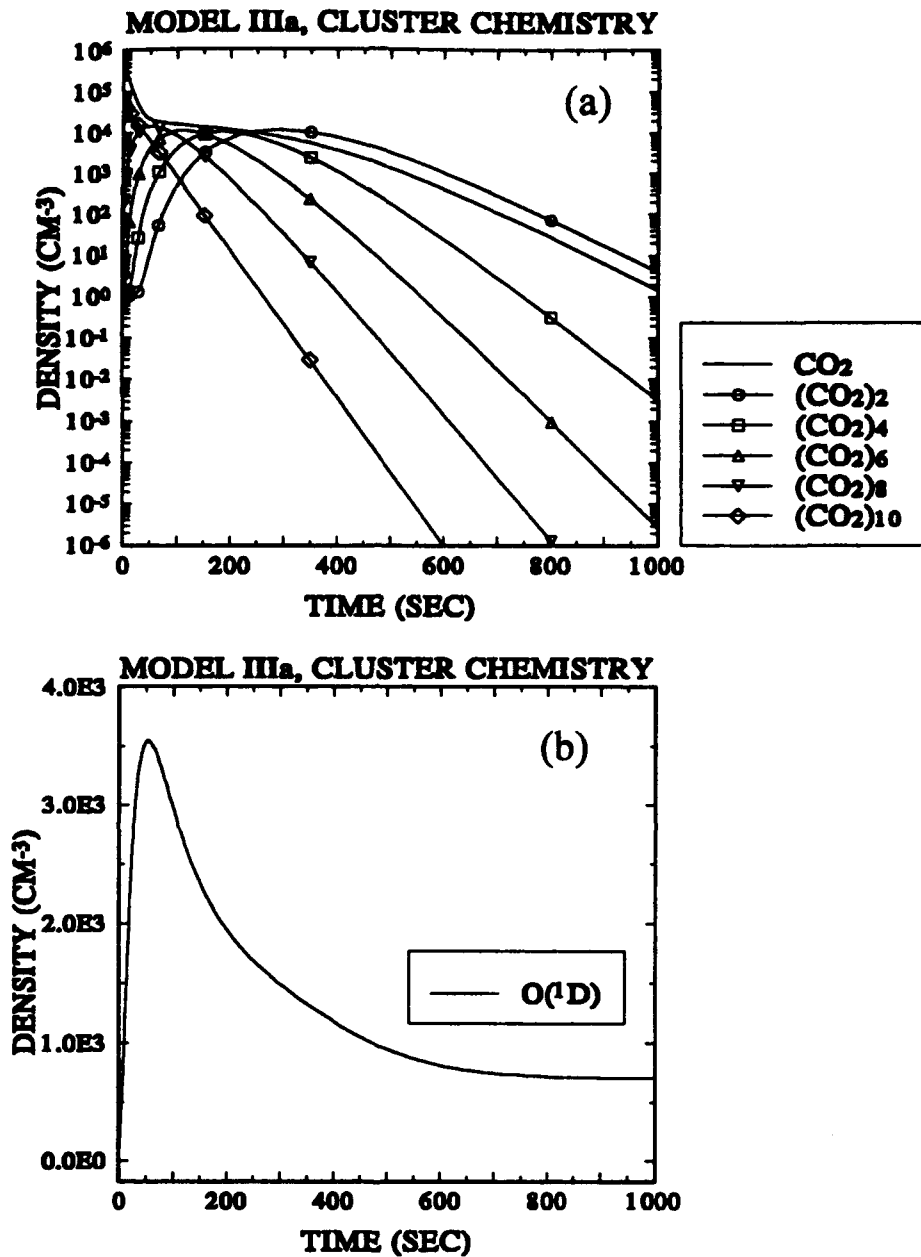


Figure 27. (a) CO_2 cluster density time history for high altitude release, single particle removal model: $(\text{CO}_2)_n + \text{M} \rightarrow (\text{CO}_2)_{n-1} + \text{CO}_2 + \text{M}$. 50% of total CO_2 released as $(\text{CO}_2)_{10}$. (b) $\text{O}(^1\text{D})$ density time history for high altitude release, single particle removal model: $(\text{CO}_2)_n + \text{M} \rightarrow (\text{CO}_2)_{n-1} + \text{CO}_2 + \text{M}$ 50% of total CO_2 released as $(\text{CO}_2)_{10}$

9.3.2. Small Cluster Removal

In an attempt to more accurately model the decay of CO₂ clusters, reactions of the following form were added to the standard CO₂ reaction set



where M again represents O or N₂. These reactions have the same reaction rates as their counterparts in the single particle removal model. CO₂ is then released via



Again it was assumed that small clusters of (CO₂)₁₀ were populated with 50% of the total release cloud density. The solution of the model is shown in Figure 28 where the density time histories of the important species CO₂ and O(¹D) are presented. Examination of Figure 28a shows that a secondary peak in CO₂ density is achieved due to the breakup of large clusters into smaller ones. This process quickly populates (CO₂)₂ clusters to a peak at about 100 seconds which then leads to the fast introduction of single carbon dioxide molecules into the already relaxing chemical system. This creates the secondary peak in CO₂ density and, therefore, in O(¹D) as well. Figure 28b clearly shows the formation of a hump in the oxygen decay curve. In addition, the maximum density of oxygen is reduced from the previous models' results and allows an estimate of peak 6300Å enhancement to be 78 Rayleighs, only about 5 percent above the observed maximum. On the basis of these results, this cluster model is a feasible description of the chemical processes that led to the unexpected hump and peak emission observed in the Red Air I high altitude 6300Å enhancement profile.

9.4. Sublimation of Frozen CO₂

The Red Air I release conditions could have frozen a large amount of the CO₂ during the release of the gas instead of clustering it. This suspicion arises from the fact that during the rocket flight the CO₂ canister was held at a temperature just above the critical temperature. Joule-Thompson cooling and directed acceleration effects from the fast discharge of high pressure gas leads one to speculate that as the gas was leaving the canister it froze, seeding the release area with small chunks of frozen CO₂. The subsequent sublimation of the ice could prolong the introduction of CO₂ into the system and thus O(¹D) production. This effect was modeled by assuming that the frozen CO₂ particles were small and would sublime at a constant rate over 300 seconds. Freezing and sublimation of 50% of the CO₂ is modeled by including a CO₂(frozen) species and a sublimation reaction:



Figures 29 a and b show the results of this effort. The CO₂ density time history shows a delay in the decay of that species while the sublimation process continues. The resulting O(¹D) profile exhibits a clearly defined hump shortly after the sublimation is complete. The peak enhancement over the background from this model is estimated to be 150 Rayleighs, about a factor of two too high. This can be attributed to not knowing the proper way to model the sublimation of frozen release particles. The peak enhancement of the emissions is directly related to the peak of CO₂ density. These results show freezing-sublimation of CO₂ can explain the observed emissions.

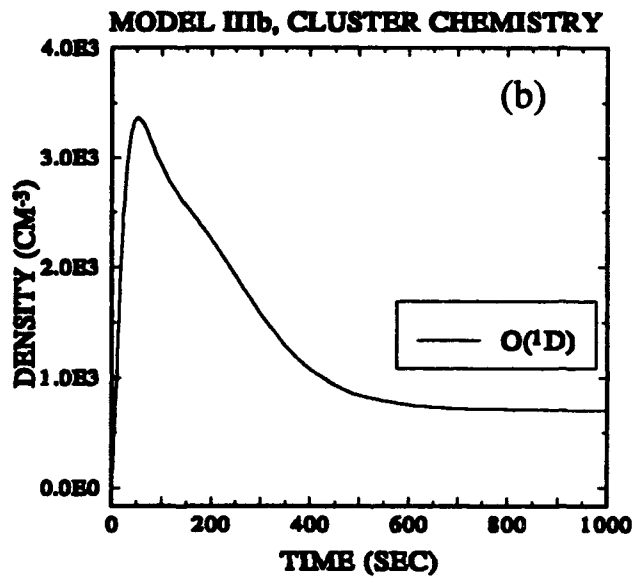
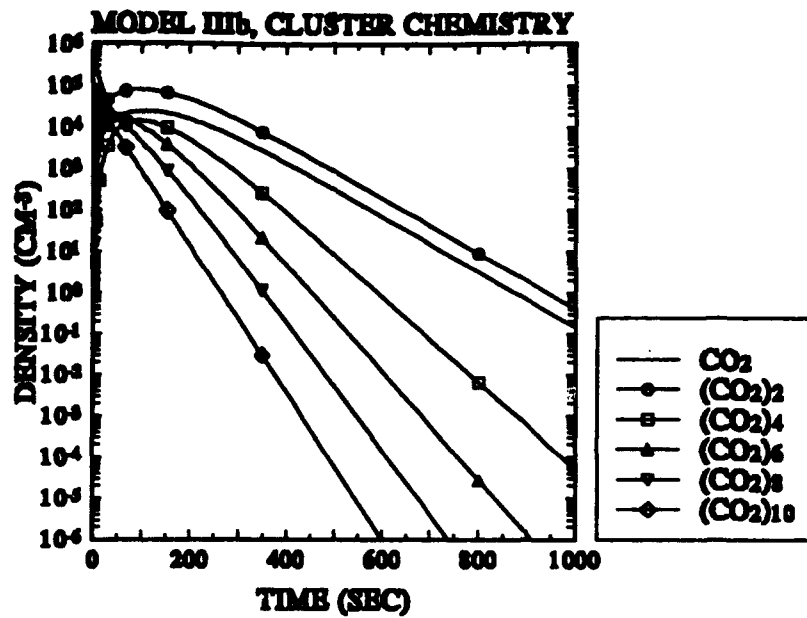


Figure 28. (a) CO₂ cluster density time history for high altitude release, small cluster removal model: $(\text{CO}_2)_n + \text{M} \rightarrow (\text{CO}_2)_{n-2} + (\text{CO}_2)_2 + \text{M}$. 50% of total CO₂ released as (CO₂)₁₀. (b) O(¹D) density time history for high altitude release, small cluster removal model: $(\text{CO}_2)_n + \text{M} \rightarrow (\text{CO}_2)_{n-2} + (\text{CO}_2)_2 + \text{M}$. 50% of total CO₂ released as (CO₂)₁₀.

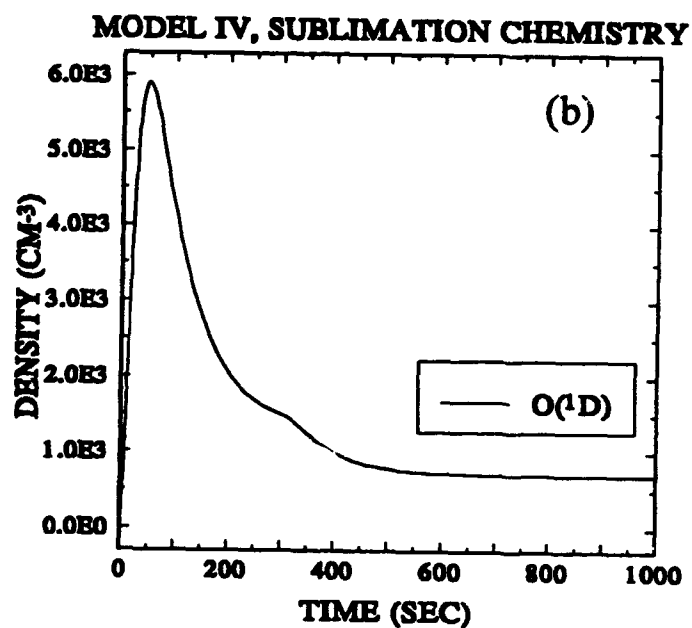
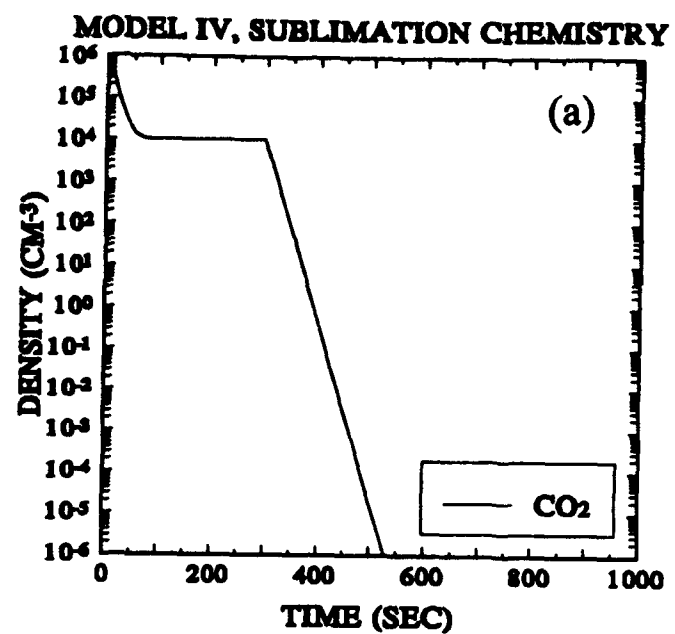


Figure 29. (a) CO₂ density time history for high altitude release, sublimation model. (b) O(¹D) density time history for high altitude release, sublimation model.

10. DISCUSSION OF CO₂ RELEASES

CO₂-ionospheric chemistry has been examined through comparison of field measurement and simulation results of the Red Air I CO₂ releases. Simulations that use standard CO₂-ionospheric reactions predict more 6300Å airglow than was observed. The simulated airglow is too large by a factor of four for the upper release and a factor of five for the lower release. The upper release may have suffered more removal of CO₂ by freezing or clustering due to the less dense ambient gases. The discrepancy may be due to error in the published charge exchange rate of O⁺ with CO₂. The conditions were approximately thermal in the experiment with CO₂ heating to 1000K. Due to the lack of laboratory measurements at higher temperatures, the CO₂ vibrational-state chemistry used in this study may not represent CO₂-ionospheric chemistry well. The discrepancy between simulation and experiment also could be due to misrepresentation of the actual ambient conditions. Increase of the electron density at the upper release affects the 6300Å airglow enhancement proportionally.

Not only do the observed and predicted airglow magnitudes differ, but also the shapes of the airglow intensity versus time curves differ. The 6300Å airglow observed at the position of the lower release is well modeled by adding the modeled airglow from upper and lower release. Two rockets for the Red Air II releases were used to separate the clouds and avoid the airglow overlap.

The intensity-time curve of the 6300Å emission from the upper release also has a complex shape. Modeling indicates that the lower release did not expand up to the upper release. The complex intensity-time curve appears to be caused by other physical processes. Chemical and thermodynamic mechanisms were examined as explanations for the bimodal airglow intensity curve. Explicit vibration chemistry was included but it was determined that NLTE effects could not produce the observed "hump" in the 6300Å signature. It was shown that perhaps the freezing-sublimation or clustering-evaporation of CO₂ could produce the second hump of the airglow curve in the upper release. A simulation with CO₂ clustering and evaporation produced the best 6300Å intensity-time curve shape. Significant clustering of the CO₂ probably occurred in the Red Air I release.

The freezing or clustering of CO₂ in future releases may be alleviated by heating the dispenser hotter than the CO₂ critical temperature of 304K prior to release to overcome the significant Joule-Thompson cooling. Also, baffling the release chamber will reduce thermal cooling due to directed acceleration of the gas.

Examination of the ambient airglow signatures predicted with two sets of airglow chemistry (*Solomon and Abreu* [1988] and *Link and Cogger* [1989]) suggests that atomic oxygen quenching of O(¹D) could be important. Additionally, the best match of the upper and lower release airglow intensity ratio was obtained using a non-zero quenching rate (at least $4 \times 10^{-12} \text{ cm}^3 \text{ s}^{-1}$).

Because the processes in the release clouds included release cloud mixing and freezing or clustering, definitive assessments of CO₂ and O(¹D) chemistry could not be made. Red Air II may be more definitive in answering these questions.

11. HF HEATER INDUCED CHEMISTRY IN THE UPPER ATMOSPHERE

The chemical effects within an HF (high-frequency) radar beam were studied through modeling of the energy deposition-emission processes and detailed induced chemistry. This effort was done in support of assessing the environmental impact of the HF Active Auroral Research Program Ionospheric Research Instrument (HAARP IRI) HF facility. The HAARP radar will be used to heat the ionosphere to examine instabilities and other ionospheric processes. Ionospheric heating experiments have been used primarily to study plasma dynamics and instabilities [e.g., *Carlson and Duncan*, 1977; *Dubois et al.*, 1990]. The published literature of chemical effects

within HF heater beams focused primarily on F region airglow production [Megill et al., 1970; Sipler et al., 1974; Bernhardt et al., 1989; and references therein]. Others have examined energy balance and electron temperatures within HF beams [Farley, 1963; Thomson, 1970; Meltz and LeLevier, 1970; Meltz et al., 1974; Mantas et al., 1981; Bernhardt and Duncan, 1987; Barr and Stubbe, 1991; Stocker et al., 1992]. Most of the studies cited have examined F region energy depositions.

The set of chemical reactions used in our study of the ionospheric heating experiments is adequate for E and D region models. This will allow us to examine the magnitude of the HF beam modification of the natural chemical system in regions of the upper atmosphere. In particular, energy enhanced chemistry can produce HO_x and NO_x species, which may subsequently be transported to lower altitudes. These species can adversely participate in the ozone chemistry of the stratosphere and mesosphere.

An initial precursory effort to model the HF heating modification was performed to discover the possibility of a null effect on NO_x and HO_x densities. These results will provide the foundation to determine the best avenue for developing higher-order models of the modification.

Recent attention has been given to the effect of the energetic particle events on ozone layer concentration [Jackman et al., 1980; Rusch et al., 1981; Orsini and Frederick, 1982; Frederick and Orsini, 1982; Solomon et al., 1982; Callis et al., 1991]. The energetic particles ionize air molecules. The ionization and recombination chemistry produces odd nitrogen species. Important odd nitrogen species are N, NO, NO₂, NO₃, HNO₃, HNO₄. It was determined by Crutzen [1970] and Johnston [1971] that odd nitrogen plays a role in determining ozone (O₃) densities within the stratosphere and mesosphere. The amount of ozone present in the stratosphere is a result of a balance between processes that produce ozone and processes that destroy ozone.

12. ODD NITROGEN-OZONE CHEMISTRY

The ozone destruction ability of CFCs (Chlorofluorocarbons) has been well publicized. Ozone is primarily created through the three-body association reaction:



Atomic oxygen is created through photodissociation of O₂ by solar EUV in the upper atmosphere. Two important reactions in odd nitrogen-ozone chemistry are



Reactions (12.2) and (12.3) have a combined net result of:



The loss of atomic oxygen reduces the rate of O₃ production via reaction (12.1). The odd nitrogen molecules are not destroyed in the reactions (12.2) and (12.3). NO and NO₂ can participate in O₃ and O destruction repeatedly. This is the nature of a catalytic reaction. The above chemistry is a simplification of NO_x chemistry but demonstrates the main effect of increased odd nitrogen levels in the stratospheric ozone layer.

The largest source of odd nitrogen in the upper atmosphere is the reaction



This source of NO produces roughly 4.5×10^{34} NO molecules per year in the stratosphere and mesosphere.

High-energy particle events are also important sources of odd nitrogen molecules. Energetic particles generated in solar flares produce "particle events" in the upper atmosphere. The fast protons in solar proton events (SPE) strike the atmosphere and produce electron-ion pairs. For every 35 eV of energy deposited in the atmosphere one electron-ion pair is produced. Other energetic particle events, such as relativistic electron precipitation (REP), and galactic cosmic rays (GCR), ionize air with the same efficiency. Impact ionization reactions are primarily



Ionization of air by electron or proton impact eventually produces odd nitrogen species through recombination of an ion-electron pair

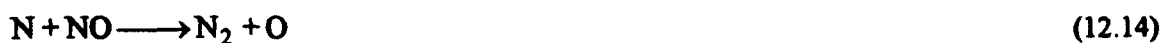


and NO production through



Careful accounting of odd nitrogen production suggests that 1.3 to 1.6 odd nitrogen molecules are produced per ionization [Rusch *et al.*, 1981]. The number used most often in the literature is about 1.3. Additional sources of odd nitrogen are ionization of air by meteors and photochemical production in the thermosphere. The long-lived NO and N(⁴S) created in the thermosphere are subject to vertical transport. The odd nitrogen produced above 100 km altitude is transported downward to mesospheric (50-80 km) and possibly stratospheric (15-50 km) altitudes [Solomon *et al.*, 1982]. Odd nitrogen molecules, which are created above 100 km and survive the transport to the lower mesosphere and stratosphere, can participate in ozone destruction.

The only loss mechanism for NO and N during the downward transport to the stratosphere is the photodissociation of NO, coupled with a cannibalistic reaction of NO and N



The photodissociation is needed to maintain N densities because N also reacts with O₂ to produce NO (reaction (12.12)).

During the long, dark polar winters the loss rate of odd nitrogen is very small. The probability that NO reaches the stratosphere increases. Also, the vertical motion is generally downward in the upper atmosphere through the winter season. *Solomon et al.* [1982] examined high latitude odd nitrogen production and transport. They concluded that auroral activity during winter months can affect stratospheric odd nitrogen levels. They also conclude that summer hemisphere odd nitrogen densities in the stratosphere are not appreciably enhanced by auroral activity, because the N and NO densities are brought into equilibrium through photodissociation and subsequent mutual destruction during downward transport. These conclusions are supported by reports of enhanced NO densities in the winter polar region [*Rusch and Barth*, 1975].

A comparison of natural odd nitrogen sources with the nuclear test series odd nitrogen production provides necessary context in understanding the magnitude of possible perturbations caused by human activity. *Jackman and others* [1980] compile a list of the annual production of odd nitrogen from various sources. Tables 9 and 10 contain the results of the compilation. The nuclear tests produced nearly as much odd nitrogen as the largest natural source. The tests were probably responsible for a 5% reduction of global ozone layer content.

Table 9. Stratospheric NO sources [*Jackman et al.*, 1980].

Source	NO molecules/yr solar maximum	NO molecules/yr solar minimum
N ₂ O+O(¹ D)	4.5x10 ³⁴	4.5x10 ³⁴
REPs	2.7x10 ³¹	2.7x10 ³⁰
SPEs	2.5x10 ³³	2.5x10 ³³
GCRs	2.7x10 ³³	3.7x10 ³³
Nuclear testing 1961-62	2.2x10 ³⁴	2.2x10 ³⁴
Total without Nuclear tests	5.0x10 ³⁴	5.0x10 ³⁴

Table 10. Mesospheric and thermospheric NO sources [*Jackman et al.*, 1980].

Source	NO molecules/yr solar maximum	NO molecules/yr solar minimum
N ₂ O+O(¹ D)	5.3x10 ³²	5.3x10 ³²
REPs	1.4x10 ³⁴	1.4x10 ³³
SPEs	3.9x10 ³³	3.9x10 ³³
Thermospheric	1.5x10 ³⁴	3.7x10 ³³
Meteors	6.3x10 ³²	6.2x10 ³²
Total	3.4x10 ³⁴	1.0x10 ³⁴

13. ENERGY DEPOSITION MODEL

There are two known mechanisms for the conversion of HF field energy to particle energy: ohmic and anomalous. In an underdense ionosphere (that is, the HF emission frequency is much less than the plasma frequency) the absorption of the HF beam takes place through ohmic heating. Beam energy is absorbed as accelerating electrons collide with ions and neutral constituents. The directed energy of the accelerating electrons is thermalized in the collisions with neutrals and ion as well as self-collisions. On a much slower time scale, the ions and neutrals are heated through elastic and inelastic collisions with the electrons. Additionally, anomalous heating occurs when the plasma frequency approaches the HF emission frequency. Anomalous heating results from time-varying plasma instabilities and occurs in a very narrow altitude range.

Typical HF radar specifications are listed in Table 11. Ambient backgrounds for winter nighttime are used for the investigations.

Table 11. Typical HF radar specifications.

Total Beam Power	3MW (2×10^{25} eV/s)
Beam width	10^0 to 3^0
Effective Beam Power	0.7 to 3GW
Frequency Range	10 to 3 MHz
Yearly operation	320 hrs (1.15×10^6 s)
Yearly emission	3.5×10^{12} W/year (2×10^{31} eV/year)

Ambient conditions for the modeling of HF effects were obtained from MSIS90 neutral atmosphere [Hedin, 1990], the E region model of Rasmussen *et al.* [1989]. Electron profiles of Ogawa and Shimazaki [1975] are used below 90 km. The geophysical parameters of average solar activity and moderate magnetic storm activity are used in obtaining the neutral atmospheric and ionospheric profiles.

Ohmic heating of the electron gas is the assumed heating mechanism for energy deposition in the D and E region of the ionosphere. The literature has many examples of deposition calculations [Farley, 1963; Thomson, 1970; Meltz and LeLevier, 1970; Showen and Behnke, 1978; Perkins and Roble, 1979; Mantas *et al.*, 1981]. The approach of Perkins and Roble [1979] is followed and extended for the calculations presented here. For the polar ionosphere the electron energy equation can be expressed as

$$\frac{d}{dt} \left(\frac{3}{2} n_e K T_e \right) - \frac{d}{dz} \left(\lambda_e \frac{dT_e}{dz} \right) = Q_{HF} - L_{el} - L_{inel} - L_{ion} \quad (13.1)$$

where t is time, z is altitude, n_e is electron density, K is Boltzmann's constant, T_e is electron temperature, u_e is electron velocity, λ_e is thermal conductivity, Q_{HF} is the HF energy deposition term, L_{el} represents all elastic collisional energy losses, L_{inel} represents all inelastic collisional energy losses, and L_{ion} represents all ionizing collisional energy losses. The ohmic HF heating term is:

$$Q_{HF} = \frac{F}{c} \left(\frac{v_p^2}{v_b^2 + v_e^2} \right) v_e \quad (13.2)$$

where F is the energy flux of the beam, c is velocity of light, v_p is the plasma frequency, v_b is the beam frequency, and v_e is the total electron collision frequency (that is, combined electron-neutral

collision frequency, ν_{en} , and electron-ion collision frequency, ν_{ei}). The energy flux, F , is attenuated with altitude as beam energy is absorbed. A kilometer below the altitude where ν_b approaches ν_p significant energy deposition occurs due to anomalous heating. The anomalous heating can produce non-thermal electrons with energies of 2 to 10 eV [see, *Bernhardt et al.* [1989] and references therein]. The anomalous heating within the HF beam is observed in the F region. A large percentage of the beam energy is absorbed in the D and E region where ohmic heating dominates.

The heated electron gas is cooled through the transfer of energy to the heavy particles by elastic and inelastic collisions. The elastic collisional heat loss is written

$$L_{el} = \sum_i n_e \frac{m_e}{m_i} \nu_{ei} 3K(T_e - T_i) + \sum_n n_e \frac{m_e}{m_n} \nu_{en} 3K(T_e - T_n) \quad (13.3)$$

Inelastic heating is considerably more complex. *Perkins and Roble* [1979] include excitation of rotational and vibrational modes of O_2 and N_2 , fine structure levels of O, and the metastable species $O(^1D)$. The vibrational and rotational energy of O_2 and N_2 is quickly transferred to the efficient radiating molecules CO_2 and NO . Electronically excited molecules radiate or quench collisionally.

Perkins and Roble [1979] noted that the collisional cooling of the electron gas is not sufficient to keep the electron temperature from "running away" from the neutral temperature. The "run-away" electron temperature is capped at higher energies through inelastic collisions that have larger energy loss per collision (i.e., impact excitation of higher electronic states and impact ionization). Additional excited states are included in the inelastic loss term. An impact-ionization cooling term is also added. The vibrational and rotational loss rates of *Schunk and Nagy* [1978] are used. The excited states included in the model are listed in Table 12. The electron impact excitation cross sections were obtained from *Banks and Kockarts* [1973]. The energy loss terms for the electron gas through inelastic collisions can be written in the form

$$L_{inel} = E_{inel} k_{inel} n_e n_n \quad (13.1)$$

where E_{inel} is the energy of the excitation of the neutral species, k_{inel} is the rate of the excitation of the neutral species, and n_n is the density of the neutral species.

The electron density is can be sensitive to energy deposition rate. As the electron density changes so does the energy deposition rate. A self-consistent determination of the electron density and the energy deposition is necessary for a complete modeling effort. For example, within a low power HF beam, electron energy may not be sufficient to ionize but the elevated electron temperature will decrease the ion-electron recombination rate. This increases the E region plasma density. As the HF beam power increases and the electron energy with it, impact ionization may become important. The electron impact ionization cross sections were obtained from *Banks and Kockarts* [1973]. The loss terms for impact ionization have the form

$$L_{ion} = E_{IP} \alpha_n n_e n_n \quad (13.4)$$

where E_{IP} is the ionization potential and α_{en} is the impact ionization rate.

Table 12. Electronically excited species contained in the deposition model.

Gas	State	Energy (eV)	Lifetime (s)
N ₂	A ³ Σ _u ⁺	6.14	1.9
	B ³ Π _g	7.30	8.9x10 ⁻⁶
	C ³ Π _u	11.03	3.6x10 ⁻⁶
	a ¹ Π _g	9.10	1.5x10 ⁻⁴
	b ¹ Π _u	12.85	10 ⁻⁷
O ₂	a ¹ Δ _g	.98	3880
	b ¹ Σ _g ⁺	1.64	11.8
	A ³ Σ _u ⁺	4.5	10 ⁻⁷
	B ³ Σ _u ⁻	8.3	10 ⁻⁷
O	1D	1.96	148
	1S	4.17	.8
	3S	9.53	1.8x10 ⁹
	5S	9.15	6x10 ⁻⁴

14. RESULTS OF HF HEATING MODEL

The two electron density profiles are used in modeling the HF heating effects (Figure 30). Both profiles are from polar winter. For simplicity the initial electron temperature was set equal to the neutral temperature at all altitudes. The energy deposition model described in previous sections calculates magnitudes of energy deposition, electron temperature and cooling terms for HF heater beams.

Energy deposition, beam flux, electron temperature, and ionization rates for the two electron density profiles are shown in Figure 31. The energy deposition drops off sharply below 75 km for both cases due to the absence of electrons below this altitude. The electrons attach to molecules readily through three-body attachment. During daylight, photodetachment increases the electron density between 60 and 75 km altitude. However, beam attenuation below 75 km during daylight will be minimized as electron attachment is accelerated by the elevated electron temperature in the HF beam. When the beam is on, the free electron density within the beam will be reduced below 75 km altitude. Three-body attachment is not important above 85 km.

The denser ionosphere within the auroral oval reflects the 2.8 MHz beam so the flux drops to zero (Figure 31c). Greater energy deposition rates occur in the ionosphere of the auroral region. The beam attenuation is obvious in all examples except the 8MHz beam in the less dense ionosphere (Figure 31c,d).

Electron temperatures of the D and E regions calculated from the balance of cooling and heating terms are larger than the temperature enhancements calculated in the *Perkins and Roble* [1979] model of Arecibo HF heating experiments. The same total emission energy was used (3MW) but the beam width is narrower than the previous study providing for larger energy fluxes.

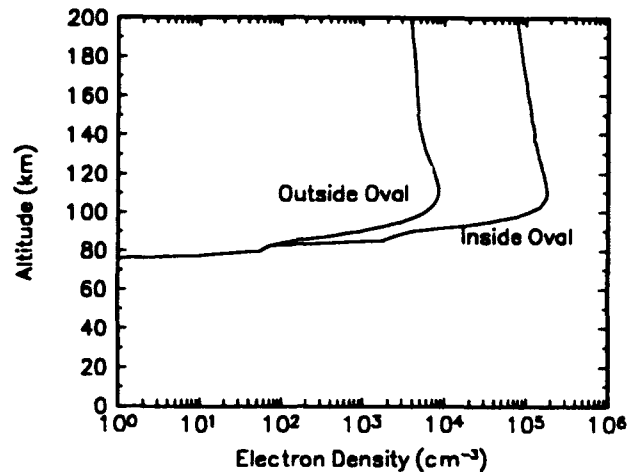


Figure 30. Electron density profiles in and out of the auroral oval. The conditions are for nighttime winter with moderate auroral activity.

A very high electron temperature results in ionization and dissociation of the neutral atmosphere through electron impact. The temperatures of .8eV at 90 km within HF beam are still not high enough for ionization or dissociation to become important. Even though the local energy deposition of the HF beam is comparable to an intense aurora, the heated electrons do ionize efficiently (Figure 32g,h). Most of the energy goes into vibrational and rotational excitation of O₂ and N₂. The ratio of the rates of ionization to energy deposition determined from the energy deposition model predicts one ion-electron pair produced per 10¹⁰ eV energy deposited. The energy deposition from high-energy particle events (>500 eV), such as in auroras, SPEs, GCEs, RPEs, produces ion-electron pairs efficiently. For such events one ion-electron pair is created per 35 eV deposited.

The impact of HF heating on the odd nitrogen chemistry can be estimated from the ion-electron pairs produced within the beam. Using the number of 1.3 odd nitrogen molecules per ion-electron pair, the total beam emission rate and 10¹⁰ eV per ion-electron pair, 2x10¹⁵ molecules/s are produced in the beam. We can now compare these rates to the natural production mechanisms of odd nitrogen listed in Tables 9 and 10. For the typical operation of an HF radar (Table 11) an annual operation time of 10⁶ s is expected. Therefore, 2x10²¹ odd nitrogen molecules could be produced during a year of HF operation. This is 14 orders of magnitude less than natural processes.

The possibility anomalous heating within the HF beam was mention previously. Anomalous heating can produce electrons with 2 to 10 eV energy within the F region of the ionosphere. This F region heating is only a limited percentage of the beam energy. Much of the beam energy will be deposited in the D and E region where ohmic heating dominates. The higher energy electrons of anomalous heating are still less efficient in ionizing air than particle precipitation events. The ratio of one ion-electron pair per 35 eV is used for particle energies above 500 eV [Banks and Kocharts, 1973].

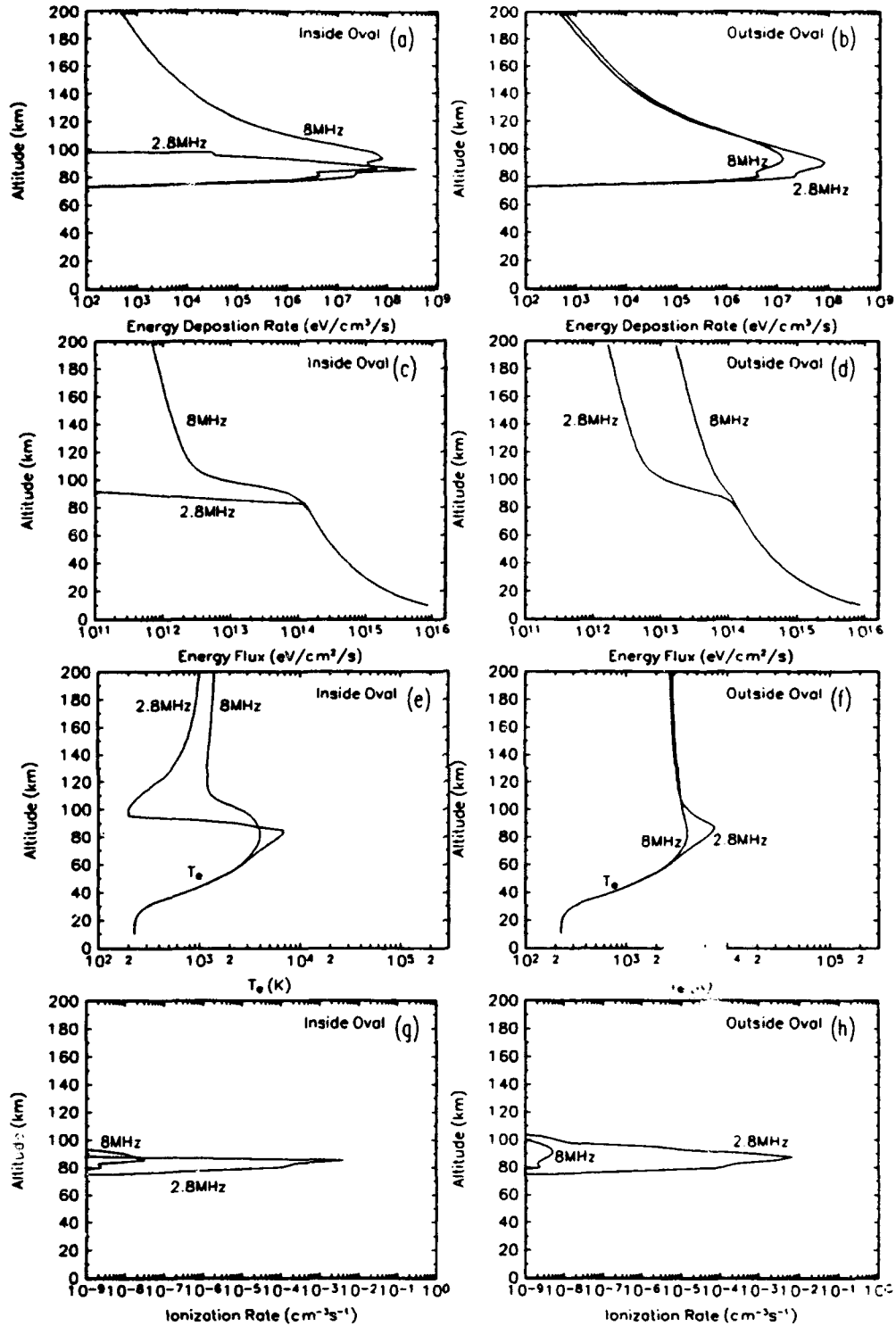


Figure 31. Results of deposition model are for beam frequencies of 2.8 and 8 MHz. Local energy deposition for (a) inside the auroral region and (b) outside the auroral region. Energy flux of HF beams for (c) inside the auroral region and (d) outside the auroral region. Electron temperatures for (e) inside auroral region and (f) outside auroral region. Ionization profiles for (g) inside the aurora zone and (h) outside the aurora zone.

15. DETAILED CHEMISTRY OF A PARCEL OF AIR IN AN HF BEAM

The time-dependent detailed chemistry of a parcel of air within the HF beam can be studied using information obtained from the energy deposition model described in the previous sections. The detailed chemistry model is used to examine the efficiency of odd nitrogen molecule creation within an HF heater beam. The energy deposited within the HF beam will not produce ion-electron pairs. However, other reactions could be driven by the elevated electron temperatures. Are there other avenues of odd nitrogen production within the beam? This is the question to be answered in this section.

The calculated results of the energy deposition model of the HF beam are used to drive the chemistry of a Lagrangian parcel of air moving through the beam. At 90 km the HF beam, where the deposition peaks, is 5 km in diameter. The wind velocities vary between 0 and 60 m/s with 35 m/s average at 90 km altitude. The electron temperature and energy deposition histories for the Lagrangian parcel are shown in Figure 32. The initial densities for the detailed chemistry study are obtained from MSIS90 [Hedin, 1991] and a model minor species mixing ratios [Anderson *et al.*, 1986]. Ionospheric constituents and ionization source terms are from the Rasmussen *et al.* [1989]. A fully time-dependent chemistry model and an extensive reaction database is used to solve a system of ordinary differential equations for 152 atmospheric species and 1844 reactions. The chemistry is defined by a comprehensive set of reactions [Kennealy *et al.*, 1989; Larkin, personal communication] for the regions of the HF radar energy deposition. The conditions in the air parcel are allowed to arrive at steady state before the energy deposition is increased. Two cases are examined. The first case represents a high-energy particle precipitation event that varies in time and the second case represents energy deposition in a moving parcel of air within an HF heater beam. The energy deposition profile is the same for both cases (Figure 32a). Only the ionization efficiencies are different.

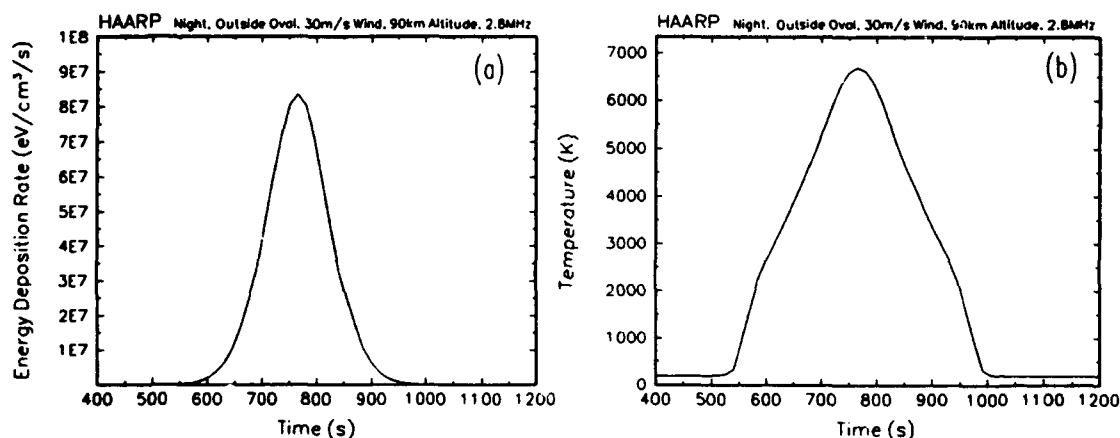


Figure 32. (a) Energy deposition rates and (b) electron temperature seen by a parcel of air moving through the HF heater beam at 30 m/s. These values are used to drive a detailed chemistry model, first, within an HF heater beam and, second, during a high-energy particle precipitation event.

For the first case of the high-energy particle precipitation, the energy deposition curve of 11.1a is used to drive ionization reactions whose rates are defined by the "magic number", 35 eV per one ion-electron pair. The resulting chemical changes during the high-energy particle precipitation event are plotted in Figure 33 with dotted lines. The increase in plasma density is large during the precipitation event but the plasma relaxes to previous densities with some differences in the pre- and post-event composition (that is, less O_2^+ after the event). The odd nitrogen species, NO, N, and NO_2 , all increase dramatically. Only N decreases after the event. NO and NO_2 remain at the elevated densities due to the absence of destruction processes during polar winter.

The second case examined was a parcel of air moving through the HF beam at 30 m/s. The electron temperature curve in Figure 32a was used to drive the chemistry. The electron temperature history (Figure 32b) was derived from the energy deposition curve show in Figure 32a. The neutral and ion temperature histories were also included in the model. Both temperatures only increase about 1° K during the parcel transit of the beam.

Within the HF beam, the elevated electron temperature slows the dissociative recombination rates. This increases the plasma density (Figure 33a). The increase in plasma density is not due to increased ionization levels. After leaving the beam, the plasma within the parcel returns to ambient density and composition. The odd nitrogen levels are unchanged throughout the transit of the beam (Figure 33b). There are some composition changes when the parcel is in the beam, such as increased metastable species, but these return to ambient levels upon beam exit or turn off. There is no observable odd nitrogen production. An NO production between the two cases of energy deposition is more likely due to non-thermal characteristics of electrons in electric fields [Carron, 1992].

The small region within the HF heater beam has local energy deposition rates that are comparable to intense auroras. This permits well determined modification experiments to be performed on the ionosphere. In particular, energy deposition and excited species chemistry might be examined through carefully planned optical experiments. The studies may elucidate the chemical time constants within the E and F regions.

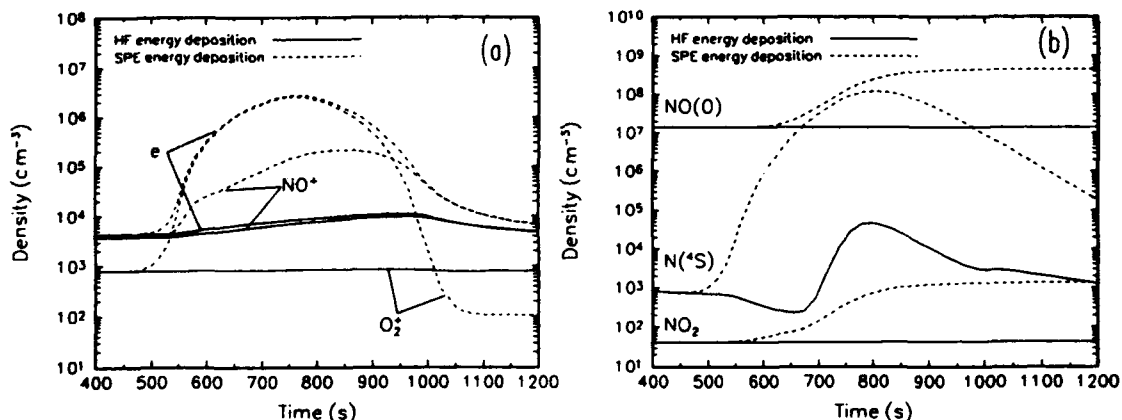


Figure 33. The chemical changes are shown for two different cases. The energy deposition is the same in both cases but one case represents HF heating effects (solid lines) and the other represents high-energy particle precipitation effects (dotted lines). (a) The main plasma constituents and (b) the odd nitrogen molecules within the air parcel are shown for the two cases.

16. DISCUSSION OF HF HEATING

We have compared atmospheric energy deposition of nature to that of an HF radar to determine the magnitude of long term chemical effects of HF operations in the atmosphere. The total energy emitted by an HF radar is many orders of magnitude smaller than the mesospheric and thermospheric energy deposition by natural processes. Natural energy deposition, which leads to ionization and odd nitrogen production, is also orders of magnitude larger than the yearly energy emission of an HF facility. By assuming the most efficient production of odd nitrogen per energy deposited we show that the HF radar has essentially no effect on the global chemical balance. However, the HF radar can be a perturber of local quantities for regions of 10's of kilometers. The perturbing ability may be an important tool for investigating D and E region chemistry. An important next step from this study is to include non-maxwellian electron distributions [Carron, 1992] to estimate the NO_x production efficiency within HF beams over a range of conditions and modes of operation.

REFERENCES

- Abreu, V. J., J. H. Yee, S. C. Solomon, and A. Dalgarno, The quenching rate of $O(^1D)$ by $O(^3P)$, *Planet. Space Sci.*, **34**, 1143, 1986.
- Albritton, D. L., I. Dotan, W. Lindinger, M. McFarland, J. Tellinghuisen, and F. C. Fehsenfeld, Effects of ion speed distributions in flow-drift tube studies of ion-neutral reactions, *J. Chem. Phys.*, **66**, 410, 1977.
- Anderson, G.P., J.H. Chetwynd, S.A. Clough, E.P. Shettle, and F.X. Kneizys, *AFGL Atmospheric Constituent Profiles (0-120km)*, ADA175173, Air Force Geophysics Laboratory, 1986.
- Anderson, D. and M. Mendillo, Ionospheric conditions affecting the evolution of equatorial plasma depletions, *Geophys. Res. Lett.*, **10**, 541, 1983.
- Archer, D.H., DNA chemistry panel review—CO₂, *DNA-TR-90-92*, Defense Nuclear Agency, 1990.
- Babcock, L.M., and G.E. Streit, Negative ion-molecule reactions of SF₄, *J. Chem. Phys.*, **75**, 3864, 1981.
- Banks, P.M. and G. Kockarts, *Aeronomy, Part A and B*, Academic Press, New York, 1973.
- Barr, R., and P. Stubbe, On the ELF generation efficiency of the Tromsø heater facility, *Geophys. Res. Lett.*, **18**, 1971, 1991.
- Bates, D.R., Theoretical considerations regarding some inelastic atomic collision processes of interest in aeronomy: Deactivation and charge transfer, *Planet. Space Sci.*, **37**, 363, 1989.
- Bernhardt, P.A., and L.M. Duncan, The theory of ionospheric focused heating, *J. Atmos. Terr. Phys.*, **49**, 1107, 1987.
- Bernhardt, P.A., Chemistry and dynamics of SF₆ injections into the F Region, *J. Geophys. Res.*, **89**, 3929, 1984.
- Bernhardt, P.A., C.A. Tepley, and L.M. Duncan, Airglow enhancements associated with plasma cavities formed during ionospheric heating experiments, *J. Geophys. Res.*, **94**, 9071, 1989.
- Bernhardt, P.A., E.J. Weber, J.G. Moore, J. Baumgardner and M. Mendillo, Excitation of oxygen permitted line emissions by SF₆ injection into the F region, *J. Geophys. Res.*, **91**, 8937, 1986.
- Bernhardt, P.A., A critical comparison of ionospheric depletion chemicals, *J. Geophys. Res.*, **92**, 4617, 1987.
- Biondi, M.A., Charged-particle recombination processes, *DNA Reaction Rate Handbook*, 1972.
- Bortner, M.H., R.H. Kummler, and T. Baurer, Summary of suggested rate constants, *DNA Reaction Rate Handbook*, 1972.
- Branscomb, L.M., Electron attachment of O, *Ann. Geophys.*, **20**, 88, 1964.
- Burch, D.S., S.J. Smith, and L.M. Branscomb, Photo-detachment of O₂, *Phys. Rev.* **112**, 171, 1958.
- Burch, D.S., S.J. Smith, and L.M. Branscomb, Errata, *Phys. Rev.* **114**, 1652, 1959.
- Cakir, S., G. Haerendel and J.V. Eccles, Modeling the ionospheric response to artificially produced density enhancements, *J. Geophys. Res.*, **97**, 1193, 1992.
- Caledonia, G.E., J.C. Person and D.E. Hastings, The interpretation of space shuttle measurements of ionic species, *J. Geophys. Res.*, **92**, 273, 1987.
- Callis, L.B., D.N. Baker, J.B. Blake, J.D. Lambeth, R.E. Boughner, M. Natarajan, R.W. Klebesadel, and D.J. Gorney, Precipitating relativistic electrons: Their long-term effect on stratospheric odd nitrogen levels, *J. Geophys. Res.*, **96**, 2939, 1991.
- Carlson, H.C. Jr., and L.M. Duncan, HF excited instabilities in space plasmas, *Radio Sci.*, **12**, 1001, 1977.
- Carron, N.J., Energy-diffusion calculation of the electron-swarm distribution function, *Phys. Rev. A*, **45**, 2499, 1992.
- Church, M.J., and D. Smith, Binary ionic recombination of SF₅⁻ and SF₆⁻ at 300K, *Int. J. Mass Spectrom. Ion Phys.*, **23**, 137, 1977.
- Crutzen, P.J., The influence of nitrogen oxides on the atmospheric ozone content, *Q. J. R. Meteorol. Soc.*, **96**, 320, 1970.
- DuBois, D.F., H.A. Rose and D. Russell, Excitation of strong Langmuir turbulence in plasmas near critical density: Application to HF heating of the ionosphere, *J. Geophys. Res.*, **95**, 21221, 1990.
- Dunkin, D.B., F.C. Fehsenfeld, A.L. Schmeltekopf and E.E. Ferguson, Ion-molecule reaction studies from 300 to 600K in a temperature-controlled flowing afterglow system, *J. Chem. Phys.*, **49**, 1365, 1968.

- Farley, D.T., Artificial heating of the electrons in the F region of the ionosphere, *J. Geophys. Res.*, **68**, 401, 1963.
- Farley, D.T., C. LaHoz, and B.G. Fejer, Studies of the self-focusing instability at Arecibo, *J. Geophys. Res.*, **88**, 2083, 1983.
- Fejer, B.G., The equatorial ionospheric electric fields: A review, *J. Atmos. Terr. Phys.*, **43**, 377, 1981.
- Fehsenfeld, F.C., E.E. Ferguson, and A.L. Schmeltekopf, Thermal-energy associative-detachment reactions of negative ions, *J. Chem. Phys.*, **45**, 1884, 1966.
- Fehsenfeld, F.C., E.E. Ferguson, and A.L. Schmeltekopf, Thermal-energy ion-neutral reaction rates. III. The measured rate constant for the reaction $O^+ + CO_2 \rightarrow O_2^+ + CO$, *J. Chem. Phys.*, **44**, 3022, 1966.
- Fehsenfeld, F.C., A.L. Schmeltekopf, H.I. Schiff, and E.E. Ferguson, Laboratory measurements of negative ion reactions of atmospheric interest, *Planet. Space Sci.*, **15**, 373, 1967.
- Fehsenfeld, F.C., D.L. Albritton, J.A. Burt, and J.I. Schiff, Associative-detachment reactions of O^- and O_2^- by $O^2(^1\Delta_2)$, *Can. J. Chem.*, **47**, 1793, 1969.
- Fehsenfeld, F.C., D.B. Dunkin, and E.E. Ferguson, Rate constants for the reaction of CO_2^+ with O, O_2 , and NO; N_2^+ and O and NO; and O_2^+ with NO, *Planet. Space Sci.*, **18**, 1267, 1970.
- Fehsenfeld, F.C., Electron attachment to SF_6 , *J. Chem. Phys.*, **53**, 2000, 1970.
- Fehsenfeld, F.C., Ion Chemistry of SF_6 , *J. Chem. Phys.*, **54**, 438, 1971.
- Fehsenfeld, F.C., C.J. Howard, and E.E. Ferguson, Thermal energy reactions of negative ions with H atoms in the gas phase, *J. Chem. Phys.*, **58**, 5841, 1973.
- Frederick, J.E., and N. Orsini, The distribution and variability of mesospheric odd nitrogen: a theoretical investigation, *J. Atmos. Terr. Phys.*, **44**, 479, 1982.
- Greenberg, K.E., and P.J. Hargis, Jr., Detection of sulfur dimers in SF_6 and SF_6/O_2 plasma-etching discharges, *Appl. Phys. Lett.*, **54**, 1374, 1989.
- Guberman, S.L., The production of $O(^1D)$ from dissociative recombination of O_2^+ , *Planet. Space Sci.*, **36**, 47, 1988.
- Haerendel, G., O.J. Bauer, S. Cakir, H. Goppl, E. Rieger, and A. Valenzuela, Coloured Bubbles-An experiment for triggering equatorial spread F, Active Experiments in Space, *Eur. Space Agency Spec. Publ.*, SP-195, 295, 1983.
- Haerendel, G., J.V. Eccles, and S. Cakir, Theory for modeling the equatorial evening ionosphere and the origin of the shear in the horizontal plasma flow, *J. Geophys. Res.*, **97**, 1209, 1992.
- Hedin, A.E., Extension of the MSIS thermospheric model into the middle and lower atmosphere, *J. Geophys. Res.*, **96**, 1159, 1991.
- Hunton, D.E., A.A. Viggiano, W. Swider, J.F. Paulson, and C. Sherman, Mass Spectrometric Measurements of SF_6 Chemical Releases, *J. Geophys. Res.*, **92**, 8827, 1987.
- Hunton, D.E., A.A. Viggiano, R.A. Morris, J.F. Paulson, D. Smith, and N.G. Adams, The $O^+ + CO_2$ reaction: New results and atmospheric implications, *J. Geophys. Res.*, **96**, 13881, 1991.
- Jackman, C.H., J.E. Frederick, and R.S. Stolarski, Production of odd nitrogen in the stratosphere and mesosphere: An intercomparison of source strengths, *J. Geophys. Res.*, **85**, 7495, 1980.
- Jaffe, S., and F.S. Klein, An ion cyclotron resonance mass spectrometric study of ion molecule reactions in CO_2 and CO, *Int. J. Mass Spectro. and Ion Phys.*, **14**, 459, 1974.
- Johnston, H.S. Reduction of stratospheric ozone by nitrogen oxide catalysts from SST exhaust, *Science*, **173**, 517, 1971.
- Johnsen, R., H.L. Brown and M.A. Biondi, Ion-molecule reactions involving N_2^+ , N^+ , O_2^+ , and O^+ ions from 300K to 1 eV, *J. Chem. Phys.*, **52**, 5080, 1970.
- Kennealy, J.P., S.B. Downer, R.J. Larkin, and T.J. Moratz, ARCHON-22, DNA-TR-89-65-VI, Defense Nuclear Agency, 1989.
- Kline, L.E., Electron and chemical kinetics in the low-pressure RF discharge etching of silicon in SF_6 , *IEEE Trans. Plasma Sci.*, **14**, 145, 1986.
- Lindenger, W. R.C. Fehsenfeld, A.L. Schmeltekopf, and E.E. Ferguson, Temperature dependence of some ionospheric ion-neutral-reactions from 300-900K, *J. Geophys. Res.*, **59**, 4753, 1974.
- Link, R. and L.L. Cogger, A reexamination of the OI 6300Å nightglow, *J. Geophys. Res.*, **93**, 9883, 1988.
- Mantas, G.P., H.C. Carlson, C. H. LaHoz, Thermal response of the F region ionosphere in artificial modification experiments by HF radio waves, *J. Geophys. Res.*, **86**, 561, 1981.

- Megill, L.R., J.C. Haslett, H.I. Schiff, and G.W. Adams, Observations of $O_2(^1\Delta_g)$ in the atmosphere and allowable values of the eddy diffusion coefficient, *J. Geophys. Res.*, 75, 6398, 1970.
- Meltz, G. and R.E. LeLevier, Heating the F region by derivative absorption of radio waves, *J. Geophys. Res.*, 75, 6406, 1970.
- Meltz, G., L.H. Holway, Jr., N.M. Tomljanovich, Ionospheric heating by powerful radio waves, *Radio Sci.*, 11, 1049, 1974.
- Mendillo, M. and J. Baumgardner, Optical signature of an ionospheric hole, *Geophys. Res. Lett.*, 215-218, 1982.
- Mendillo, M. and J. Forbes, Theory and observation of a dynamically evolving negative ion plasma, *J. Geophys. Res.*, 87, 8273, 1982.
- Miller, T.M., A.E.S. Miller, J.F. Paulson, and X. Liu, Thermal electron attachment to SF_4 and SF_6 , *J. Chem. Phys.*, 100, 8841, 1994.
- Mothes, K.G., E. Schultes, and R.N. Schindler, Application of electron cyclotron resonance technique in studies of electron capture processes in the thermal energy range, *J. Phys. Chem.*, 76, 3758, 1972.
- Mosesman, M. and W.T. Huntress, On the reaction of O^+ with CO_2 , *J. Chem. Phys.*, 53, 462, 1970.
- Mullen, J.H., J.M. Madson, and L.N. Medgyesi-Mitschang, Measurement of electron attachment processes in a high-temperature plasma, *Proceedings of the IEEE*, 59, 605, 1971.
- Narcisi, R. S., Quantitative determination of the outgassing water vapor concentrations surrounding space vehicles from ion mass spectrometer measurements, *Adv. Space Res.*, 2, 283, 1983.
- Olson, R.E., J.R. Peterson, and J. Moseley, Oxygen ion-ion neutralization reaction as related to tropical ultraviolet nightglow, *J. Geophys. Res.*, 76, 2516, 1971.
- Olthoff, J.K., R.J. Van Brunt, Y. Wang, R.L. Champion, and L.D. Doverspike, Collisional electron detachment and decomposition rates of SF_6^- , SF_5^- , F^- in SF_6 : Implications for ion transport and electrical discharges, *J. Chem. Phys.*, 91, 2261, 1989.
- Orsini, N. and T. Shimazaki, Diurnal variations of odd nitrogen and ionic densities in the mesosphere and lower thermosphere: Simultaneous solution of photochemical-diffusive equations, *J. Geophys. Res.*, 80, 3945, 1975.
- Orsini, N. and J.E. Frederick, Solar disturbances and mesospheric odd nitrogen, *J. Atmos. and Terr. Phys.*, 44, 489, 1982.
- Paulson, J.F. and R.L. Mosher, Reaction $O^+ + CO_2 \rightarrow O_2^+ + CO$, *Bull. Am. Phys. Soc.*, 7, 633, 1966.
- Perkins, F.W. and R.G. Roble, Ionospheric heating by radio waves: Predictions for Arecibo and the satellite power station, *J. Geophys. Res.*, 83, 1611, 1978.
- Phelps, A.V., and R.J. Van Brunt, Electron-transport, ionization, attachment, and dissociation coefficients in SF_6 and its mixtures, *J. Appl. Phys.*, 64, 4259, 1988.
- Queffelec, J.L., B.R. Rowe, F. Vallee, J.C. Gomet and M. Morlais, The yield of metastable atoms through dissociative recombination of O_2^+ ions with electrons, *J. Chem. Phys.*, 91, 5335, 1989.
- Rasmussen, C.E., R.W. Schunk, and V.B. Wickwar, A photochemical equilibrium model for ionospheric conductivity, *J. Geophys. Res.*, 93, 9831, 1988.
- Richmond, A.D., S. Matsushita and J.D. Tarpley, On the production mechanism of electric currents and fields in the ionosphere, *J. Geophys. Res.*, 81, 547, 1976.
- Rishbeth, H., Polarization fields produced by winds in the equatorial F region, *Planet. Space Sci.*, 19, 357, 1971.
- Roble, R.G., E.C. Ridley, and R.E. Dickinson, On the global mean structure of the thermosphere, *J. Geophys. Res.*, 92, 8745, 1987.
- Rosenberg, N.W. (Ed.), Project Firefly 1962-1963, *Environ. Res. Pap.* 1, CRL-64-363, Air Force Cambridge Res. Lab., Hanscom Field, Mass., 1964.
- Rusch, D.W., and C.A. Barth, Satellite measurements of nitric oxide in the polar region, *J. Geophys. Res.*, 80, 3719, 1975.
- Rusch, D.W., J.-C. Gerard, S. Solomon, P.J. Crutzen and G.C. Reid, The effect of particle precipitation events on the neutral and ion chemistry of the middle atmosphere I. Odd nitrogen, *Planet. Space Sci.*, 29, 767, 1981.

- Sauerb I., L.G. Christophorou, and S.M. Spyrou, Negative ion sormation in SF₆ spark by-products, *Plasma Chem. Plasma Proc.*, 13, 17, 1993.
- Schunk, R.W., and A.F. Nagy, Electron temperature in the F region of the ionosphere: Theory and observations, *Rev. Geophys. and Space Phys.*, 16, 355, 1978.
- Seppelt, Z. *anorg. ally. chem.*, 1977.
- Sipler, D.P., E. Enemark, and M.A. Biondi, 6300-Å intensity variations produced by the Arecibo ionospheric modification experiment, *J. Geophys. Res.*, 79, 4276, 1974.
- Showen, R. L., and R. A. Behnke, The effect of HF -induced plasma instabilities on ionospheric electron temperatures, *J. Geophys. Res.*, 83, 207, 1978.
- Solomon, S., P.J. Crutzen, and R.G. Roble, Photochemical coupling between the thermosphere and the lower atmosphere 1. Odd nitrogen from 50 to 120 km, *J. Geophys. Res.*, 87, 7206, 1982.
- Solomon, S.C., P.B. Hays, and V.J. Abreu, The auroral 6300Å emission: Observations and modeling, *J. Geophys. Res.*, 93, 9867, 1988.
- Solomon, S.C. and V.J. Abreu, The 630 nm dayglow, *J. Geophys. Res.*, 94, 6817, 1989.
- Spence, D. and G.J. Schulz, Temperature dependence of electron attachment at low energies for polyatomic molecules, *J. Chem. Phys.*, 58, 1800, 1973.
- Stockner, A.J., F. Honary, T.R. Robinson, T.B. Jones, P. Stubbe, and H. Kopka, EISCAT observations of large scale electron temperature and electron density perturbations caused by high power HF radio waves, *J. Atmos. Terr. Phys.*, 54, 1555, 1992.
- Thomson, J.A., Energy deposition in artificial ionospheric heating experiments, *J. Geophys. Res.*, 75, 6446, 1970.
- Torr, M.R. and D.G. Torr, The role of metastable species in the thermosphere, *Rev. Geophys. and Space Phys.*, 20, 91, 1982.
- Van Brunt, R.J., Production rates for oxyfluorides SOF₂, SO₂F₂ and SOF₄ in SF₆ corona discharges, *J. Res. National Bureau of Standards*, 90, 229, 1985.
- Van Brunt, R.J., L.W. Sieck, I. Sauers, and M.C. Siddagangappa, Transfer of F⁻ in the reaction of SF₆⁻ with SOF₄: Implications for SOF₄ production in corona discharges, *Plasma Chemistry and Plasma Processing*, 8, 225, 1988.
- Van Brunt, R.J. and J.T. Herron, Fundamental processes of SF₆ decomposition and oxidation in glow and corona discharges, *IEEE Transactions on Electrical Insulation*, 25, 75, 1990.
- Viggiano, A.A., R.A. Morris, F. Dale, and J.F. Paulson, Production of vibrationally excited O₂⁺ in the reaction O⁺ with CO₂, *J. Chem. Phys.*, 93, 1681, 1990a.
- Viggiano, A.A., R.A. Morris, and J.F. Paulson, Rate constant and branching fraction for the reaction of O⁺(²D, ²P) with CO₂, *J. Chem. Phys.*, 93, 1483, 1990b.
- Yee, J.H., and A. Dalgarno, The quenching of O(¹D) by O(³P) atoms, *EOS Trans. AGU*, 66, 993, 1985.
- Wang, Y., R.L. Champion, L.D. Doverspike, J.K. Olthoff, and R.J. Van Brunt, Collisional electron detachment and decomposition cross sections for SF₆⁻, SF₅⁻, F⁻ on SF₆ and rare gas targets, *J. Chem. Phys.*, 91, 2254, 1989.